DZero Note 4897
Version 3.6

Measurement of $Z \rightarrow e^+e^-$ and $W \rightarrow e^{\pm}\nu$ Production Cross Sections Using One Tight Central Electron

Doug Chapin, Harald Fox, John Gardner, Robert Illingworth, Adam Lyon, Junjie Zhu

Abstract

This note presents measurements of the Z and W boson production cross sections times branching fractions into electrons using the D0 detector and an integrated luminosity of 177 pb^{-1} of $p\bar{p}$ collisions from RunII of the Tevatron. Additionally, indirect results for the W leptonic branching ratio and W total width are extracted from the ratio of these cross sections.

Z and W candidates with at least one tight(track match and good electron likelihood) central($|\eta_{\text{det}}| < 1.05$) electron with $E_T > 25$ GeV are analyzed. After correction to the full p_T and η range, the measured cross sections are:

$\sigma_Z \times B(Z \rightarrow e^+e^-) =$
$267.7 \pm 3.0\ (stat) \pm 1.6\ (sys\_stat) \pm 4.5\ (sys)\ {}^{+4.0}_{-3.3}\ (pdf) \pm 17.4\ (lumi)\ pb$

and $\sigma_W \times B(W \rightarrow e^{\pm}\nu\ ) =$
$2929 \pm 9\ (stat) \pm 30\ (sys\_stat) \pm 49\ (sys)\ {}^{+56}_{-28}\ (pdf) \pm 190\ (lumi)\ pb.$

The ratio, R, of the W cross section times branching fraction to the Z cross section times branching fraction is
$10.94 \pm 0.13\ (stat) \pm 0.07\ (sys\_stat) \pm 0.14\ (sys)\ {}^{+0.12}_{-0.08}\ (pdf).$

Based on R and external Standard Model based inputs, indirect results for the W leptonic branching ratio, $Br(W \rightarrow e\nu)$, and W total width, Γ_W, are extracted:

$B(W \rightarrow e\nu) =$
$(10.89 \pm 0.13\ (stat) \pm 0.07\ (sys\_stat) \pm 0.14\ (sys)\ {}^{+0.12}_{-0.08}\ (pdf)$
$\pm 0.16\ (ext)\ )\%$

and $\Gamma_W =$
$2.080 \pm 0.024\ (stat) \pm 0.014\ (sys\_stat) \pm 0.027\ (sys)\ {}^{+0.023}_{-0.015}\ (pdf)$
$\pm 0.031\ (ext)$ GeV.

Contents

1 Introduction

The measurements of production cross sections for Z and W bosons test theoretical predictions of these cross sections. Z and W decays are also used for understanding and calibration of the detector. The W cross section will eventually be used to measure the delivered luminosity to a higher precision than is possible by measuring the inelastic $p\bar{p}$ cross section.

The events used in this analysis are from data collected between run 161973 (August 2002) and run 180956 (September 2003). The data has been processed with version p14 of the reconstruction program. Unnormalizable luminosity blocks and runs declared bad by the JET/MET group and detector subsystems (other than the muon system) are removed from this sample, leaving a total of 177 ± 12 pb^{-1} of luminosity. In order to reduce processing time, events with at least one electromagnetic object having $E_T > 15$ GeV were preselected from the RECO thumbnails and all studies were conducted on this sample. Approximately 62 million events meet the preselection criteria. D0CORRECT version v00-00-06 has been used to generate the root tuples used for the final analysis.

From the preselected data, three data sets are identified.

- Z Candidates - Events are required to have two electrons having $E_T > 25$ GeV and pseudorapidity satisfying $|\eta| < 1.05$ OR $1.5 < |\eta| < 2.3$. At least one of these electrons must be within $|\eta| < 1.05$ and pass tight cuts including a track match.

- W Candidates - Events are required to have one electron passing tight cuts including a track match, $E_T > 25$ GeV and pseudorapidity satisfying $|\eta| < 1.05$ along with missing transverse energy > 25 GeV.

- QCD-EM Sample - Events are required to have one EM object with identical selection criteria as used to select the W sample and one jet. The electron candidate and the jet are required to be back-to-back within $\Delta\phi < 0.5$. These events, assumed to be from QCD production of a γ/π^0 or other electromagnetic jet and a hadronic jet, are used for studying electron likelihood fake rates.

For our PMCS Monte Carlo simulation, efficiencies of the electron selection criteria are measured using the Z sample in bins of electron $\eta_{\mathrm{d}et}$, E_T and/or primary vertex z position. These measured efficiencies are used in PMCS to take correlations into account. The acceptance correction calculated from PMCS therefore includes corrections for selection efficiencies as well.

For this analysis, regions where $|\eta_{\mathrm{d}et}| > 1.05$ have been studied in parallel with $|\eta_{\mathrm{d}et}| < 1.05$ and work for all regions is shown in this note. However, too many problematic calorimeter regions in the end caps and limited statistics along with too many efficiency dependencies are issues which need to be resolved before quoting results requiring tight electrons with $|\eta_{\mathrm{d}et}| > 1.05$.

2 Calorimeter Issues

2.1 Central Calorimeter Cluster Phi Shifts

There are cracks in the central calorimeter between the azimuthal module boundaries. A particle entering the calorimeter near these boundaries can lose a portion of its energy to these cracks which will shift the phi cluster centroid toward the center of the module. These cracks are cut out by phi fiducial cuts and therefore particles falling within the bad phi fiducial region can have a measured calorimeter detector phi position shifted into the good phi fiducial region. It is important to model this effect accurately in PMCS since it will increase our acceptance.

Electrons with a track match are used to measure the calorimeter phi shift with the track position treated as the true position of the electron. The electron sample is taken from diem probes passing preselection cuts. See section 4.1 for details. Units of "phimod", defined as $(\phi_{det} \times 16/\pi) \, mod \, 1.0$, are used. In phimod units, 0.0 is at one calorimeter tower boundary and 1.0 is at the other. Phi fiducial cuts are made if phimod < 0.1 or phimod > 0.9. Figure 1 compares the track and calorimeter detector phimod positions of our electron sample. For the track, ϕ_{det} is always the phi position extrapolated to the calorimeter EM3 layer. It can be seen by comparing the track and calorimeter phimod distributions that many electrons are shifted out of the cracks. Figure 2 is a scatter plot of phimod shift as a function of track phimod measured by plotting calorimeter detector phimod - track detector phimod. The tendency for calorimeter phi to be shifted toward module centers is quite noticeable at the tower edges and also at the cell boundary at 0.5.

The amount electrons are shifted is found to be dependent not only on phimod position but also p_T and $|\eta_{physics}|$. To see this, the electron sample is divided into four bins for each quantity and plotted as a function of phimod as shown in figure 3. For PMCS, shifting is modeled as a function of phimod, p_T and $|\eta_{physics}|$. Bins are: 50 uniform bins from 0 to 1 for phimod, (< 36, 36 to 43, > 43 GeV) for p_T and (< 0.35, 0.35 to 0.65, > 0.65) for $|\eta_{physics}|$. This is described further in section 6.1.5.

2.2 Calibration by Module and Pseudorapidity

It has been found that the electron energy scale, described in section 6.1.2, is not consistent from module to module in phi in the central calorimeter. Also, missing E_T is significantly different between the positive and negative $\eta_{detector}$ halves. $u_{\|}$, described in section 6.1.9, has a direct effect on missing E_T and is found to vary with both phi module and pseudorapidity. For this reason, both relative electron energy scale and $u_{\|}$ are measured for each of the phi modules and both halves of the central calorimeter. Relative electron energy scale is measured as the peak in the ratio of calorimeter E_T to track p_T distribution for the W candidate sample, see figure 4. For $u_{\|}$, a cut is chosen which equally divides the W candidate sample based on measured $u_{\|}$, see figure 5. These distributions are used in PMCS to correct the electron energy scale and $u_{\parallel}$ shift parameters, which previously used single averaged values for the entire central region.

2.3 Problematic Calorimeter Regions

The calorimeter has a number of regions which have for all or part of the luminosity unreliable acceptance or efficiency. These regions must be cut out in the data and the reduced acceptance accounted for in the calculation. Problem areas are identified by both the relative number and EMid efficiency of EM objects falling within each of the calorimeter towers in η_{det} and ϕ_{det}. Affected cells are removed by cutting everything within a box centered on the cells and extending slightly beyond the cell boundaries in η_{det} and ϕ_{det} to account for effects on neighboring cells (see Figure 12). Since many problems occur for only a fraction of the data, run ranges are assigned to all of these boxes. An electron is cut if its η_{det} and ϕ_{det} fall within one of these boxes and its run number is within the corresponding box's run range. To model this in PMCS, luminosity weighted random run numbers are generated for each event. This, along with the generated η_{det} and ϕ_{det}, is applied in exactly the same way as data to determine if a generated electron should be cut. PMCS comparisons with and without these cuts indicate an acceptance loss of 8% for W candidate events and 20% for Z candidate events.

By comparing the number of EM objects passing EMid cuts in a calorimeter cell to the average number for all cells at that phi, low efficiency "holes" can be identified. Figures 6 to 11 show these low efficiency cells for each of the eleven run ranges studied. Low efficiency cells are identified by solid blue boxes, with the lightest blue boxes less 60% efficient down to the darkest blue with less than 20% efficiency. Also, cells with over twice the average acceptance are marked as bright orange solid boxes.

Hollow boxes represent regions cut out. The violet boxes are from "tower 2" [1], the green box is where signal cables were swapped, the dark blue are from "energy sharing" [2], black is from gain switching, light blue is central calorimeter phi module 17 and causes of red boxes have not been tracked down. Phi module 17 is removed because its energy scale is significantly lower than the rest, approximately 8%. A large fraction of the north(negative) end cap is removed because of the "checkerboard" pattern produced by gain switching. Lately, much work has been done in understanding and correcting for gain switching, but unfortunately not in time to be used for this analysis.

The 2D plots are useful as an overview, but to more precisely locate problem areas, 1D projections along η_{det} and ϕ_{det} are made both of all EM objects with p_T over 25 GeV and of EM objects satisfying EMid cuts. For example, Figure 12 shows EMid efficiency vs η_{det} and ϕ_{det} for regions with the "tower2" effect and figure 13 profiles the checkerboard pattern in the north end cap region of the calorimeter which alternate between high and low acceptance and EMid efficiency. Figure 14 shows acceptance and EMid efficiency for regions with "energy sharing" and figure 15 shows EMid efficiency vs η_{det} and ϕ_{det} for regions with cables swapped.

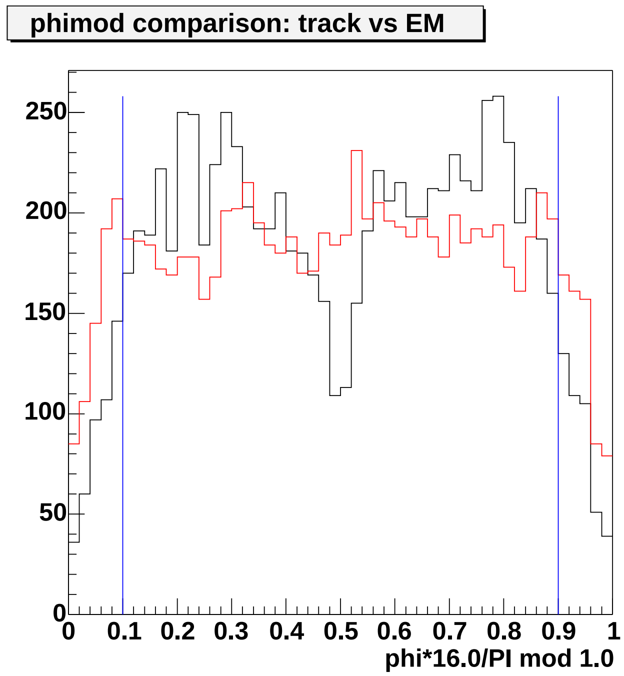

Figure 1: comparison of phimod positions for electrons passing preselection cuts. The red histogram is track phimod, black is calorimeter phimod and the blue lines are fiducial phi crack cut boundaries. Note that after the calorimeter phi shift there are much fewer electrons in the crack.

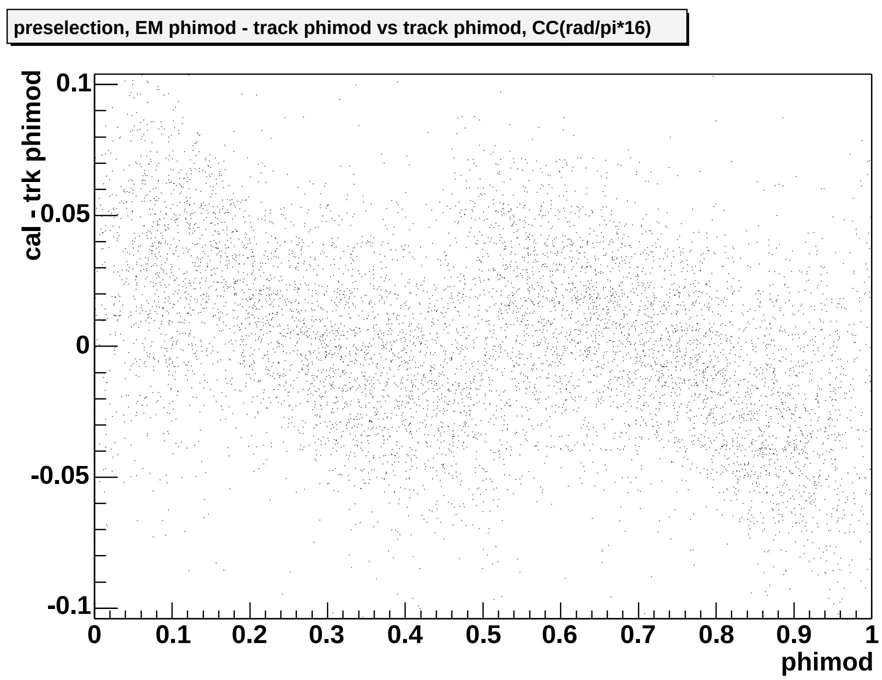

Figure 2: scatter plot showing shift of calorimeter phimod with respect to track phimod as a function of track phimod. Electrons are shifted away from the tower crack boundaries and also away from the EM cell boundary at 0.5.

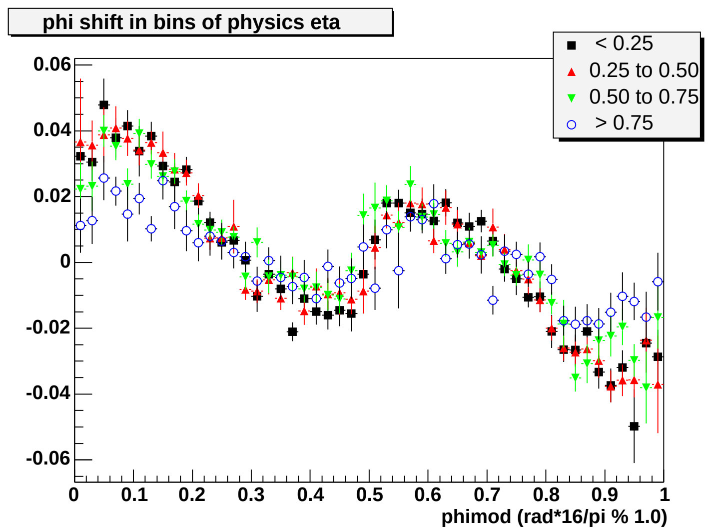

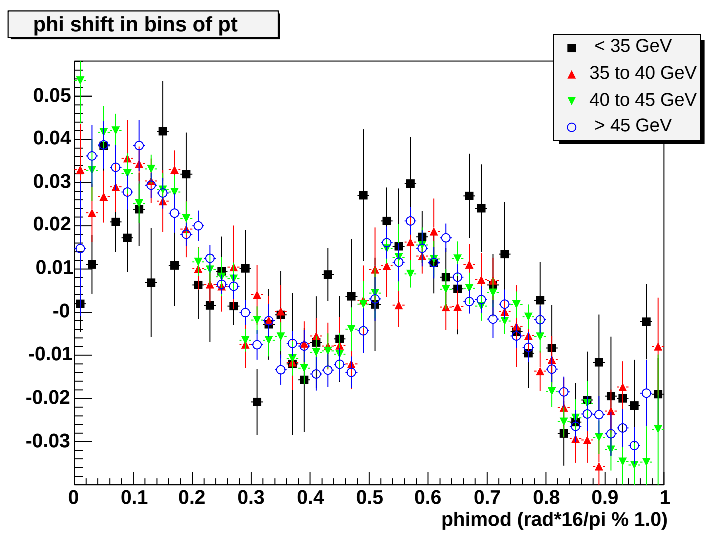

Figure 3: scatter plots vs. phimod showing dependence of calorimeter phimod shift on $\eta_{physics}$ (top) and p_T (bottom). The binning for each quantity is shown on the legends.

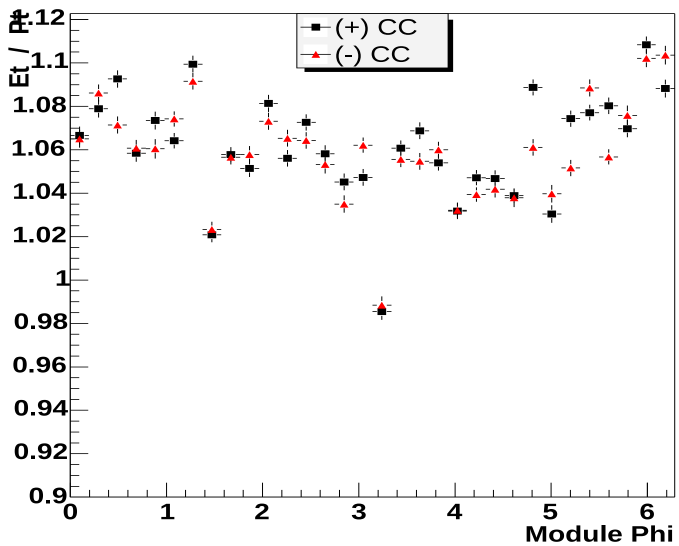

Figure 4: position of E_T/p_T peak for the W candidate sample as a function of phi module and detector half.

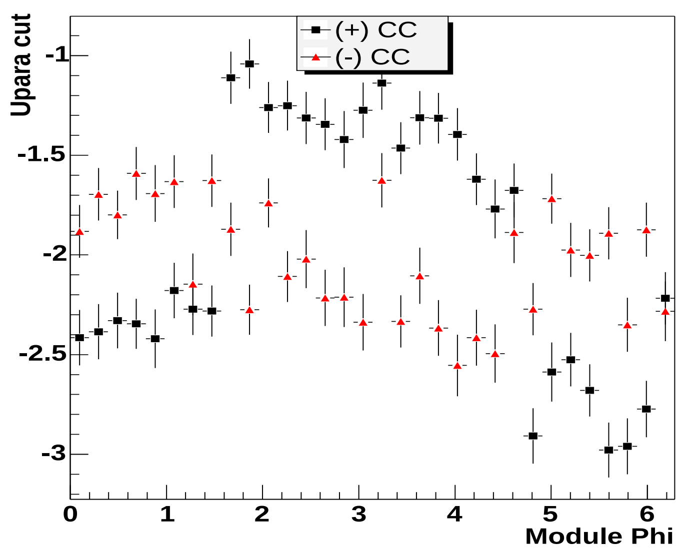

Figure 5: $u_{\parallel}$ cut equally dividing the W candidate sample as a function of phi module and detector half.

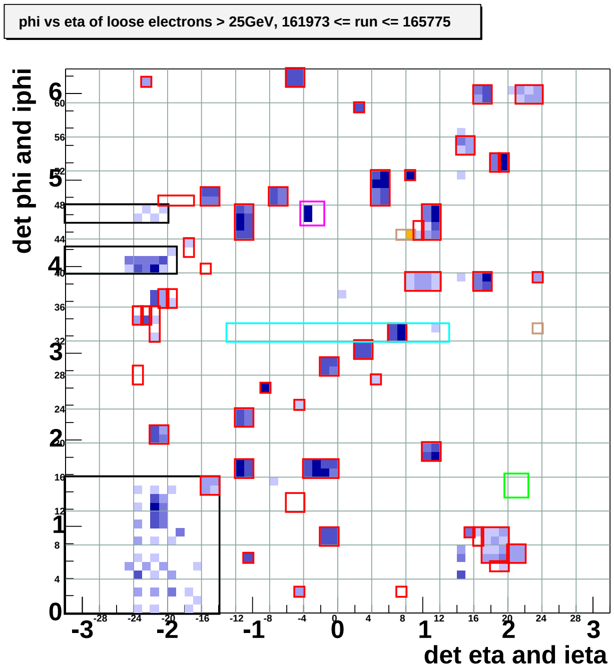

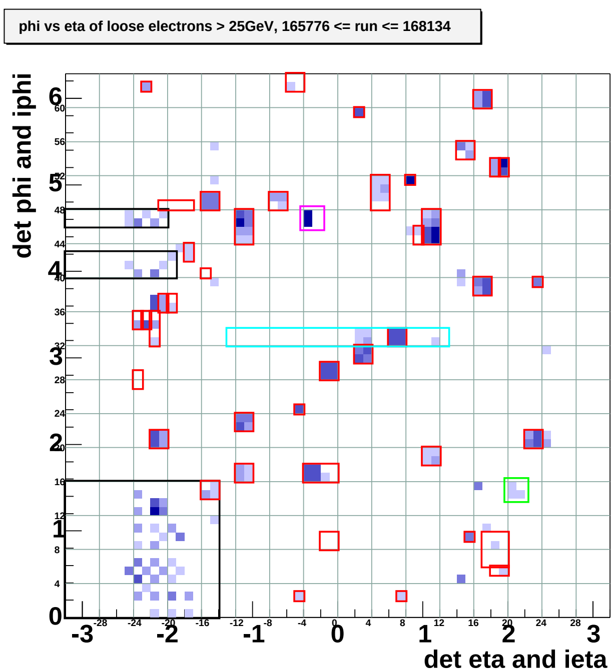

Figure 6: η_{det} vs ϕ_{det} calorimeter plots for (top) runs 161973 to 165775 and (bottom) 165776 to 168134. (hollow boxes are regions cut out, blue solid boxes are inefficient cells(lightest are $<$ 60% normal to darkest $<$ 20%), orange have at least twice normal acceptance)

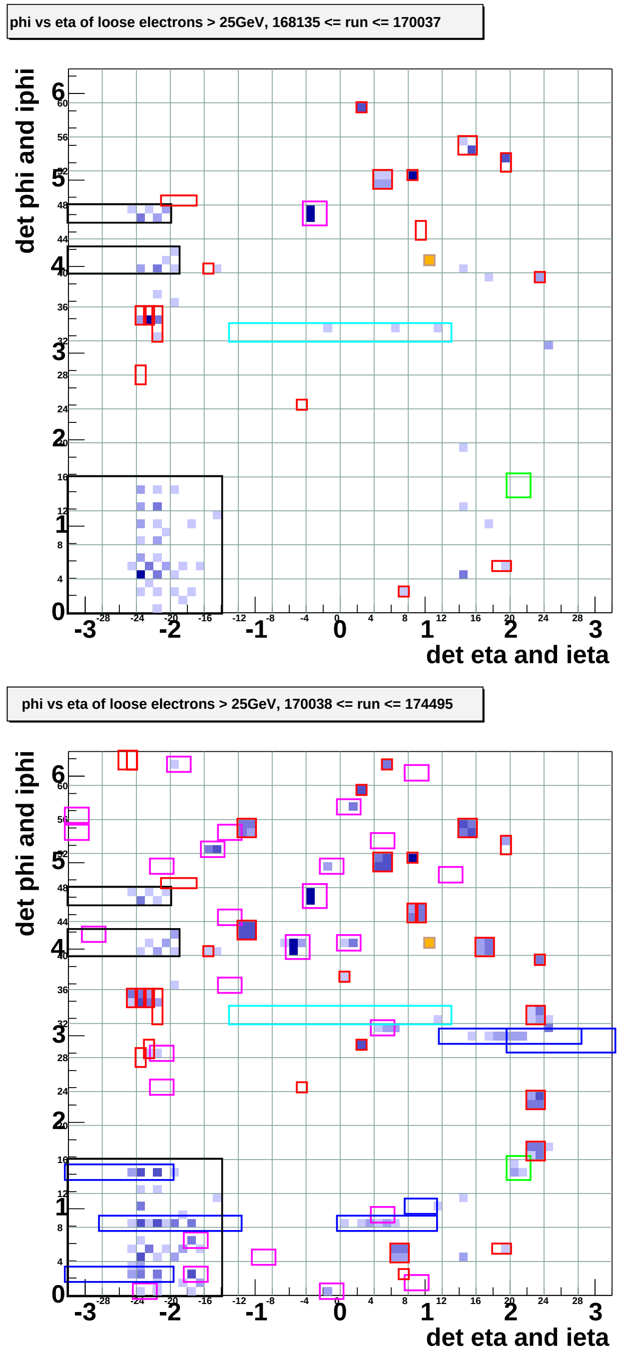

Figure 7: η_{det} vs ϕ_{det} calorimeter plots for (top) runs 168135 to 170037 and (bottom) 170038 to 174495. (hollow boxes are regions cut out, blue solid boxes are inefficient cells(lightest are $<$ 60% normal to darkest $<$ 20%), orange have at least twice normal acceptance)

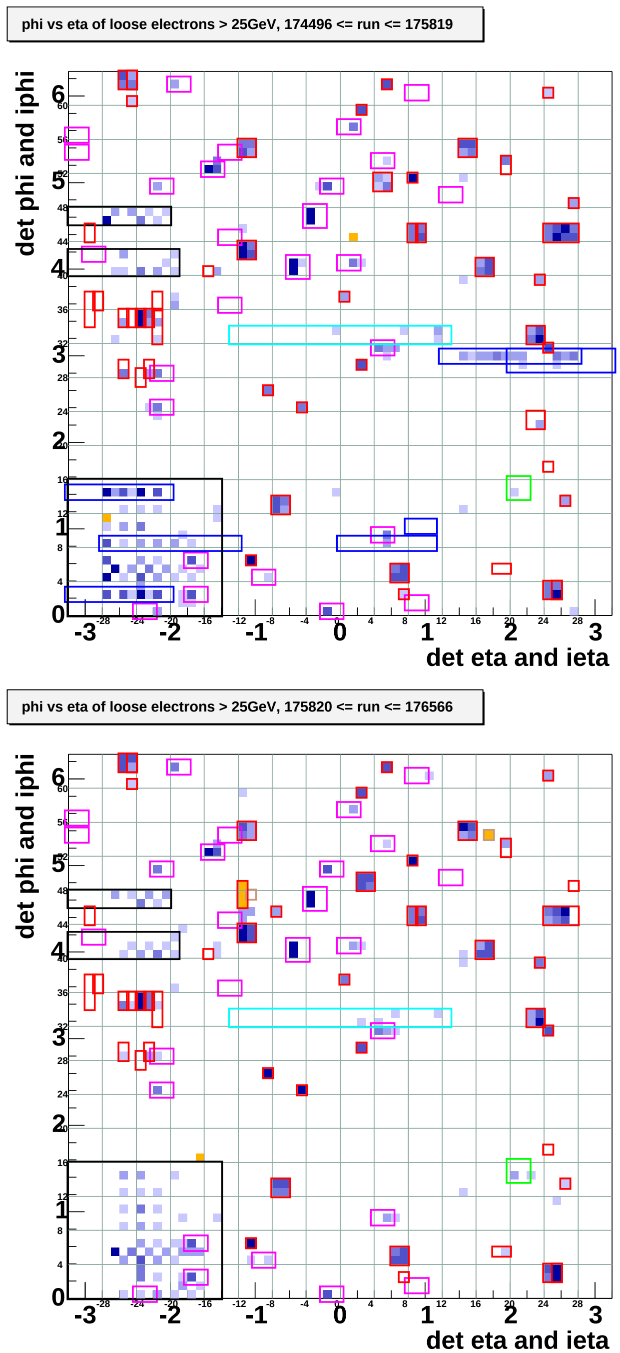

Figure 8: η_{det} vs ϕ_{det} calorimeter plots for (top) runs 174496 to 175819 and (bottom) 175820 to 176566. (hollow boxes are regions cut out, blue solid boxes are inefficient cells(lightest are < 60% normal to darkest < 20%), orange have at least twice normal acceptance)

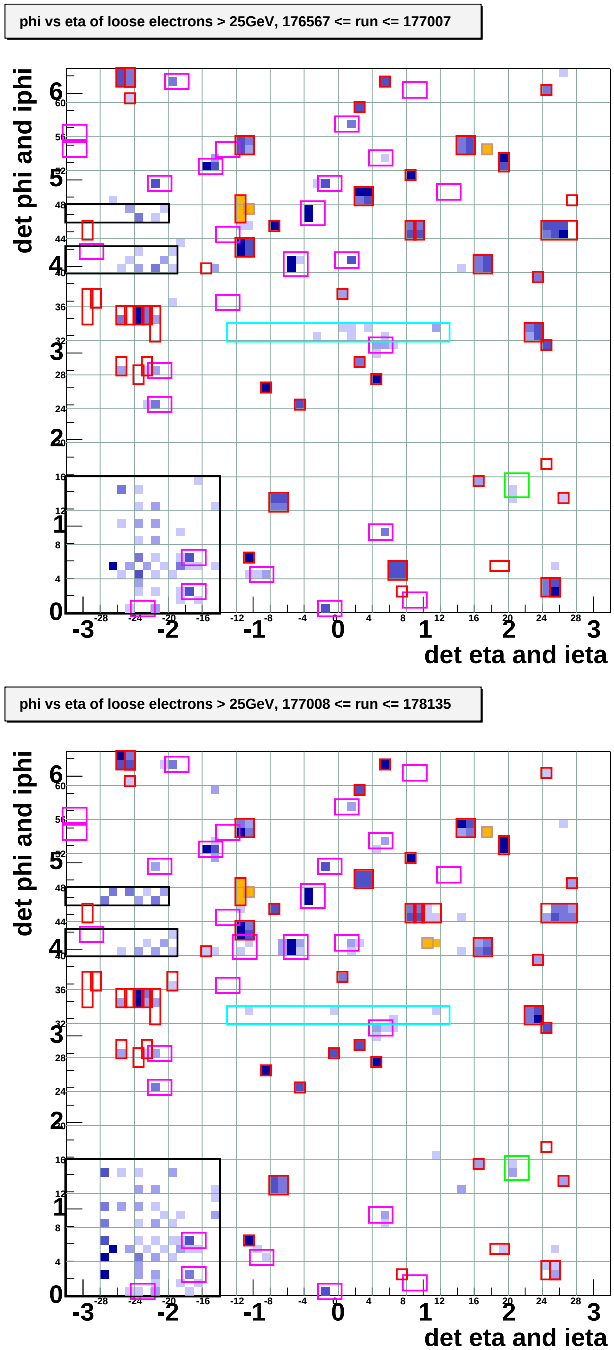

Figure 9: η_{det} vs ϕ_{det} calorimeter plots for (top) runs 176567 to 177007 and (bottom) 177008 to 178135. (hollow boxes are regions cut out, blue solid boxes are inefficient cells(lightest are < 60% normal to darkest < 20%), orange have at least twice normal acceptance)

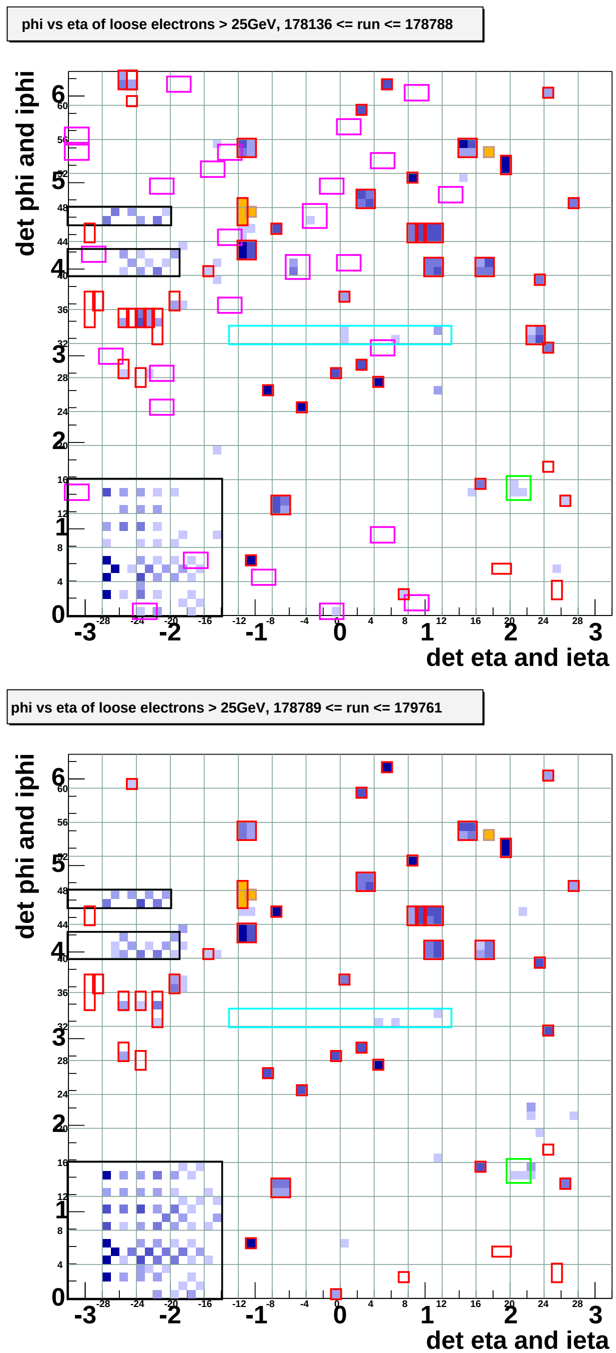

Figure 10: η_{det} vs ϕ_{det} calorimeter plots for (top) runs 178136 to 178788 and (bottom) 178789 to 179761. (hollow boxes are regions cut out, blue solid boxes are inefficient cells(lightest are $< 60\%$ normal to darkest $< 20\%$), orange have at least twice normal acceptance).

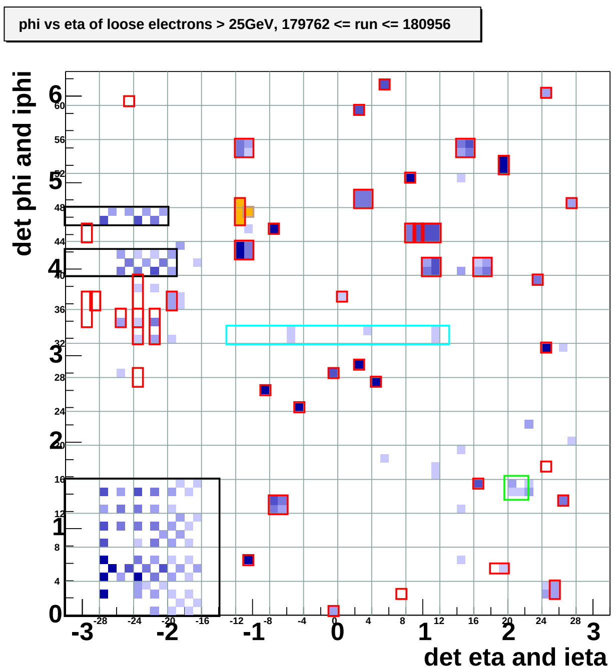

Figure 11: η_{det} vs ϕ_{det} calorimeter plot for runs 179762 to 180956. (hollow boxes are regions cut out, blue solid boxes are inefficient cells(lightest are $<$ 60% normal to darkest $<$ 20%), orange have at least twice normal acceptance)

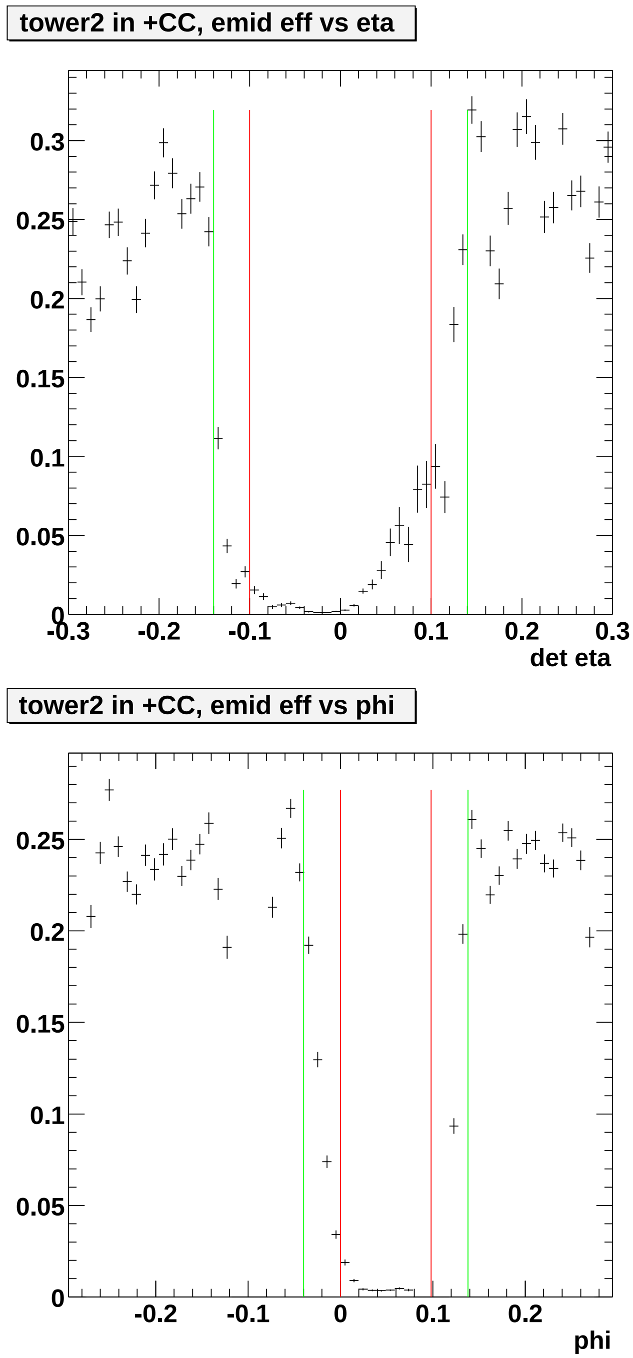

Figure 12: projections along (top)η_{det} and (bottom)ϕ_{det} of EMid efficiency vs position relative to the tower2 cells. The red lines indicate cell boundaries and the green lines indicate where data are cut.

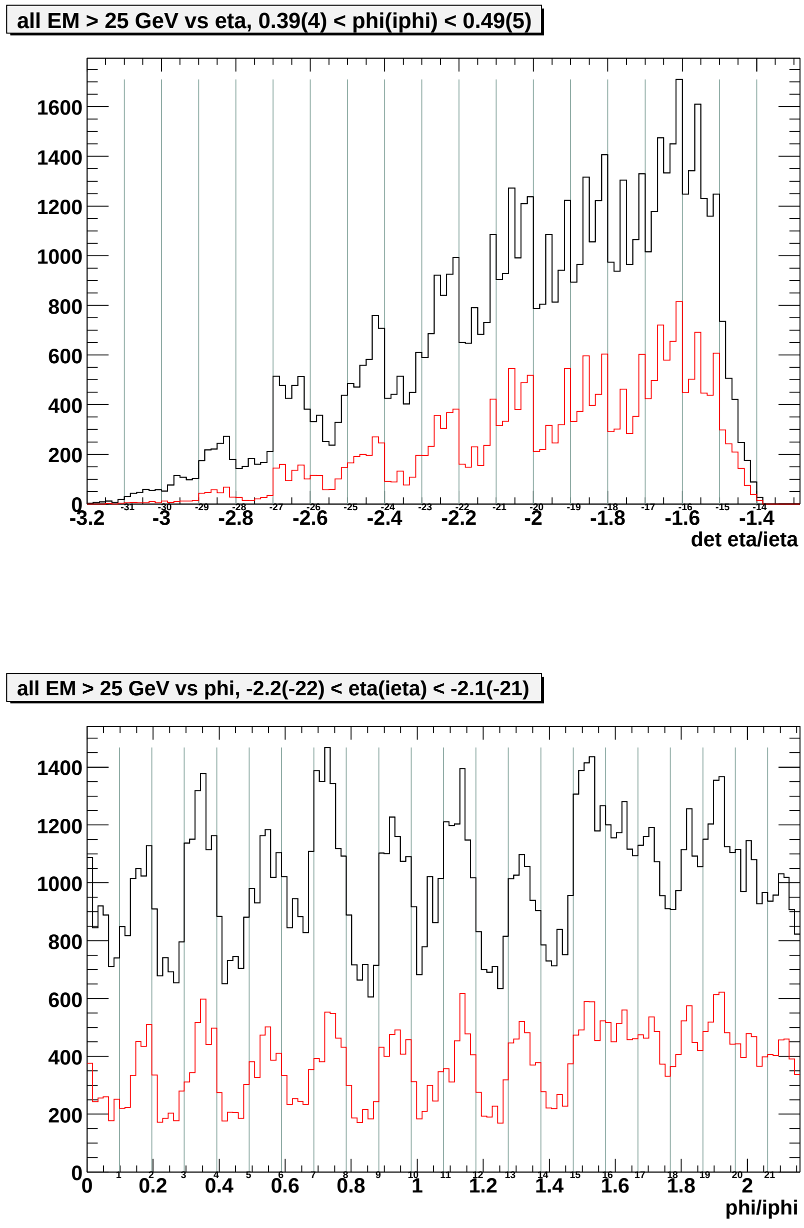

Figure 13: plots illustrating alternating calorimeter cells in the negative EC region. Projections are along (top) η_{det} where $0.39 < \phi_{det} < 0.49$ and (bottom) ϕ_{det} where $-2.2 < \eta_{det} < -2.1$. Plots are for (black) all EM objects with p_T greater 25 GeV and (red) EM objects passing EMid cuts.

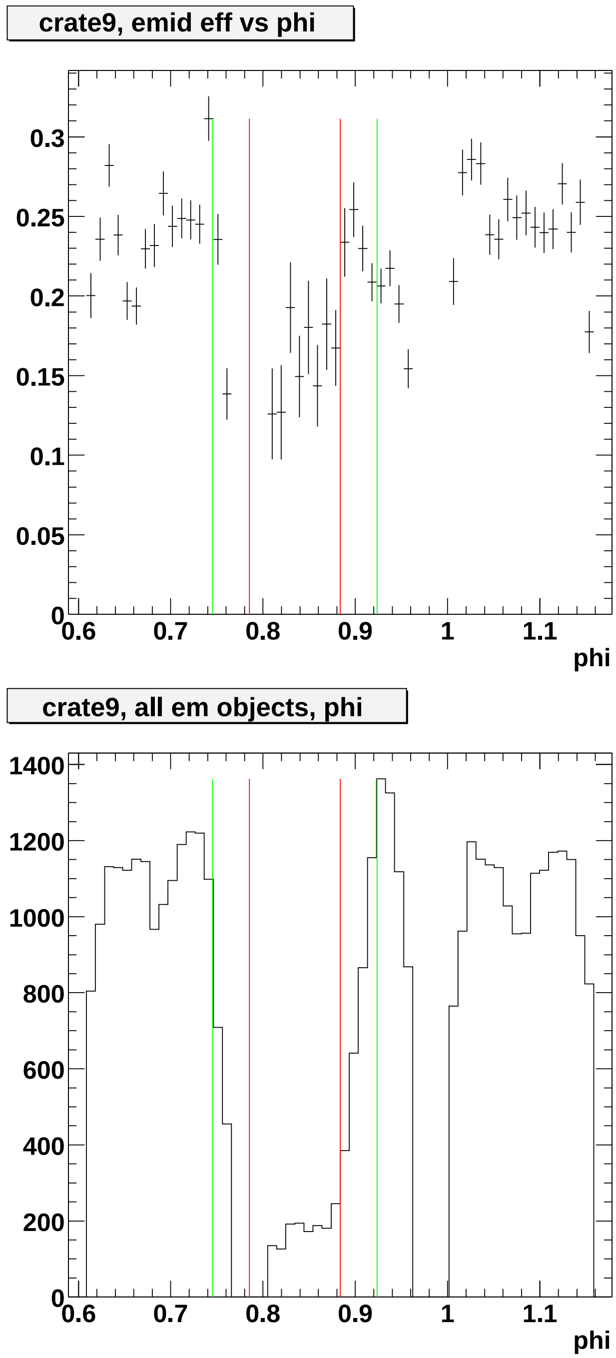

Figure 14: projections along ϕ_{det} of EMid efficiency (top) and all EM objects passing acceptance (bottom) for cells with "energy sharing". The red lines indicate cell boundaries and the green lines indicate where data are cut.

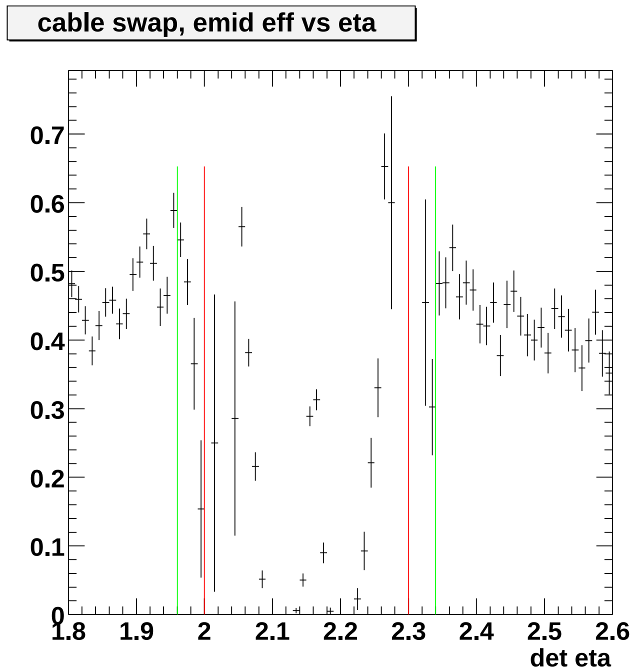

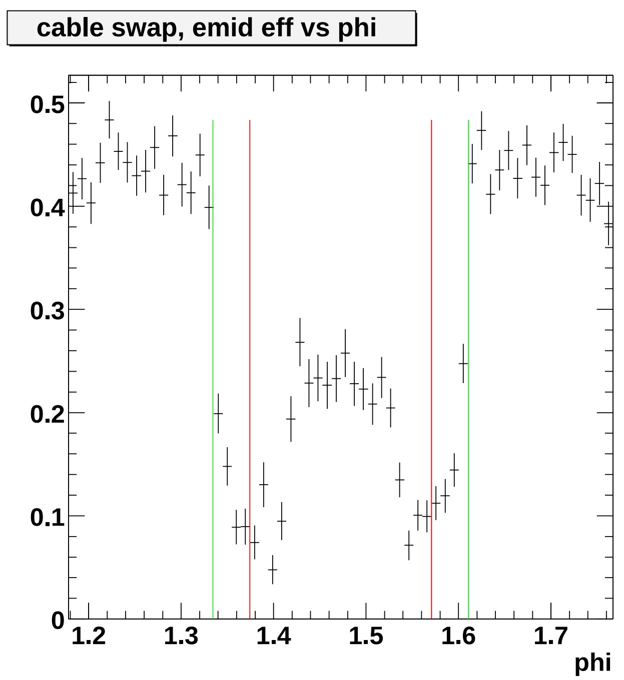

Figure 15: projections along (top)η_{det} and (bottom)ϕ_{det} of EMid efficiency vs position relative to the cells with cables swapped. The red lines indicate cell boundaries and the green lines indicate where data are cut.

3 Event Selection

3.1 Trigger Selection

Events which enter into the final Z and W candidate samples are selected from a combination of unprescaled single EM triggers. For an event to be used, a candidate electron must fire one of these triggers. Listed below, is the preferred order of trigger combinations to use based on which are unprescaled.

global CMT 8 to 11 trigger combinations (runs $\leq$ 178721)

- EM_HI_SH or EM_HI_2EM5_SH
- EM_HI_SH
- EM_HI
- EM_MX_SH
- EM_MX.

global CMT 12 trigger combinations (runs $\geq$ 178722)

- E1_SHT20, E2_SHT20, E3_SHT20 or E1_SH30
- E1_SHT20, E2_SHT20 or E1_SH30
- E1_SHT20 or E1_SH30
- E1_SHT20

For runs $\geq$ 174845, The level 1 trigger detector eta coverage was extended from $|\eta_{det}| < 2.4$ to $|\eta_{det}| < 3.2$. For pre global CMT 12 triggers, the level 2 and level 3 eta coverage is $|\eta_{det}| < 3.0$ and all CMT 12, L3 triggers cut on physics eta where $|\eta_{physics}| < 3.6$. Due to these eta coverages, a maximum $|\eta_{det}|$ of 2.3 is used. See Table 1 for a trigger summary.

3.2 Electron Selection

Electrons are selected using the version of EMcandidate dated 10 December 2003 and applying the quality cuts recommended by the EMID group. Electromagnetic objects have to satisfy the following requirements:

- Preselection cuts:
  - ID = 10 OR $\pm$ 11
  - EMFraction > 0.9
  - Isolation < 0.15
- Kinematic and fiducial cuts:
  - $E_T > 25$ GeV

trigger	L1	L2	L3
EM_HI_SH	CEM(1,10)	EM(1,12)	ELE_LOOSE_SH_T(1,20)
EM_HI_2EM5_SH	CEM(2,5)	EM(1,12)	ELE_LOOSE_SH_T(1,20)
EM_HI	CEM(1,10)	EM(1,12)	ELE_LOOSE(1,30)
EM_MX_SH	CEM(1,15)	none	ELE_LOOSE_SH_T(1,20)
EM_MX	CEM(1,15)	none	ELE_LOOSE(1,30)
E1_SHT20	CEM(1,11)	none	ELE_NLV_SHT(1,20)
E2_SHT20	CEM(2,6)	none	ELE_NLV_SHT(1,20)
E3_SHT20	CEM(1,9)CEM(2,3)	none	ELE_NLV_SHT(1,20)
E1_SH30	CEM(1,11)	none	ELE_NLV_SH(1,30)

L1 triggers

CEM(1,10)	one EM trigger tower with $E_T > 10GeV$
CEM(2,5)	two EM trigger towers with $E_T > 5GeV$
CEM(1,15)	one EM trigger tower with $E_T > 15GeV$
CEM(1,11)	one EM trigger tower with $E_T > 11GeV$
CEM(2,6)	two EM trigger towers with $E_T > 6GeV$
CEM(1,9)CEM(2,3)	one EM trigger tower with $E_T > 9GeV$, another EM trigger tower with $E_T > 3GeV$

L2 triggers

EM(1,12)	one EM candidate with $E_T > 12GeV$ (not present for runs below 169524)

L3 triggers

ELE_LOOSE_SH_T(1,20)	one electron with $\|\eta\| < 3.0$ and $E_T > 20GeV$ passing loose requirements including shower shape cuts
ELE_LOOSE(1,30)	one electron with $\|\eta\| < 3.0$ and $E_T > 30GeV$ passing loose requirements
ELE_NLV_SHT(1,20)	one electron with $\|\eta\| < 3.6$ and $E_T > 20GeV$ passing tight shower shape cuts
ELE_NLV_SH(1,30)	one electron with $\|\eta\| < 3.6$ and $E_T > 30GeV$ passing loose shower shape cuts

Table 1: Single EM triggers

    - central($|\eta| < 1.05$) OR $1.5 < |\eta| < 2.3$ for Z sample
    - central($|\eta| < 1.05$) for W sample ($1.7 < |\eta| < 2.3$ also shown).
    - 'is_in_fiducial' in EMCandidate
    - Not in a problematic calorimeter region

- Loose electron:
    - EM object satisfying preselection, kinematic and fiducial cuts.
    - Track match with $P(\chi^2) > 0.01$

- Tight electron:
    - Loose electron
    - Electron Likelihood > 0.9

Electromagnetic clusters from EMReco are assigned an ID of 10 if they have $E_T > 1.5$ GeV and EMFraction > 0.9. If the cluster also has a track loosely matched to it, it is given an ID of ± 11 depending on the sign of the track (note: electrons are given an ID of +11 and positrons are given an ID of -11). The isolation variable is defined as

$$\text{iso} = \frac{E_{tot}(0.4) - E_{EM}(0.2)}{E_{EM}(0.2)} \tag{1}$$

where $E_{tot}(R)$ and $E_{EM}(R)$ denote the total energy and EM energy within a cone of radius R.

The fiducial requirement avoids cryostat edges and removes electron candidates within 0.1 in phimod of the ϕ gaps due to module boundaries. Calorimeter quality cuts refer to the calorimeter areas that have an identified hardware problem as discussed in Section 2. The electron likelihood is described in detail in Section 4.4. The track matching criteria is described in detail in Section 4.2. The E_T of the electron is calculated using the position and energy of the EM cluster energy and the primary vertex (or a vertex of $(0,0,0)$ if there is no vertex. Less than 0.4% of events do not have a primary vertex so this does not pose a significant problem.

3.3 Missing E_T

For W candidates a Missing Transverse Energy (MET) of 25GeV is required. The W missing E_T distribution using the electron corrected variable ("eleMET") and the W p_T distribution are shown in figure 18.

3.4 Z Event Selection

Z candidate events have to fulfill the following requirements:

- At least two electron candidates satisfying preselection, kinematic and fiducial cuts

- At least one central tight electron
- One of the electron candidates must have fired the trigger.
- di-EM invariant mass between 70 and 110 GeV

The two electron candidates with the highest p_T are selected to form a Z if there are more than 2 candidates. 5174 Z candidates with both electrons in the central region (CC-CC) and 2754 with one electron in the central region and one in the end cap (CC-EC) have been selected for a total of 7928 Z candidates before background subtraction.

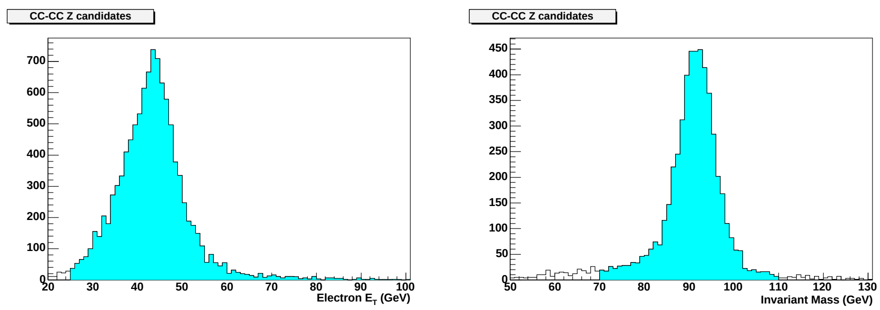

Figure 16: Z candidate CC-CC electron E_T and invariant mass distributions.

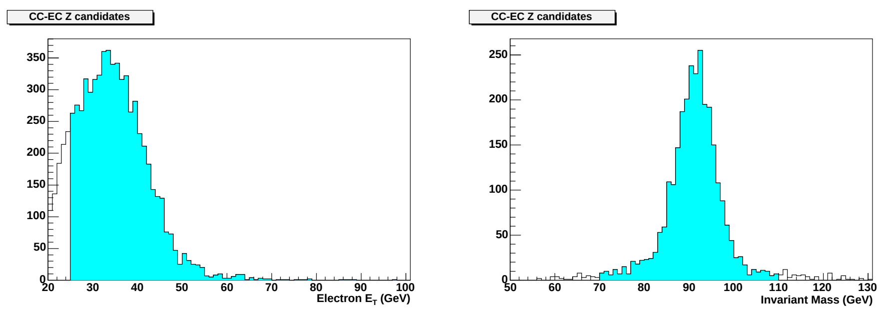

Figure 17: Z candidate CC-EC electron E_T and invariant mass distributions.

3.5 W Event Selection

The criteria for the W event selection are:

- W candidate (loose):
  - At least one central loose electron

– The electron candidate must have fired the trigger.

– Missing $E_T > 25$ GeV.

A tighter sample is also required for background subtraction.

- Tight W candidate:
  - W candidate
  - The electron must satisfy tight electron requirements.

In total, 97,757 W candidates have been selected and 85,947 satisfy the tight requirement.

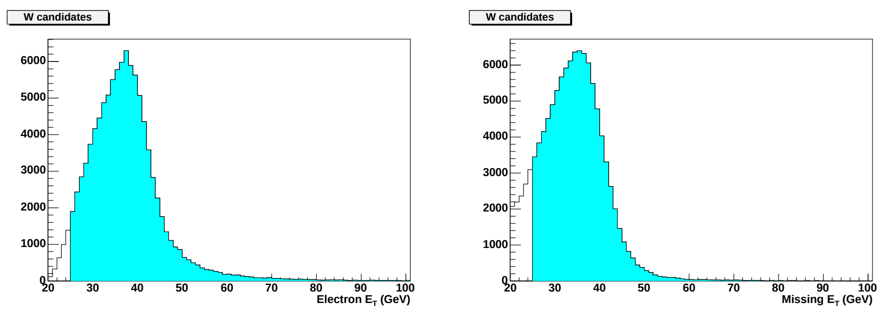

Figure 18: W candidate electron E_T and MET distributions.

4 Efficiencies

Efficiencies are found with a tag-probe method using Z candidate events. The tag is always required to satisfy requirements of a tight electron. Additionally, the tag must pass trigger requirements for at least one unprescaled trigger in the trigger combination. For all tag-probe efficiencies if two tight electrons are found they are both considered as possible tags with the other electron becoming the probe. Efficiencies are applied in the following order:

- Preselection
- Track Matching
- Trigger
- Electron Likelihood

The probe electron must satisfy cut requirements of all previous efficiencies. This method allows us to determine the efficiency as a function of another variable, such as $\eta_{\mathrm{d}et}$ and p_T. One disadvantage of this method is that background subtraction can be difficult. This is mainly a concern for preselection and track matching efficiencies. For trigger and electron likelihood efficiencies, background is extremely small since the probe must already have a track match.

4.1 EMID Preselection Efficiency

The preselection efficiency is defined as the efficiency for an electron satisfying the kinematic and geometric requirements to form an EM cluster passing the following cuts:

- ID = 10 OR $\pm$ 11
- EM fraction > 0.9
- isolation < 0.15

An unbiased method not using calorimeter information needs to be employed to study the preselection efficiency. Fiducial cuts similar to those used for determining geometric acceptance are made with the exception of the central phi fiducial cut. For PMCS, efficiency in the central calorimeter is measured as a function of phimod and must include the ϕ crack regions. To study dependence on other variables it is desired to only measure efficiency of electrons in the phi fiducial region. For this, the probe track is required to be an additional 0.025 phimod units away from the phi module boundaries. The extension to this cut is necessary to ensure the matching EM cluster is within the fiducial region. For all tracks except the tag, η_{det} and ϕ_{det} positions are found by extrapolating to the third floor of the calorimeter. For an event to be included in the probe sample, there must be a good tag electron and a second track with the following properties:

- $27 < p_T < 80\ GeV$
- stereo track
- $|\eta| < 3.2$
- $\chi^2 < 8$ and DCA < 0.3 cm
- no muon within $\Delta R_{\eta-\phi} < 0.02$
- Δz_{vertex} of the two tracks $< 4\ cm$
- $\Delta\phi$ of the two tracks > 2 rad
- invariant tag-electron probe-track mass within $70 < M < 105\ GeV$.

The track with highest p_T is selected as the probe track if more than one track fulfills the above requirements.

Electromagnetic clusters are successfully matched to the track if they are within $\Delta R(\eta_{physics}, \phi_{physics}) < 0.1$ of the extrapolated track position. Z candidates that are matched to two tracks with the same sign are used for background studies. Before matching, the same sign track sample contains mainly background events whereas after matching the same sign track sample contains mainly signal events. Therefore, Z candidates with same sign tracks are counted as signal events if an EM match is found and background if not.

The efficiency is defined as

$$\epsilon_{presel} = \frac{\#\text{ probes with matching EM cluster}}{\text{total probe tracks}} \tag{2}$$

Defining opposite sign tracks passing the EM match requirement as P_O, failing as F_O, passing with same sign tracks as P_S and failing same sign as F_S gives the background subtracted preselection efficiency.

$$\epsilon_{presel} = \frac{P_O + P_S}{(P_O + P_S) + (F_O - F_S)} \tag{3}$$

Figure 19 shows the invariant mass distributions for these four samples. The uncertainty on ϵ_{presel} can be calculated by writing it in terms of the statistically independent samples P defined as $P_O + P_S$ and F defined as $F_O - F_S$:

$$\epsilon_{presel} = \frac{\text{P}}{\text{P+F}}. \tag{4}$$

The uncertainty is then

$$\delta\epsilon_{presel} = \sqrt{\frac{(F\delta P)^2 + (P\delta F)^2}{(F+P)^4}}, \tag{5}$$

where δP and δF are the statistical uncertainties of the samples P and F.

$$\delta P = \sqrt{P_0 + P_S}\ , \quad \delta F = \sqrt{F_0 + F_S} \tag{6}$$

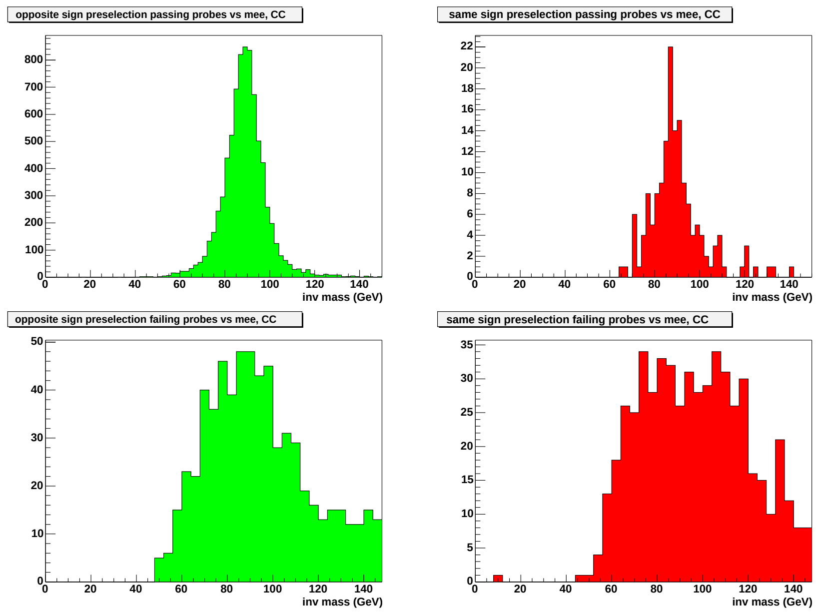

Figure 19: Invariant mass of the tag electron and probe track for the independent samples used in determining efficiency for CC. Plots are of opposite sign tracks (left side), same sign (right side), passing preselection cuts (top half) and failing cuts (bottom half).

The numbers obtained from the mass distributions within the mass window $70 < M < 105\ GeV$ for CC are $P_O = 6692$, $P_S = 76$, $F_O = 132$ and $F_S = 72$. The same figures for the EC region are $P_O = 1298$, $P_S = 45$, $F_O = 56$ and $F_S = 41$. Using these to calculate an average preselection efficiency per electron one gets:

$$\epsilon_{\mathrm{pre}}^{CC} = (99.1 \pm 0.2)\% \tag{7}$$

$$\epsilon_{\mathrm{pre}}^{EC} = (98.9 \pm 0.7)\%. \tag{8}$$

The $\eta_{\mathrm{d}et}$ distribution of the probe track is used to determine the preselection efficiency as a function of $\eta_{\mathrm{d}et}$. The background subtraction is again performed using same sign tracks as shown in figure 20. The resulting efficiency shown in figure 21 is used in PMCS for EC only. For CC, it is necessary due to calorimeter ϕ shifts, see section 2.1, to use preselection efficiency as a function of phimod. See figure 22. Additional plots include efficiency vs. E_T in figure 25, ϕ_{det} in figure 26, run number in figure 27 and instantaneous luminosity in figure 28.

One source of systematic uncertainty is estimated by studying the variation of the preselection efficiency in ϕ and for $|\eta_{\mathrm{d}et}| < 0.7$ where the efficiency is expected to be constant and very close to one. From these variations, a relative uncertainty of 0.5% is estimated. Additionally, full monte carlo checks indicate an upward bias of 0.4% from the use of a track in the tag-probe method. This is based on the observed increase in average CC efficiency when a track is required as shown in figure 114. An additional check was done for uncertainty arising from number of jets. Preselection efficiency does drop with the presence of jets as shown in figure 23. However comparisons with full monte carlo show good agreement. Combining these sources yields a 0.7% total systematic for preselection efficiency.

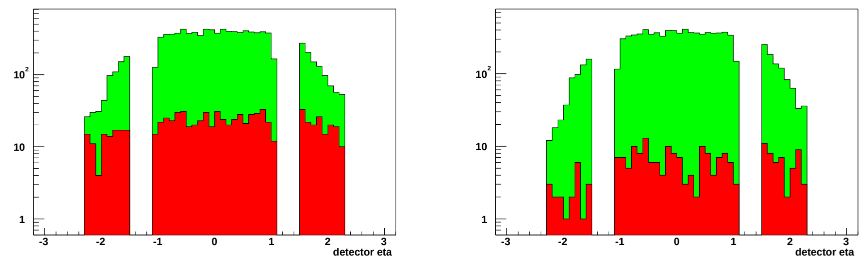

Figure 20: η_{det} distribution of probe tracks from Z candidates with opposite (green) and same sign (red) tracks for all probe tracks (left) and probe tracks with a matched EM cluster (right).

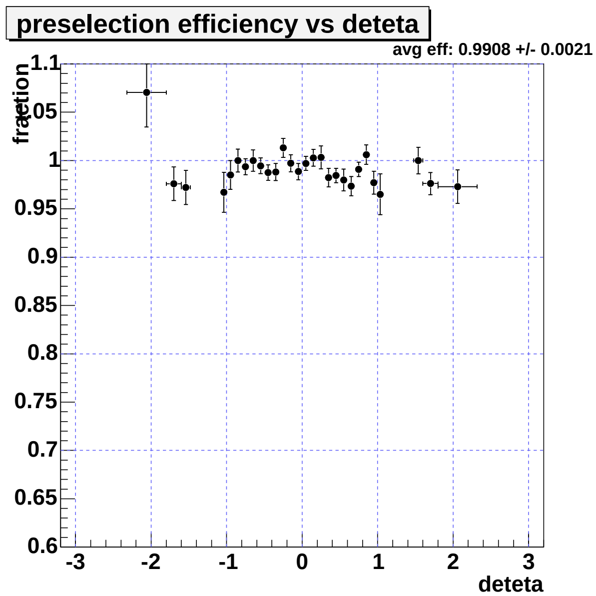

Figure 21: preselection efficiency after background subtraction as a function of η_{det}, used in PMCS for EC.

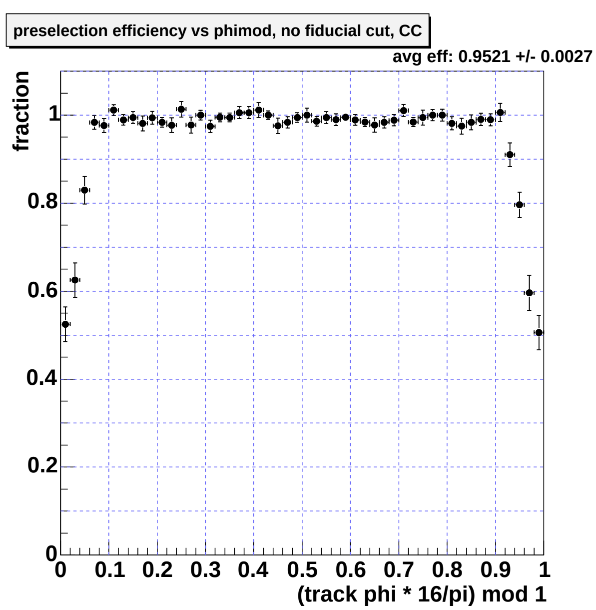

Figure 22: preselection efficiency after background subtraction as a function of phimod, used in PMCS for CC

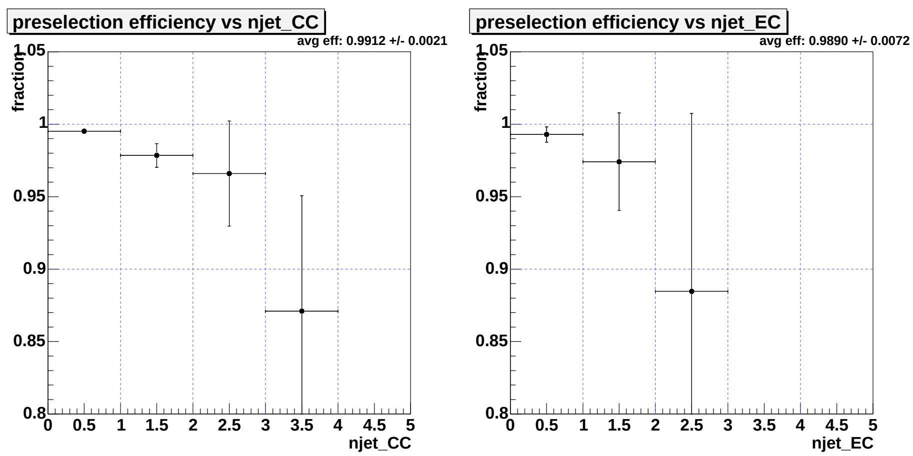

Figure 23: preselection efficiency after background subtraction as a a function of number of jets for CC (left) and EC (right)

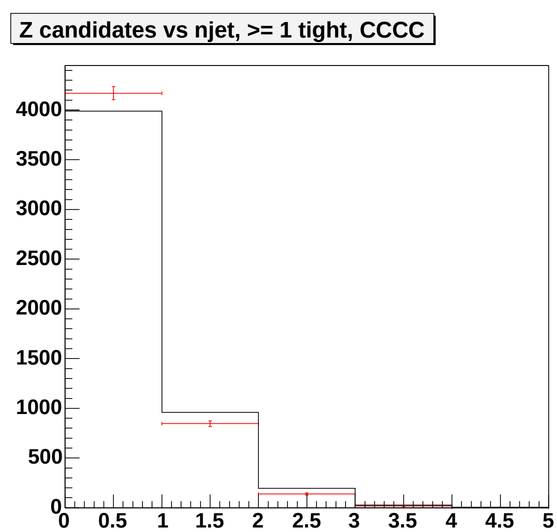

Figure 24: A data(blue dots) to full MC(red histogram) comparison of number of jets for Z CC-CC

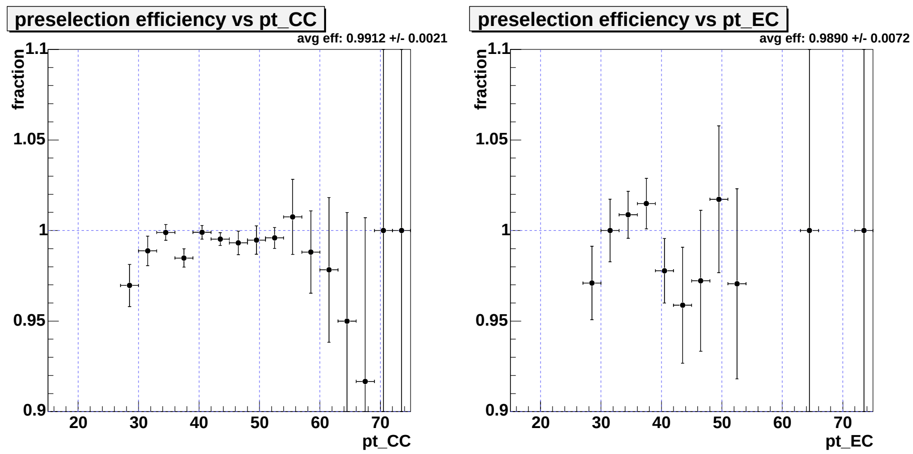

Figure 25: preselection efficiency after background subtraction as a a function of E_T for CC (left) and EC (right)

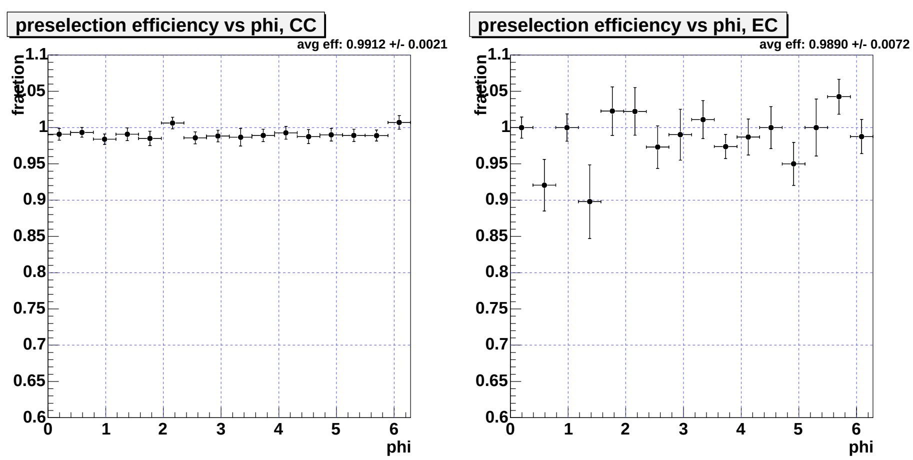

Figure 26: preselection efficiency after background subtraction as a function of ϕ_{det} for CC (left) and EC (right)

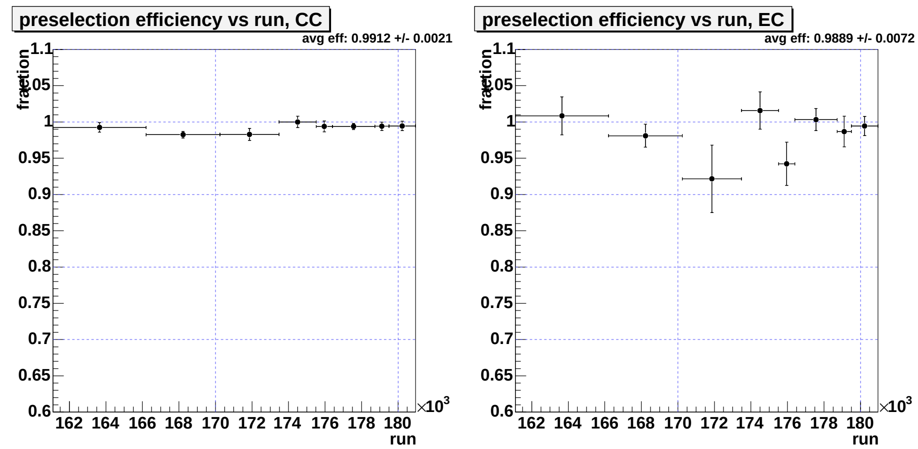

Figure 27: preselection efficiency after background subtraction as a function of run number for CC (left) and EC (right)

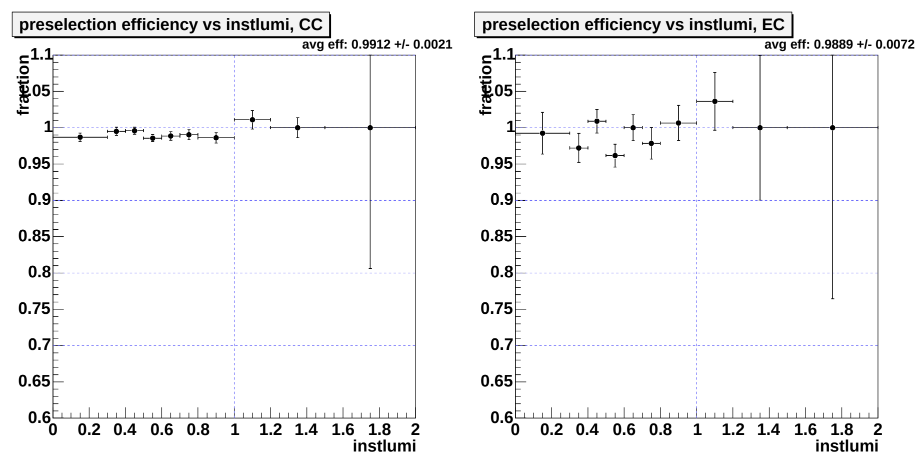

Figure 28: preselection efficiency after background subtraction as a function of instantaneous luminosity ($10^{30} cm^{-2} s^{-1}$) for CC (left) and EC (right)

4.2 Track Matching Efficiency

The track matching algorithm used in this analysis is found in the em_util package and includes a cut on the χ^2 of the track match.

$$\chi^2_{CC} = \left(\frac{\Delta z}{\sigma(z)}\right)^2 + \left(\frac{\Delta\phi}{\sigma(\phi)}\right)^2 + \left(\frac{E_T/p_T - 1}{\sigma(E_T/p_T)}\right)^2 \tag{9}$$

$$\chi^2_{EC} = \left(\frac{\Delta z}{\sigma(z)}\right)^2 + \left(\frac{\Delta\phi}{\sigma(\phi)}\right)^2 \tag{10}$$

In the above expression, Δz and $\Delta\phi$ are the differences between the track position and the EM cluster position at the third floor of the calorimeter; E_T/p_T is the transverse energy of the EM cluster as measured by the calorimeter divided by the transverse momentum of the track; and the σ variables are the root-mean-squares of the experimental measurements of each quantity. In the EC region of the calorimeter the E_T/p_T term in the χ^2 is not used. For a good track match, the track matching χ^2 probability cut is $P(\chi^2) > 10^{-2}$. To give an idea of the level of matching required, for CC this is roughly $\Delta z < 2.4cm$, $\Delta\phi < 0.02$ rad or $|E_T/p_T - 1| < 0.6$ when the other terms are zero.

It is important that at least one electron with a matched track is present in an event. With no track match requirement, approximately 4% of events have no primary vertex compared to less than 0.4% with a track. Additionally, comparing track z0 positions to the primary vertex indicates that primary vertex z is biased toward lower z as shown in figure 29. For this reason, track z0 of the highest p_T electron is used in place of the primary vertex for all efficiencies dependent on primary vertex. A track z0 reliability check, plotting the difference in track z0's for electrons in Z events as shown in figure 30, demonstrates excellent track z0 consistency. Although treating track z0 as the vertex lowers the percent of events with no vertex to 0.4%, there is still an issue with the primary vertex z bias toward zero. The main concern is the use of an incorrect primary vertex when reconstructing MET for W candidate events and E_T for an electron with no track match in Z candidate events. Including events with no primary vertex(z = 0), nearly 4% of W candidates have a primary vertex defined more than 20 cm away from the high p_T electron track z0. To model this in PMCS, a plot of W candidate (vertex z - track z0) vs. track z0, shown in figure 31, is input into PMCS. This shift is applied to EM particles to alter E_T at the point in the PMCS code where MET is calculated. E_T is only smeared in this way for the MET calculation since track z0 is used in electron measurements. The change in acceptance with this smearing is less than 0.1%. The other concern is Z electrons with no track match. However, this is considered negligible since a much smaller percentange, at only 0.6%, of Z events have both an electron without a track match and poor agreement with the primary vertex.

The tag-probe method is used with the probe electron required to pass preselection cuts to be considered. Background is large enough in this sample so that its contribution must be carefully taken into account. The probe sample di-EM mass distributions are fit to the QCD background shape estimated from data

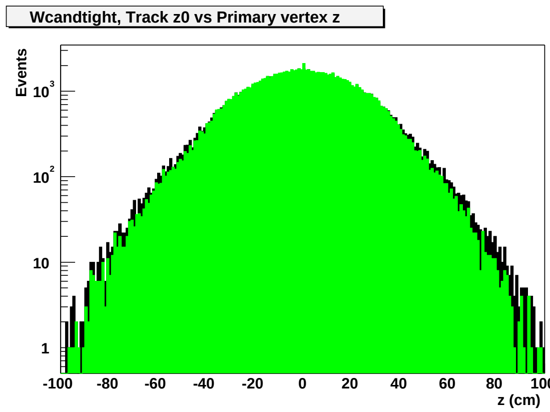

Figure 29: W candidate tight sample track z0 (black) vs primary vertex z (green) showing bias of vertex z toward zero.

plus a signal shape estimated from the tuned PMCS sample. Fitting is done separately for CC-CC, CC-EC and EC-EC events as shown in figure 32 resulting in background fractions of 1.3%, 2.3% and $< 1\%$ respectively. The background invariant mass distribution is estimated using the QCD background shape defined in section 5.1.1.

The track match efficiency is then the ratio of the number of events where the probe cluster has a good track match to the total number of kept events, after background subtraction. The track matching efficiencies vs detector and physics eta are shown in figure 33, as a function of electron E_T in figure 34, detector phi in figure 35, run in figure 36, instantaneous luminosity in figure 37, tick number in figure 38 and phimod in figure 39. In the central region, the efficiency is fairly steady with an average of $(77.4 \pm 0.4)\%$. In the EC region, $1.5 < |\eta| < 2.3$, the efficiency varies greatly ranging from 50% to 95% with an average of $(72.1 \pm 0.8)\%$. The overall efficiency is $(76.1 \pm 0.4)\%$.

For the PMCS simulation, track match efficiency vs η_{det} is binned according to primary vertex z position. While fairly stable in the CC region, efficiency varies greatly for EC dropping to practically nothing for high z vertex when the electron is on the same side. See figure 40 for plots vs η_{det} for all z vertex bins.

To test uncertainty in the background measurement, several different background shapes were produced by altering the background selection cuts. Variations in the background fraction resulting from these different shapes were less than 0.5 percent from the chosen shape. From this, a 0.5% relative systematic uncertainty on the track-match efficiency is assigned.

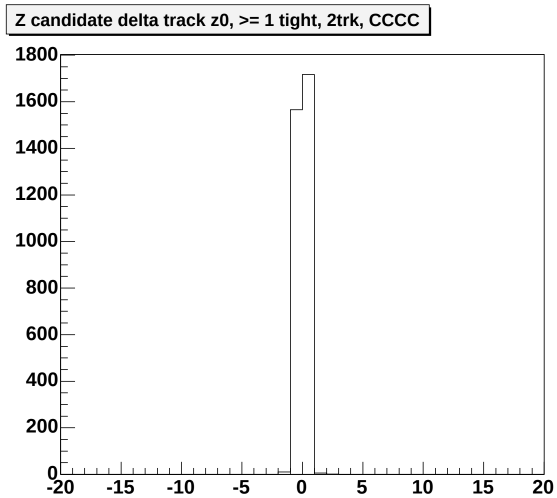

Figure 30: Histogram showing difference in Track z0's(cm) for CC-CC Z candidate events. Underflow and overflow bins at ± 20cm are visible but empty.

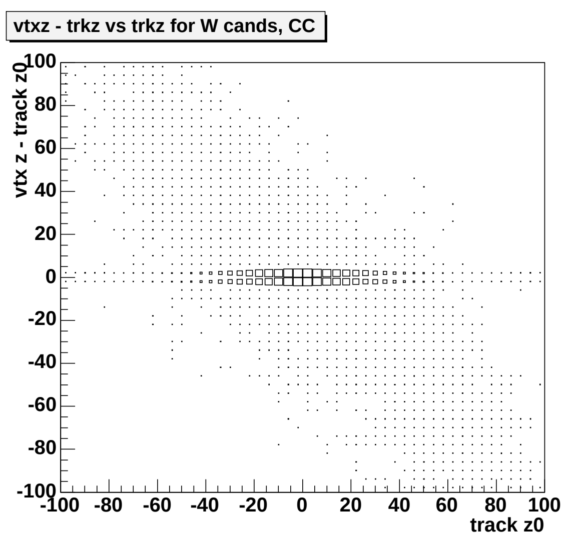

Figure 31: W candidate CC (vertex - track z0) vs track z0 (cm) used to smear the primary vertex in PMCS.

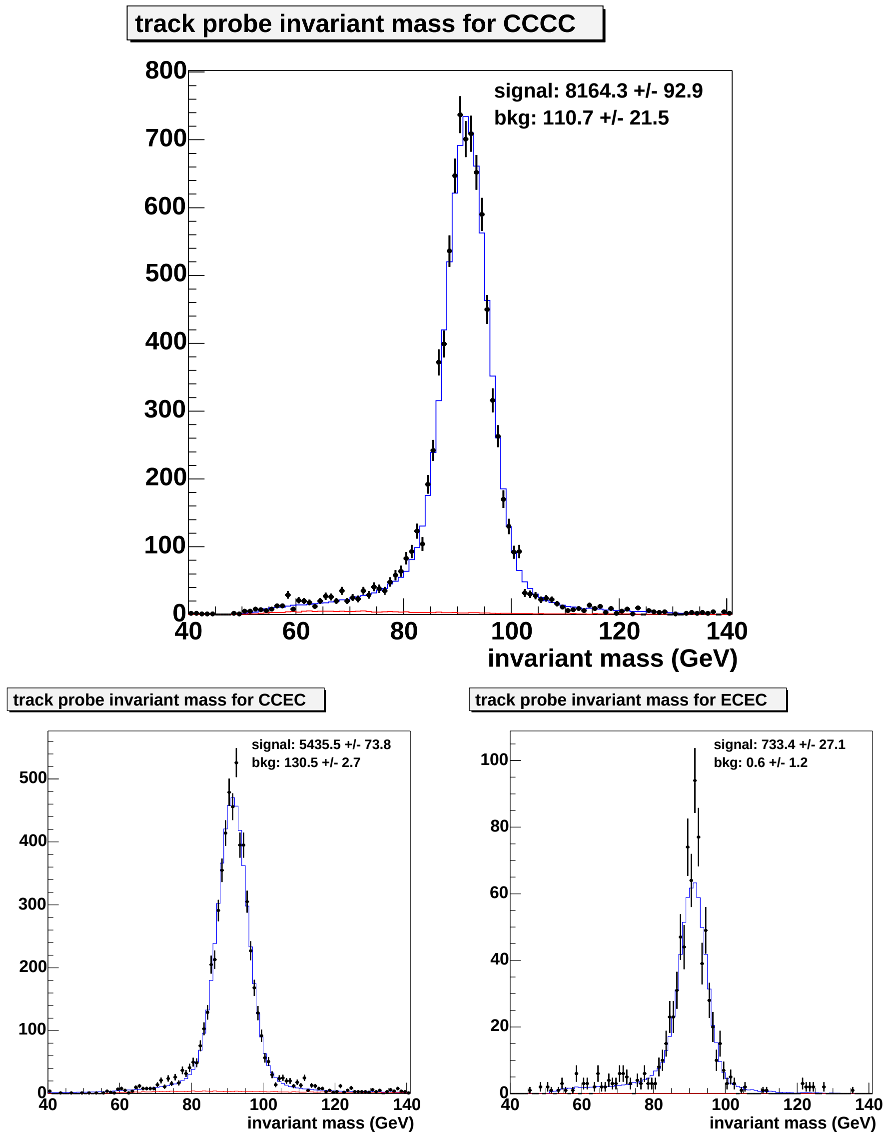

Figure 32: Invariant mass distribution of probes before track requirement for CC-CC (top), CC-EC (left) and EC-EC (right).

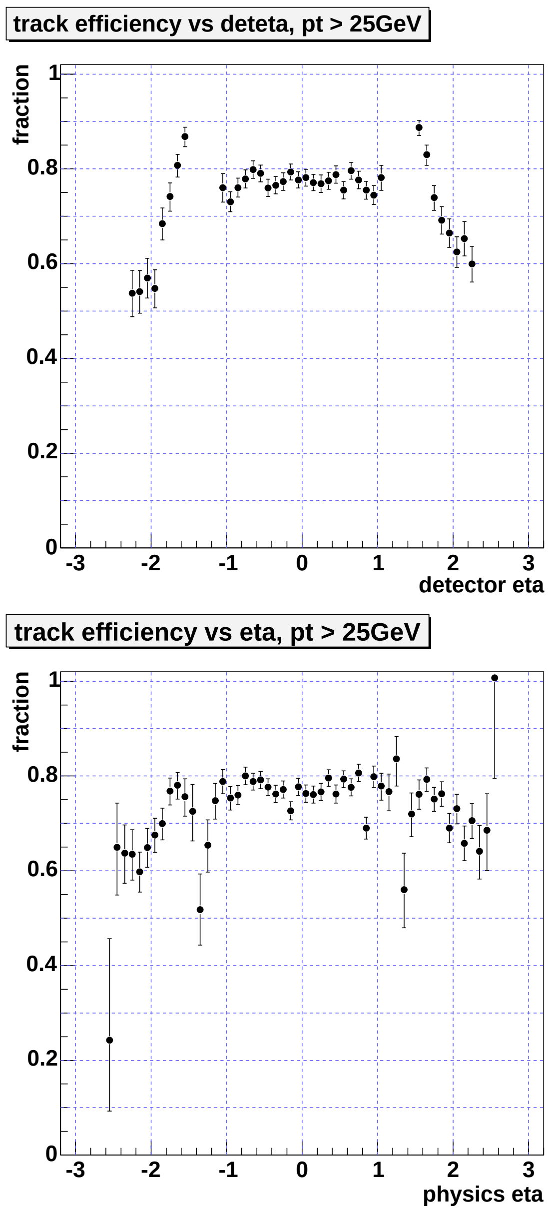

Figure 33: Track matching efficiency vs. η_{det} (top) and η_{phys} (bottom).

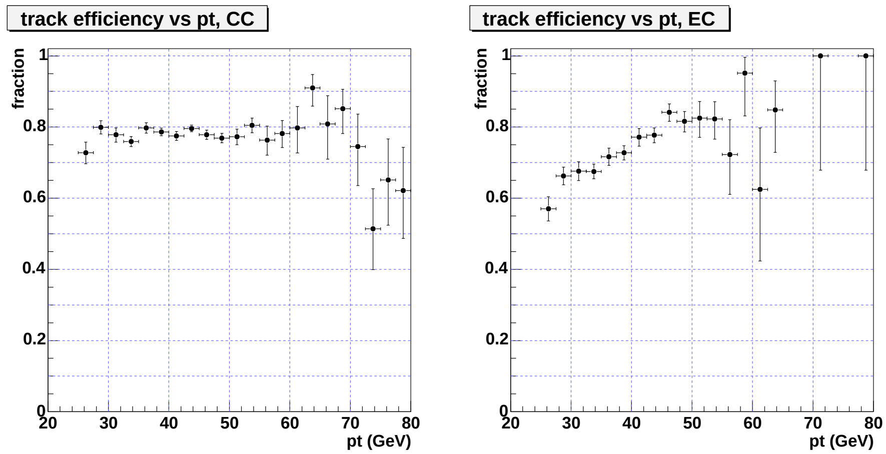

Figure 34: Track matching efficiency vs. E_T for CC (left) and EC (right).

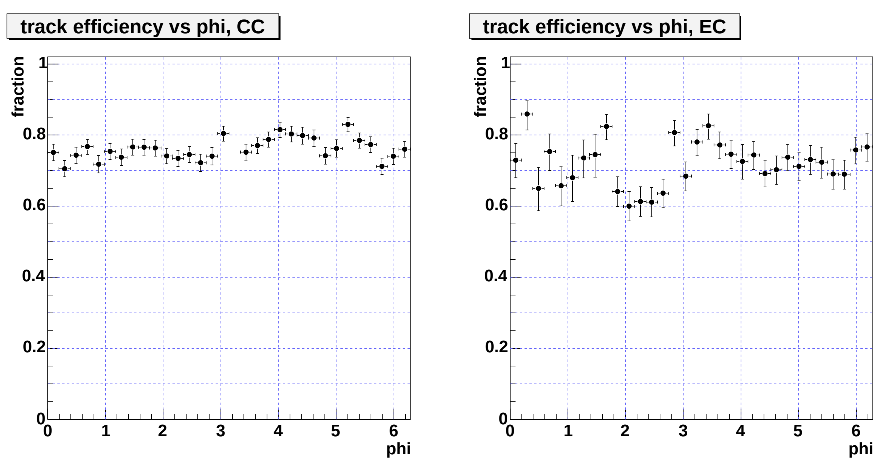

Figure 35: Track matching efficiency vs. ϕ for CC (left) and EC (right).

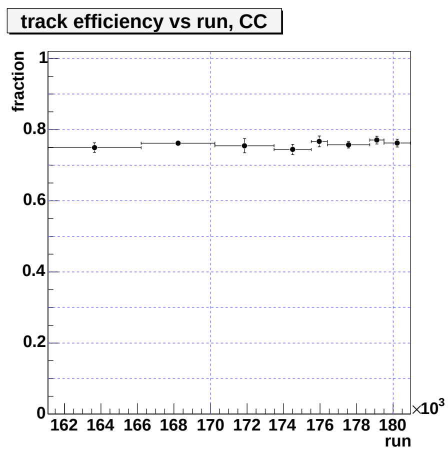

Figure 36: Track matching efficiency vs. run number for CC (left) and EC (right).

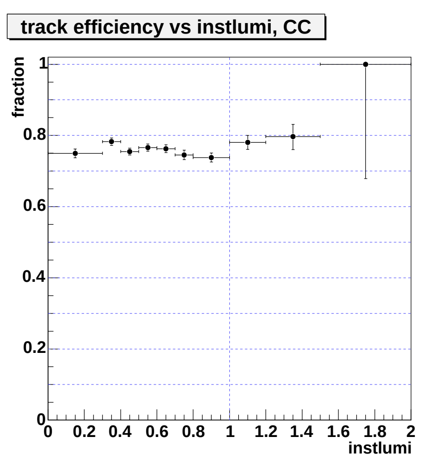

Figure 37: Track matching efficiency vs. instantaneous luminosity ($10^{30} cm^{-2} s^{-1}$) for CC (left) and EC (right).

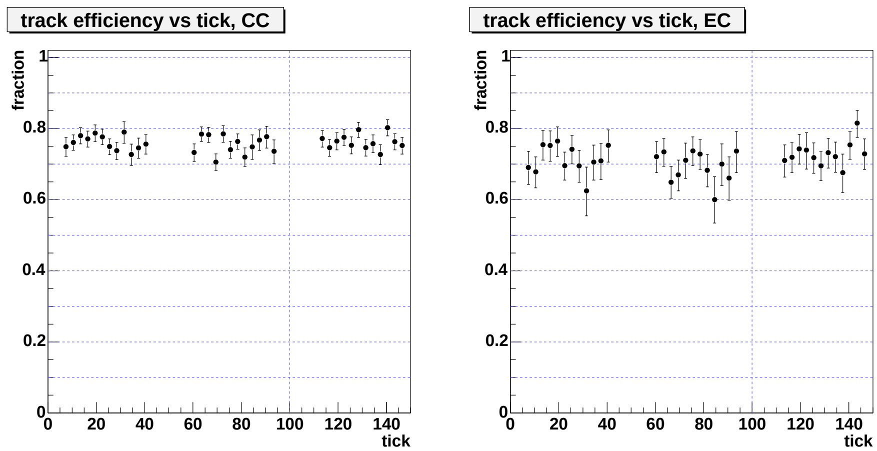

Figure 38: Track matching efficiency vs. tick number for CC (left) and EC (right). This plot shows the 153 ticks, each representing 132 ns or 39.6 m, within the Tevatron circumference. This is divided into 3 groups of 12 bunches, with each bunch in a group separated by 3 ticks.

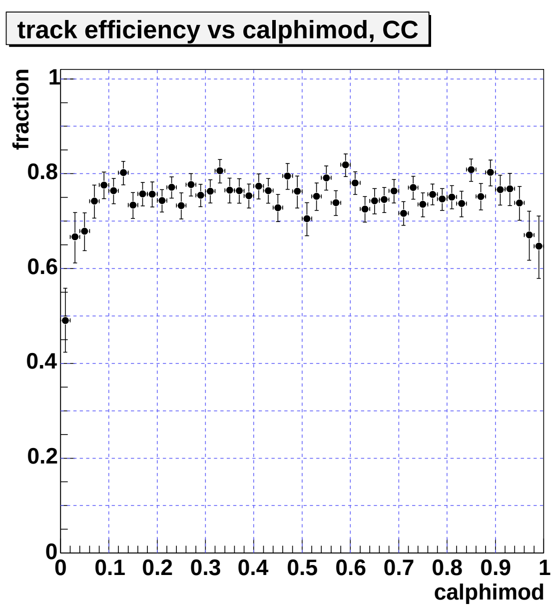

Figure 39: Track matching efficiency vs phimod for CC using EM ϕ_{det}.

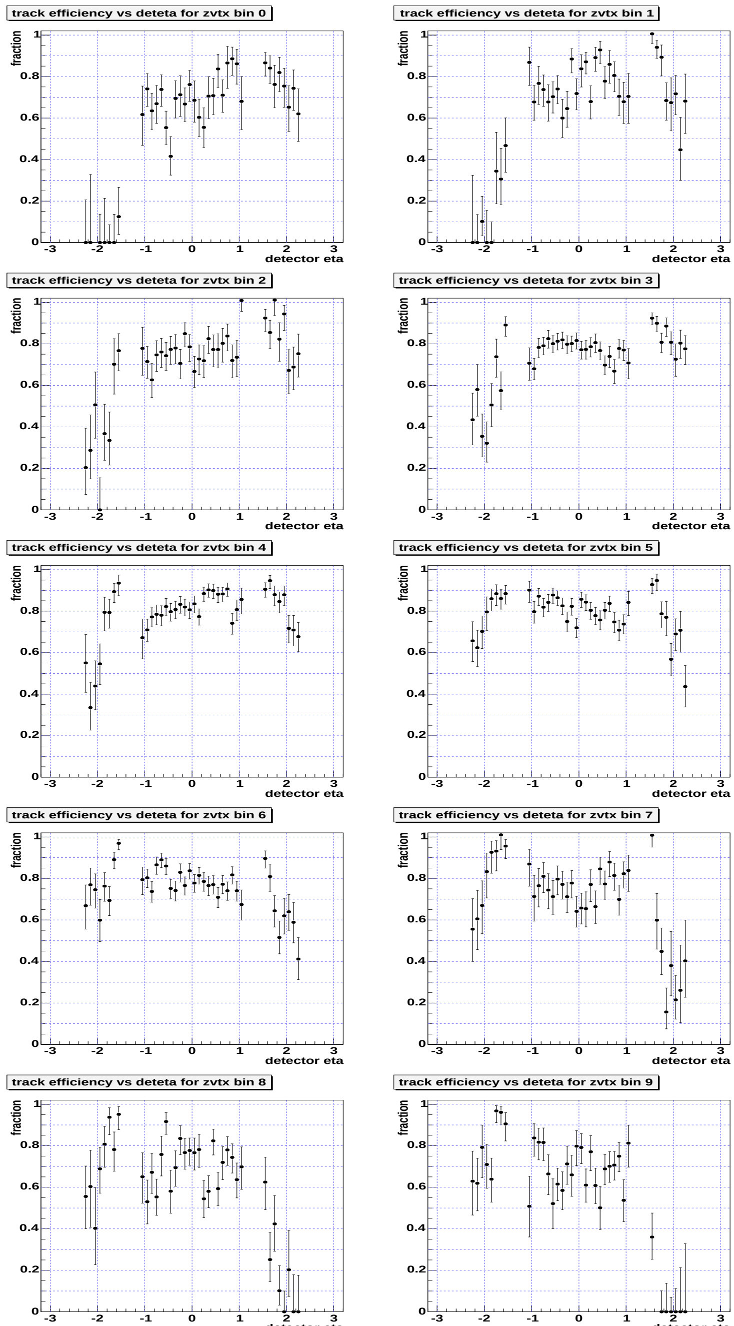

Figure 40: Track matching efficiency vs η_{det} using primary vertex z bins as input into PMCS. Z vertex bins are, going left to right from top to bottom: $<$ -39, -39 to -30, -30 to -23, -23 to -10, -10 to 0, 0 to 10, 10 to 23, 23 to 30, 30 to 39, and $>$ 39 cm.

4.3 Trigger Efficiency

The combined efficiency per electron of all triggers used in the analysis, see section 3.1, is studied with the tag-probe method with the probe required to pass preselection and track match requirements. For this efficiency, the requirement that the "tag" electron passes trigger requirements for at least one unprescaled trigger is especially important. This ensures the probe is not biased by the event trigger requirement. For an electron to pass a trigger's requirements, the EM object must have a matching trigger object at each level which passes all cuts for the corresponding trigger. The electron EM to trigger object matching requirements are:

- L1: $\Delta\phi < 0.4$ (L1 η information not available)
- L2: $\Delta R < 0.4$
- L3: $\Delta R < 0.4$

where $\Delta R = \sqrt{\Delta\phi^2 + \Delta\eta^2}$

A total of 8285 di-EM electrons for runs $\leq$ 178721 and 2949 for runs $\geq$ 178722 are found to satisfy requirements for the "tag". The other electron in the event becomes the "probe" if it has a track match. Trigger efficiency is the fraction of these probes passing the trigger requirements. A total of 8180 probes for runs $\leq$ 178721 and 2896 for runs $\geq$ 178722 pass trigger requirements, yielding average trigger efficiencies of 98.7% and 98.2% respectively.

Trigger efficiency is highly dependent on p_T. Figure 41 shows trigger efficiency for both run ranges as a function of electron p_T in the calorimeter CC region, figure 42 in the EC region with $|\eta_{det}| < 2.3$ and figure 43 with $2.3 < |\eta_{det}| < 3.0$. One method to find an efficiency for a W or Z candidate event to fire a trigger is to weight these efficiency vs p_T distributions by Monte Carlo W and Z electron p_T distributions. Although not used in this cross sections measurement, the resulting efficiencies shown in table 2 are a useful crosscheck.

Figure 44 shows η_{det} dependence for both run ranges. Separating this into two parts for primary vertex z $>$ 0 and z $<$ 0 shows also a z vertex dependence, see figure 45. For this reason, electron trigger efficiencies used in PMCS are binned in p_T, η_{det} and primary vertex z. Figures 46 to 49 show efficiencies in these bins. Additional plots include figure 50 vs. ϕ_{det}, figure 51 vs. run number, figure 52 vs. instantaneous luminosity, figure 53 vs. tick number and figures 54 to 57 showing separate L1 and L3 trigger efficiencies. For more information see [4].

The systematic for Z enters from the measurement of trigger efficiency with a track requirement on the probe when only one of the Z candidate electrons must have a track. Acceptance increases by 0.05% for CC-CC and drops by 0.29% for CC-EC for a combined change of -0.07%.

The systematic for W is estimated from the difference in cross sections measured using CMT 8 to 11 vs CMT 12 triggers. The cross sections are 2924 pb^{-1}

runs $\leq$ 178721	trigger efficiency
W event, electron in CC	$98.0 \pm 0.3\%$
W event, electron in EC	$96.8 \pm 0.6\%$
electron from Z, CCCC event	$99.1 \pm 0.2\%$
electron in CC from Z, CCEC event	$97.4 \pm 0.4\%$
electron in EC from Z, CCEC event	$95.7 \pm 0.5\%$
electron from Z, ECEC event	$98.4 \pm 0.4\%$
Z, CCCC event	$99.992 \pm 0.004\%$
Z, CCEC event	$99.89 \pm 0.02\%$
Z, ECEC event	$99.97 \pm 0.02\%$
runs $\geq$ 178722	trigger efficiency
W eff, electron in CC	$97.8 \pm 0.4\%$
W eff, electron in EC	$94.7 \pm 1.0\%$
electron from Z, CCCC event	$98.9 \pm 0.3\%$
electron in CC from Z, CCEC event	$97.3 \pm 0.5\%$
electron in EC from Z, CCEC event	$93.0 \pm 0.9\%$
electron from Z, ECEC event	$98.1 \pm 0.7\%$
Z, CCCC event	$99.988 \pm 0.006\%$
Z, CCEC event	$99.81 \pm 0.04\%$
Z, ECEC event	$99.96 \pm 0.03\%$

Table 2: p_T weighted event trigger efficiencies. CC is for W event electrons within $|\eta_{det}| < 1.05$ and EC within $1.7 < |\eta_{det}| < 2.3$. CCCC is for Z events with both electrons within $|\eta_{det}| < 1.05$, ECEC with both electrons within $1.5 < |\eta det| < 2.3$ and CCEC with one electron in each region. Errors are binomial. The p_T weight is taken from PMCS generator level electrons. The purpose of this table is to give an overview of what the global efficiencies are. For the cross section number trigger efficiencies are corrected for in bins of $|\eta_{\mathrm{det}}|$, p_T and primary vertex.

binning test	change in Z acc	change in W acc
double E_T bin size	-0.02%	-0.6%
halve E_T bin size	-0.12%	-0.3%
don't use zvtx bins	-0.15%	-0.3%
use 2 CC deteta bins	+0.04%	-0.2%

Table 3:

for CMT 8 to 11 and 2946 pb^{-1} for CMT 12. The systematic is determined to be 0.38% by taking the relative difference divided by two.

Due to the large number of dependencies, rather large bin sizes are necessary in order to have a reasonable number of statistics for every bin. These large bin sizes can result in large jumps from bin to bin at low E_T. To check the stability of the result with bin size, changes in acceptances for W and Z are recorded when different binning choices are made. See table 3 for a summary of results from binning tests.

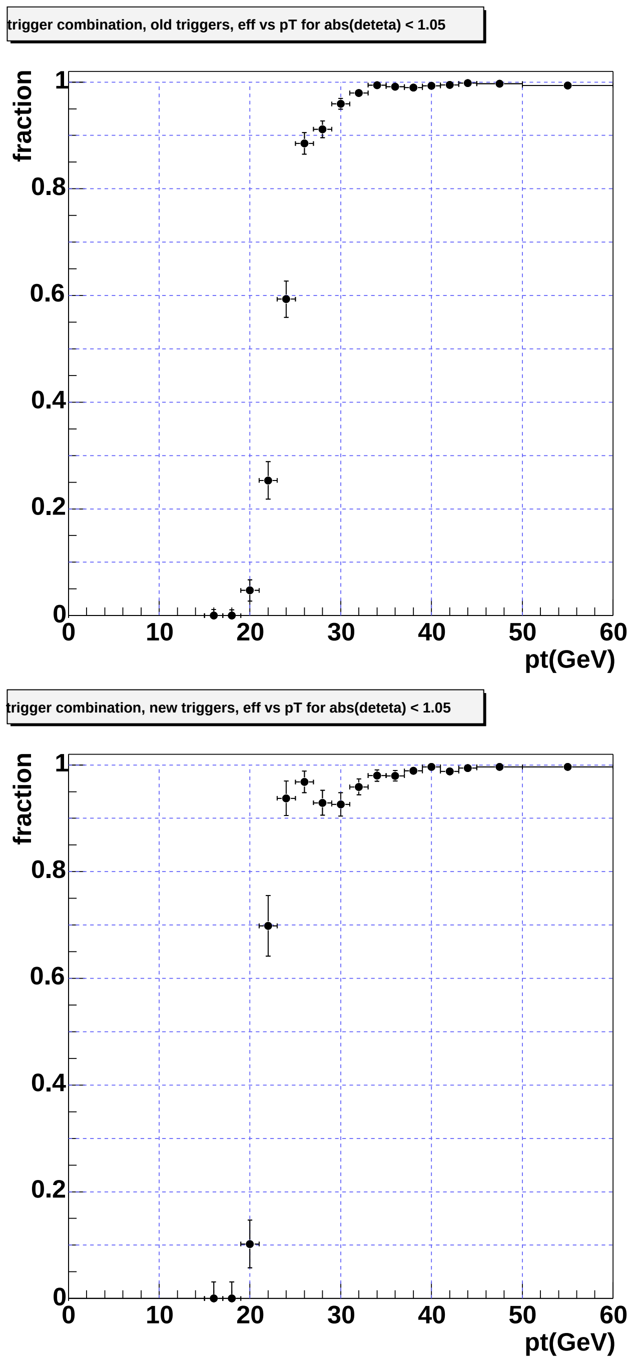

Figure 41: Electron trigger efficiency with respect to p_T in the CC region for runs $\leq$ 178721 (top) and runs $\geq$ 178722 (bottom). The bottom plot shows an odd bump around 25 GeV. This bump is produced by the combination of the two level 3 triggers used in this run range. These level 3 triggers, ELE_NLV_SH and ELE_NLV_SHT, are shown in figure 57.

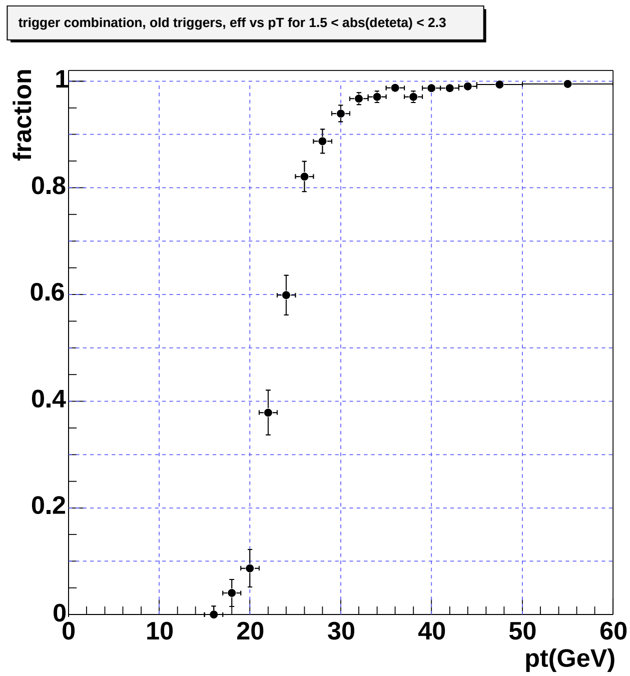

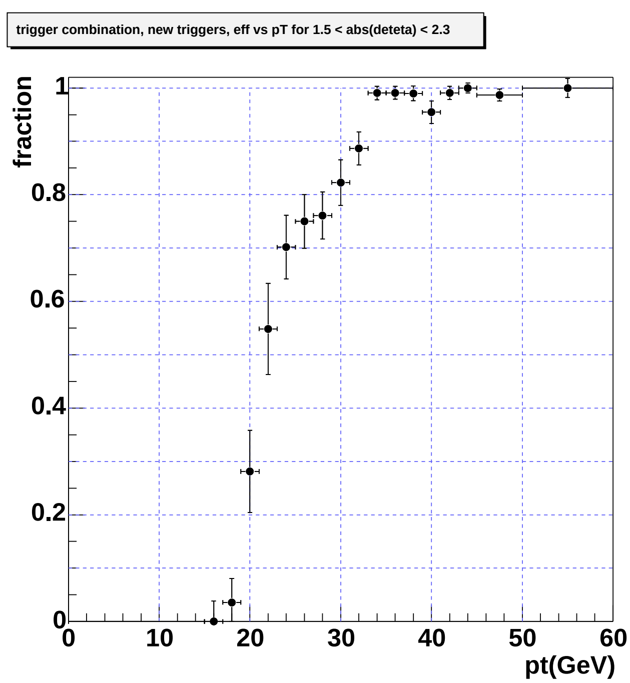

Figure 42: Electron trigger efficiency with respect to p_T in the EC region with $1.5 < |\eta_{det}| < 2.3$ for runs ≤ 178721 (top) and runs ≥ 178722 (bottom).

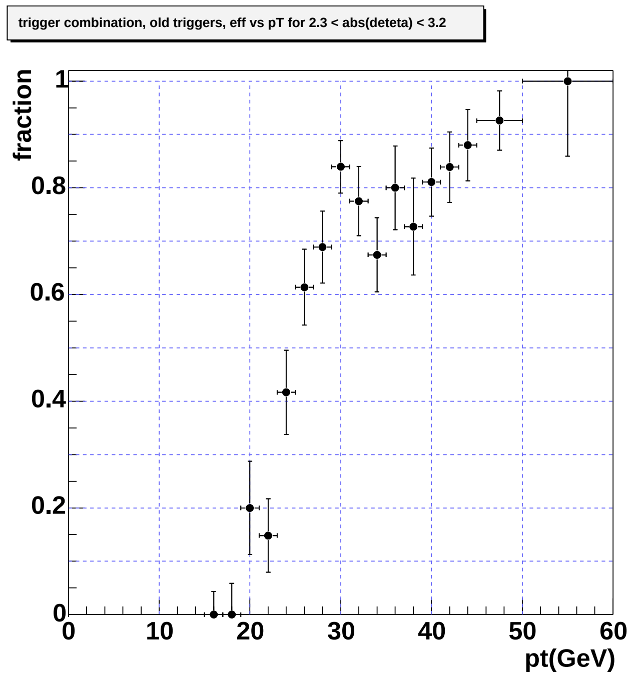

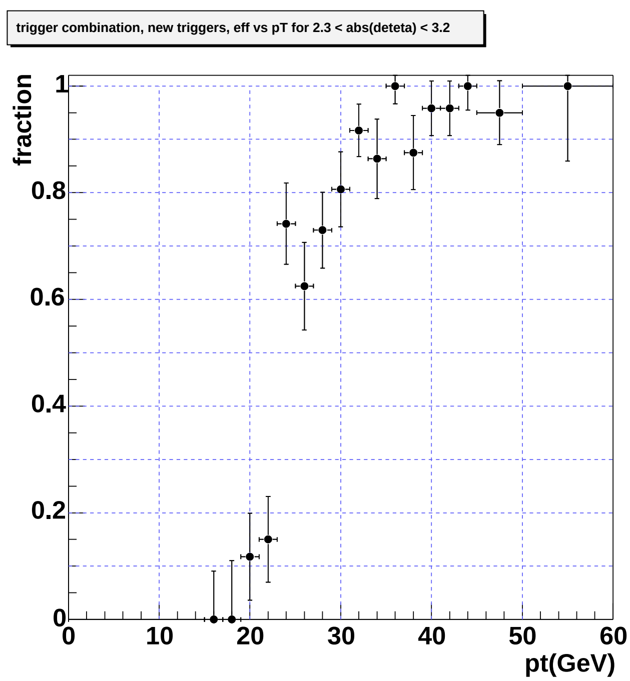

Figure 43: Electron trigger efficiency with respect to p_T in the EC region with $2.3 < |\eta_{det}| < 3.0$ for runs ≤ 178721 (top) and runs ≥ 178722 (bottom).

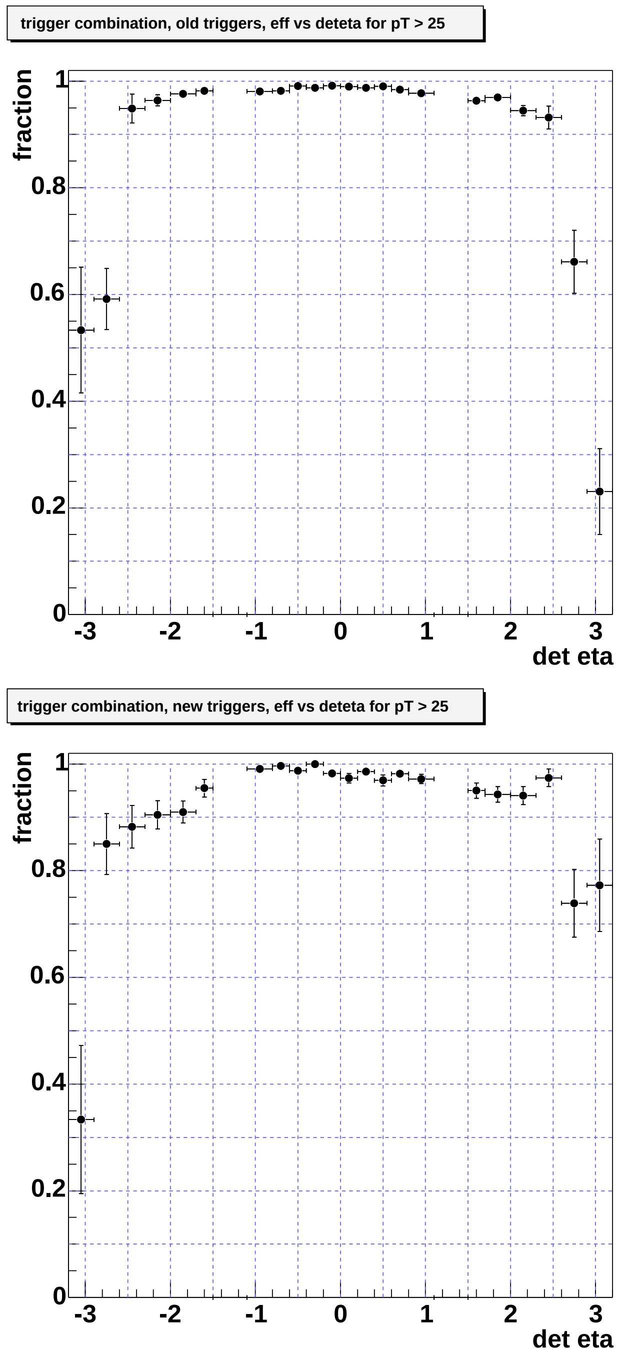

Figure 44: Electron trigger efficiency with respect to detector eta for runs $\leq$ 178721 (top) and runs $\geq$ 178722 (bottom).

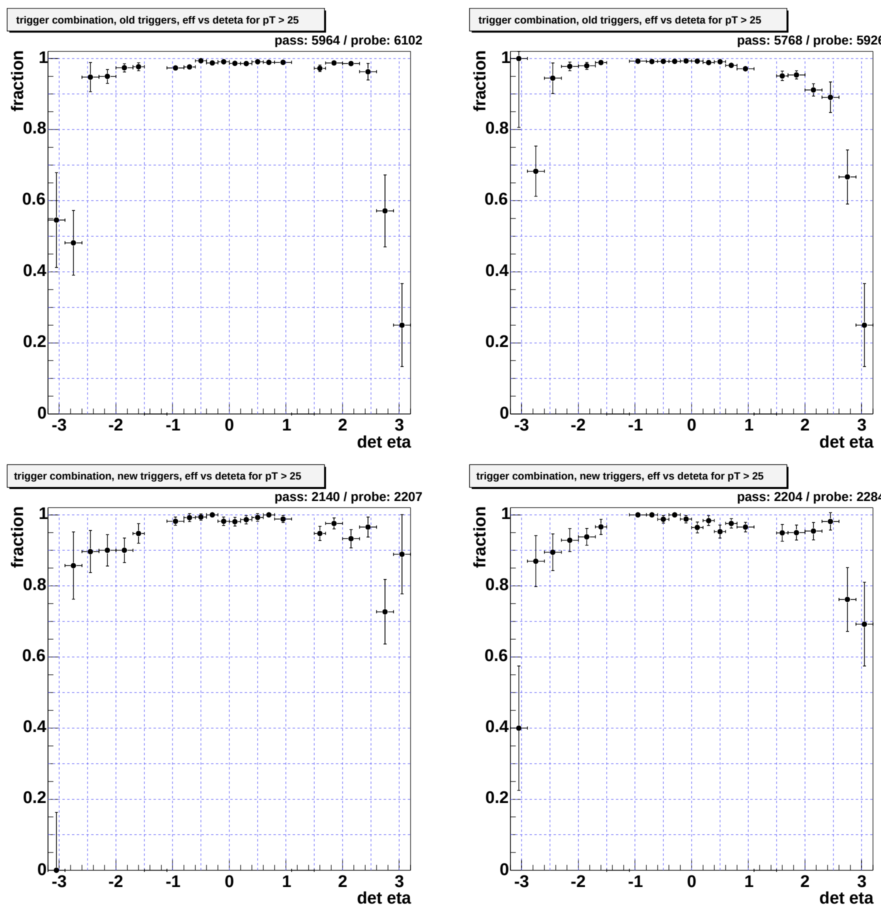

Figure 45: Electron trigger efficiency with respect to detector eta for runs $\leq$ 178721 (top) , runs $\geq$ 178722 (bottom), primary vertex z < 0 (left) and primary vertex z > 0 (right).

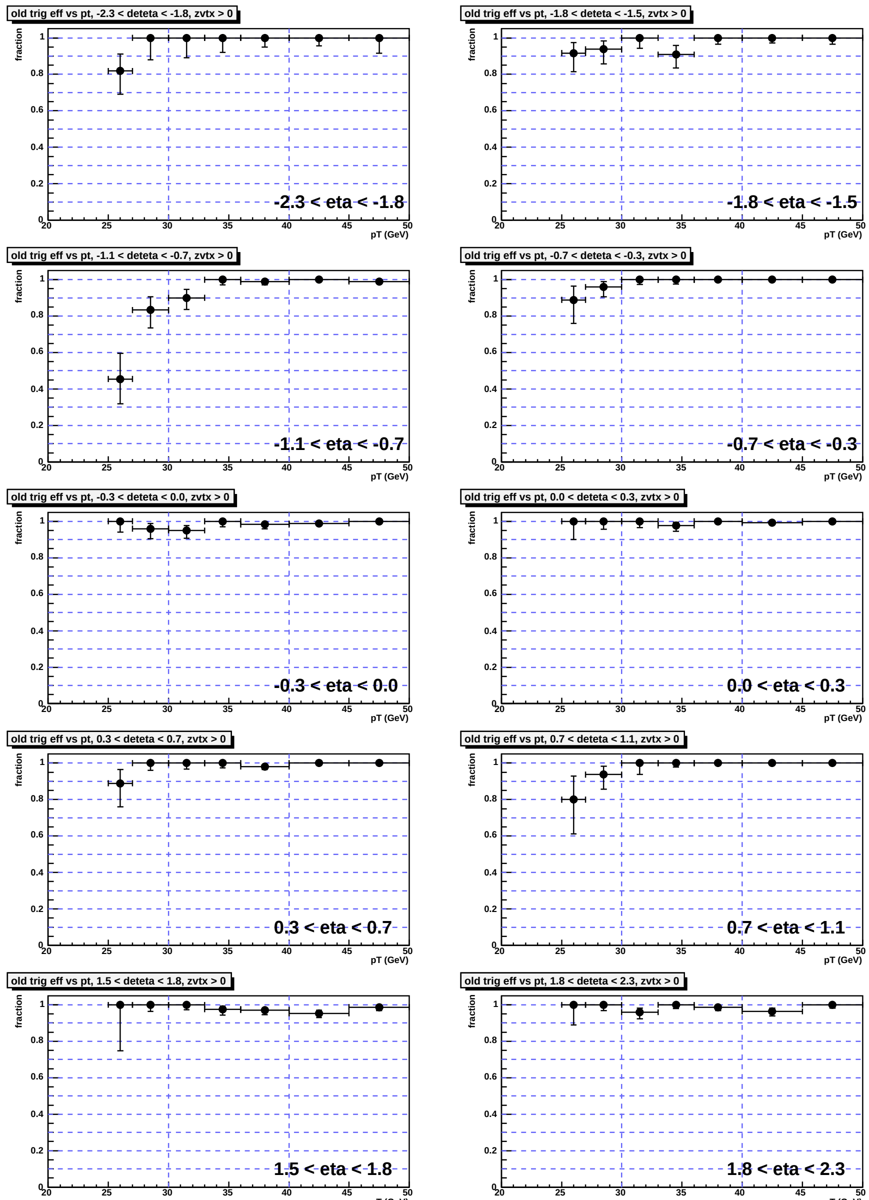

Figure 46: Summary of electron trigger efficiency in bins used in PMCS for runs ≤ 178721 and primary vertex z < 0. Plots are shown as a function of p_T (GeV) with η_{det} range displayed on each plot.

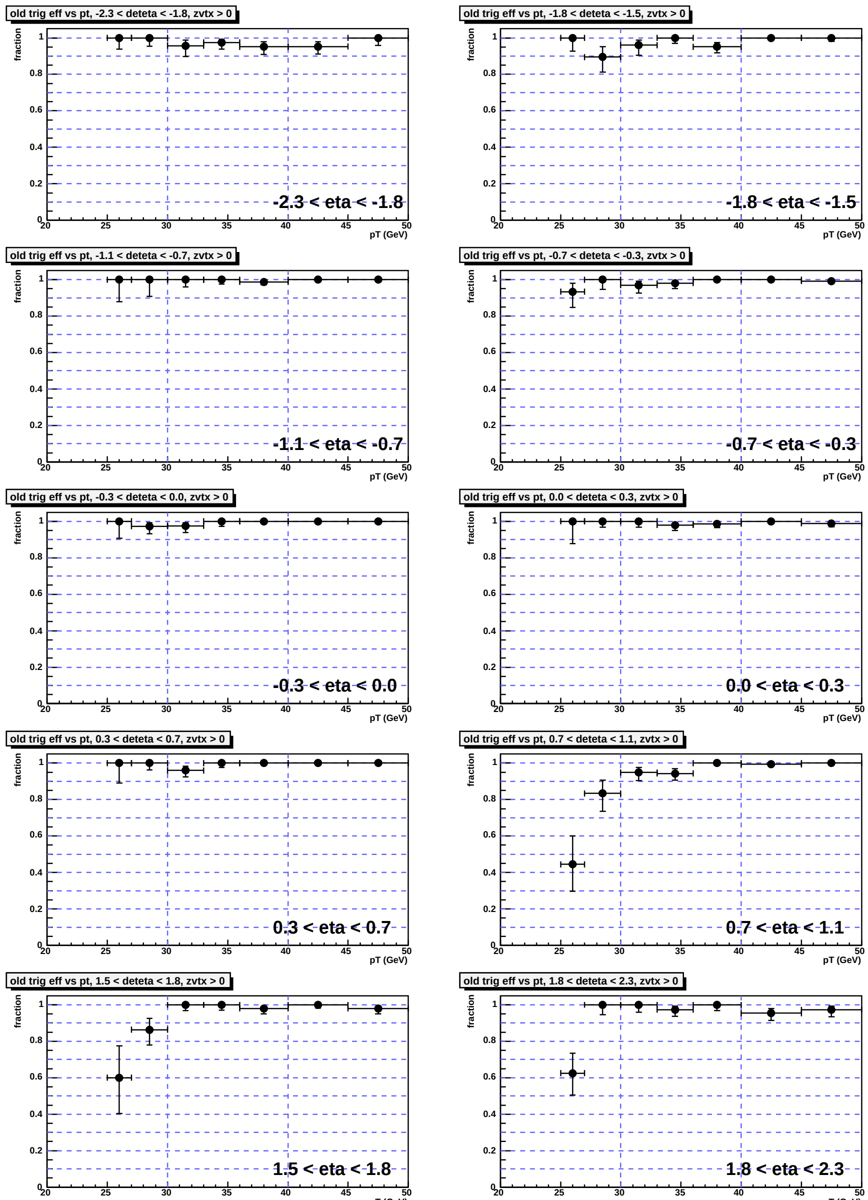

Figure 47: Summary of electron trigger efficiency in bins used in PMCS for runs $\leq$ 178721 and primary vertex z > 0. Plots are shown as a function of p_T (GeV) with η_{det} range displayed on each plot.

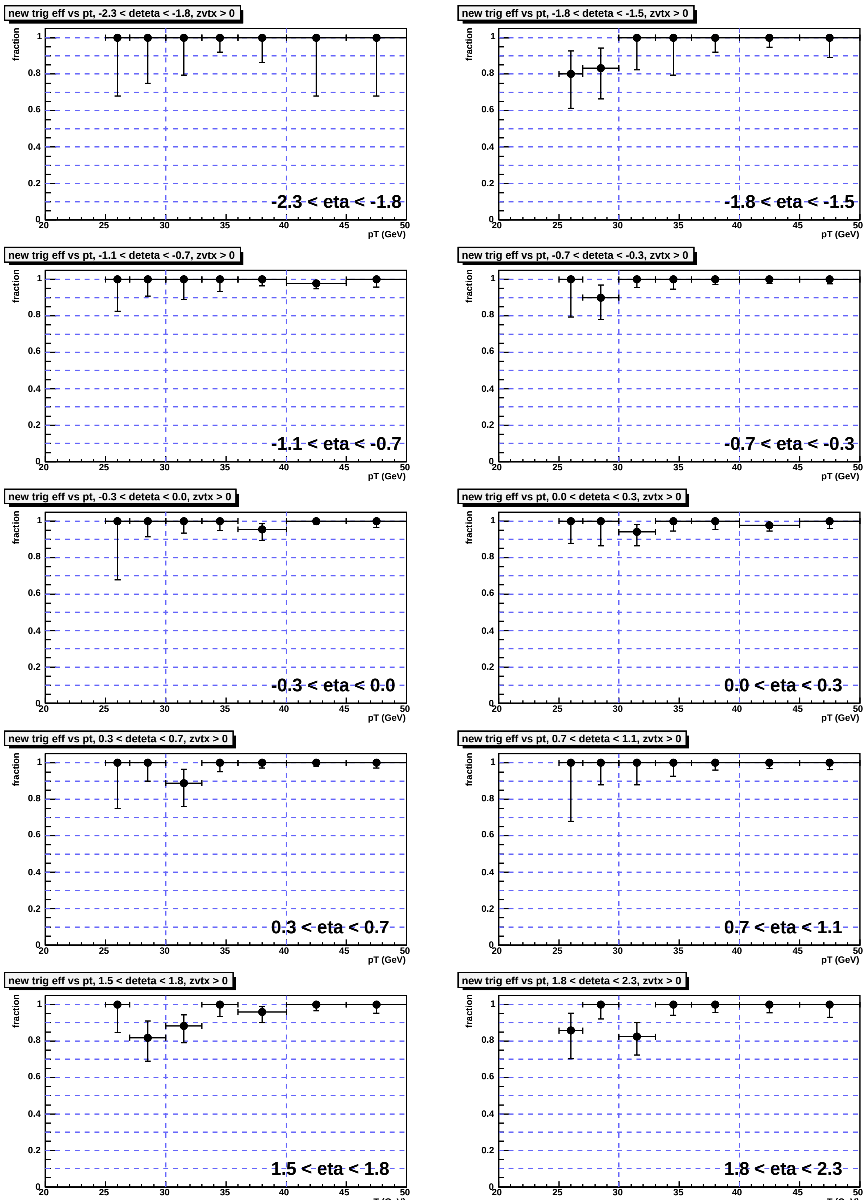

Figure 48: Summary of electron trigger efficiency in bins used in PMCS for runs $\geq$ 178722 and primary vertex z $<$ 0. Plots are shown as a function of p_T (GeV) with η_{det} range displayed on each plot.

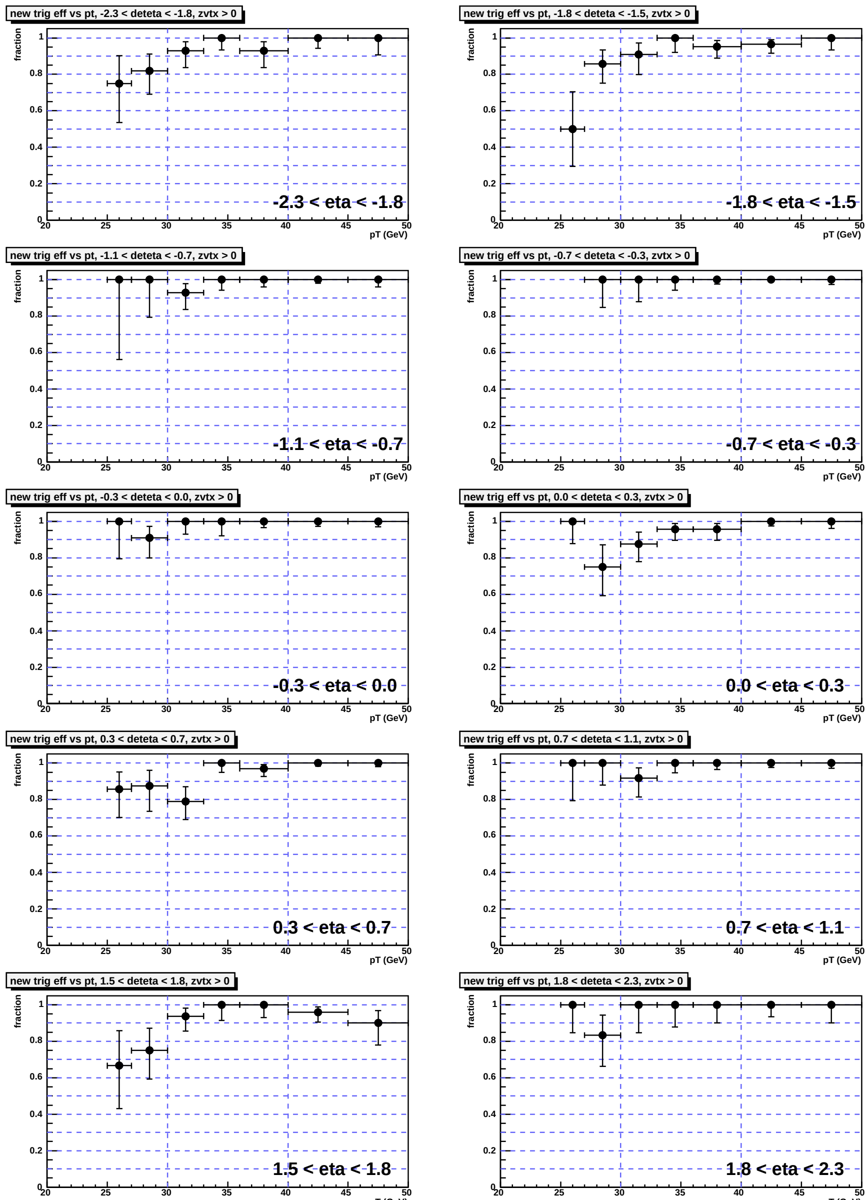

Figure 49: Summary of electron trigger efficiency in bins used in PMCS for runs ≥ 178722 and primary vertex z > 0. Plots are shown as a function of p_T (GeV) with η_{det} range displayed on each plot.

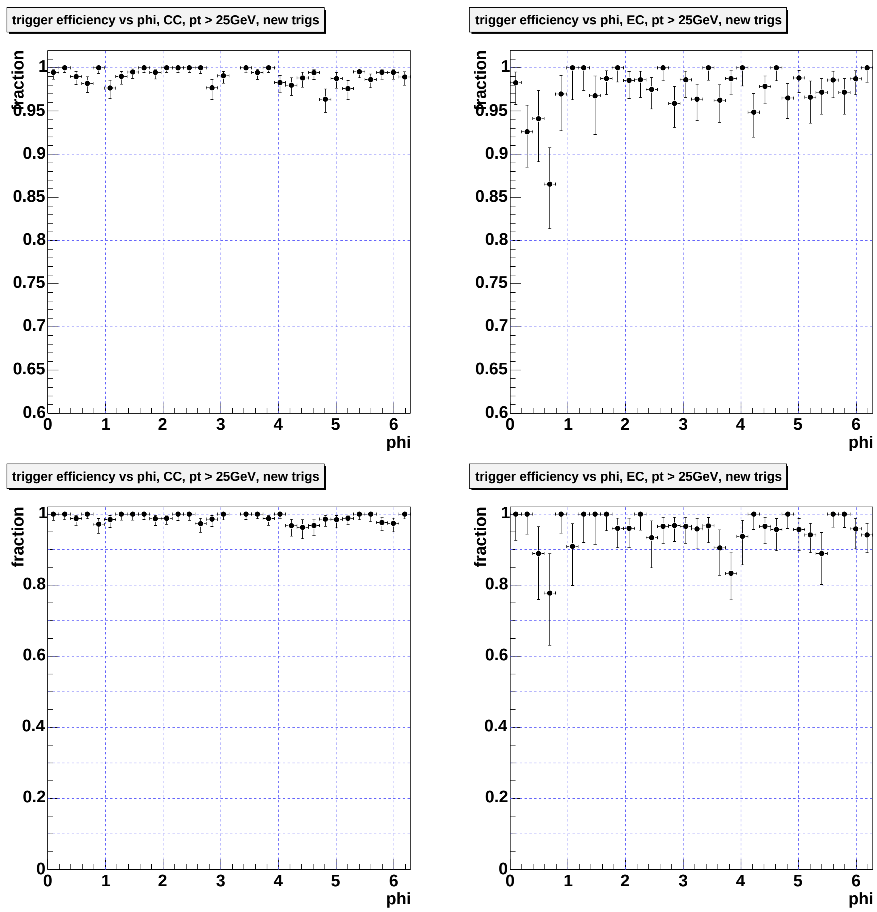

Figure 50: Electron trigger efficiency vs. phi for runs ≤ 178721 (top), runs ≥ 178722 (bottom), for CC (left) and EC (right)

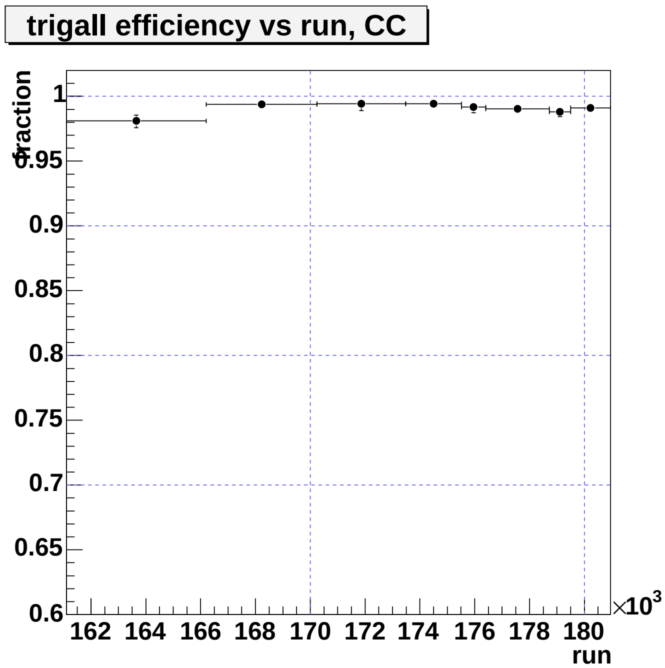

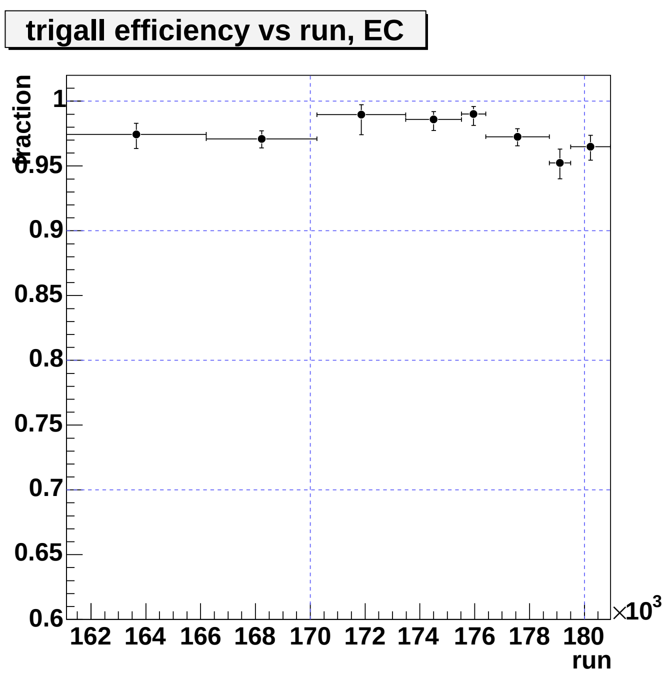

Figure 51: Electron trigger efficiency vs. run number for CC (top) and EC (bottom)

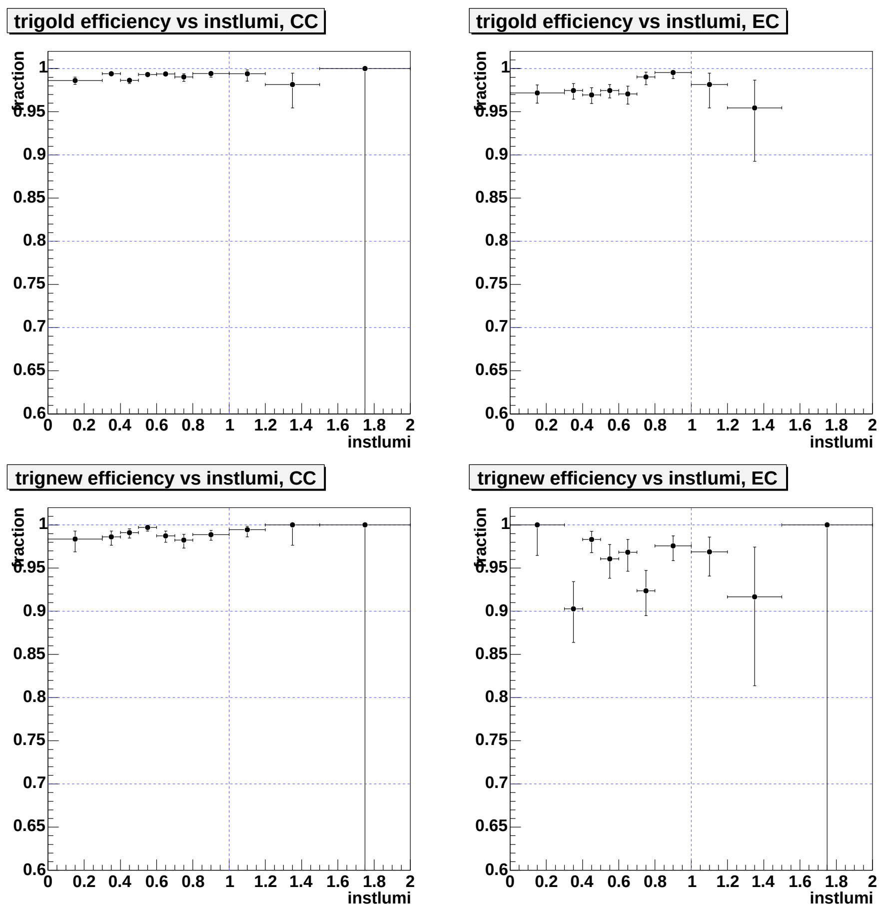

Figure 52: Electron trigger efficiency vs. instantaneous luminosity ($10^{30} cm^{-2} s^{-1}$) for runs $\leq$ 178721 (top), runs $\geq$ 178722 (bottom), for CC (left) and EC (right)

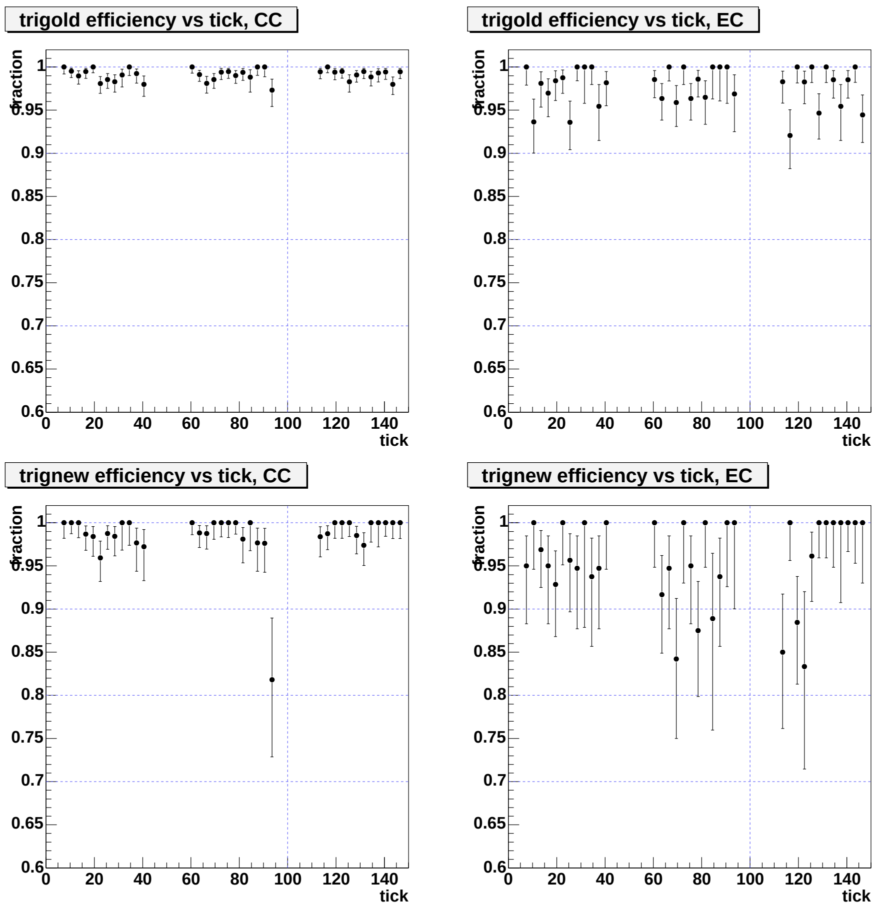

Figure 53: Electron trigger efficiency vs. tick number for runs ≤ 178721 (top), runs ≥ 178722 (bottom), for CC (left) and EC (right). This plot shows the 153 ticks, each representing 132 ns or 39.6 m, within the Tevatron circumference. This is divided into 3 groups of 12 bunches, with each bunch in a group separated by 3 ticks.

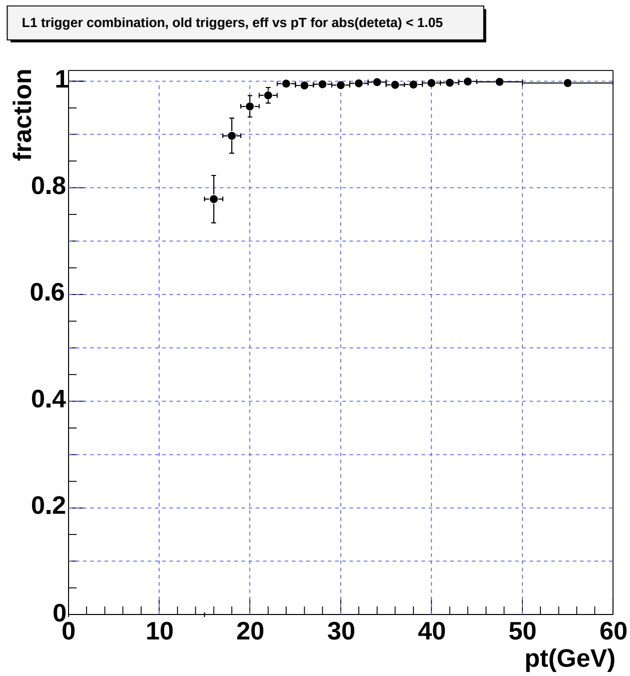

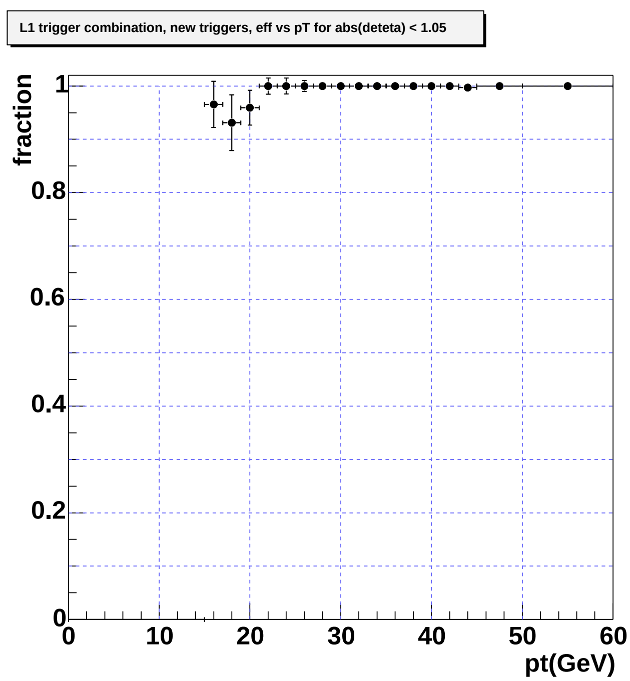

Figure 54: Combined L1 electron trigger efficiency with respect to electron p_T for runs $\leq$ 178721 (top) and runs $\geq$ 178722 (bottom).

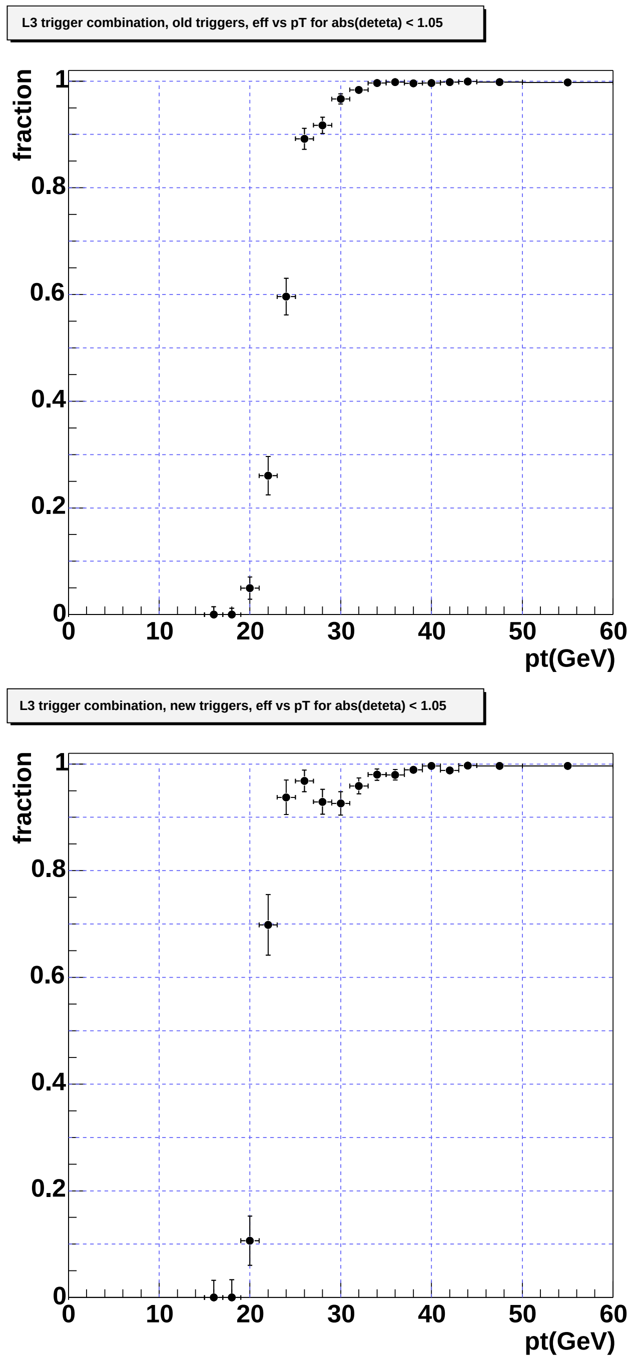

Figure 55: Combined L3 electron trigger efficiency with respect to electron p_T for runs $\leq$ 178721 (top) and runs $\geq$ 178722 (bottom).

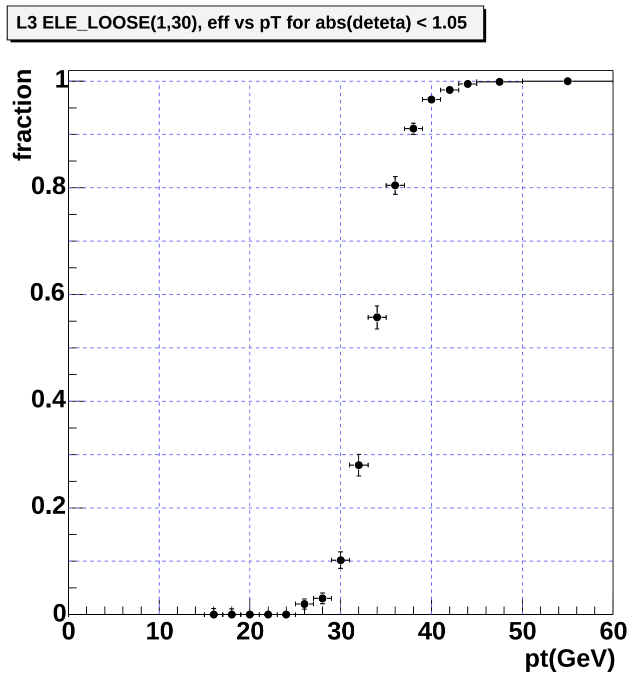

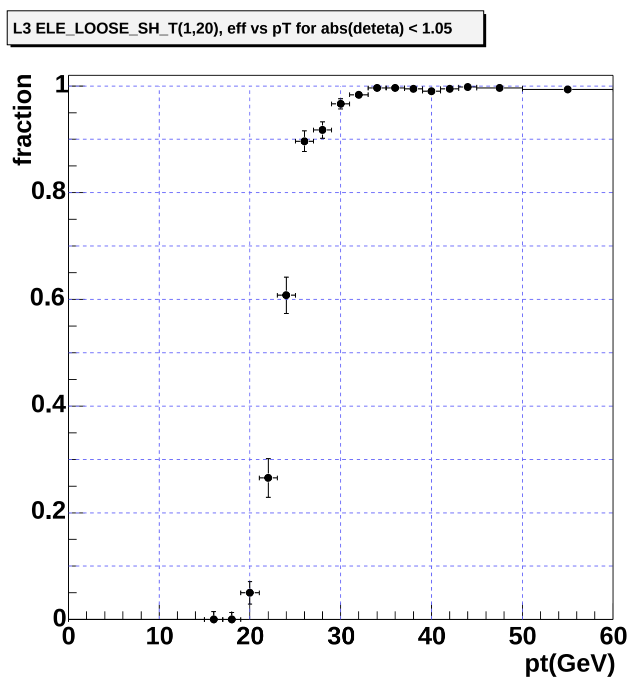

Figure 56: Electron trigger efficiency for L3 triggers used in runs $\leq$ 178721 with respect to electron p_T in the CC region. ELE_LOOSE(1,30) (top) and ELE_LOOSE_SH_T(1,20) (bottom)

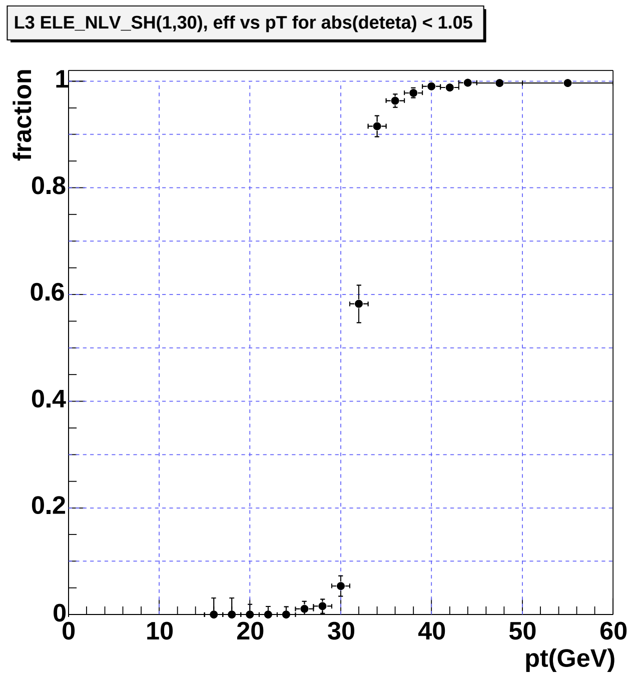

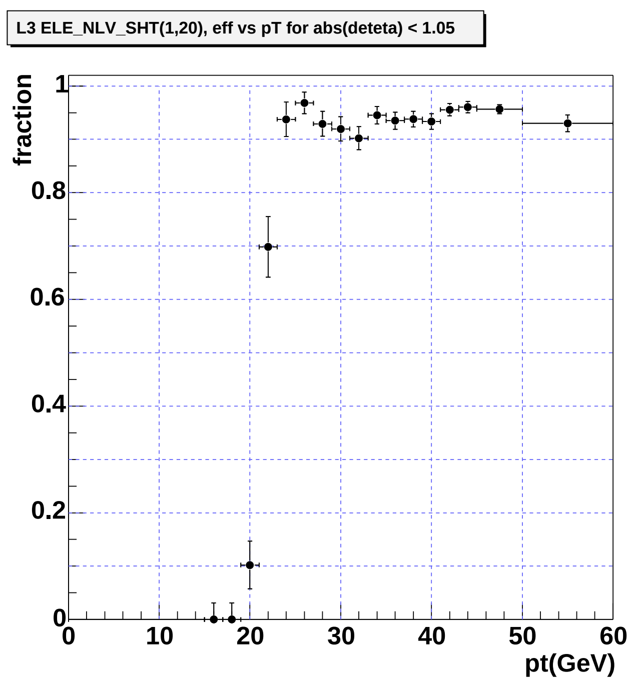

Figure 57: Electron trigger efficiency for L3 triggers used in runs $\geq$ 178722 with respect to electron p_T in the CC region. ELE_NLV_SH(1,30) (top) and ELE_NLV_SHT(1,20) (bottom). The plot for ELE_NLV_SHT suggests a higher efficiency at 25 GeV than just above.

4.4 Electron Likelihood Efficiency

The electron likelihood was developed to maximize discrimination between signal and background. Histograms of seven variables are input for a signal and background sample obtained from data. These variables are:

- EM fraction
- H-Matrix(8)
- Calorimeter E_T / Track P_T
- Track DCA
- Track spatial χ^2 probability
- Number of tracks in an 0.05 cone around (and including) the candidate track
- Total P_T of tracks in an 0.4 cone around the candidate track, but excluding the candidate track

See [3] for detailed information on the likelihood.

The tag-probe method is used with the probe electron required to pass preselection, track match and trigger cuts to be considered. The likelihood efficiency is defined as the fraction of events with the probe electron passing the likelihood cut over the total number of probes. The likelihood efficiencies are shown as a function of detector and physics eta in figure 59, electron E_T in figure 60, detector phi in figure 61, run in figure 62, instantaneous luminosity in figure 63, tick number in figure 64 and phimod in figure 65. The efficiency is fairly steady for both CC and EC except perhaps when the primary vertex is far from zero. The average efficiency is $(90.7 \pm 0.3)\%$ for CC and $(87.0 \pm 0.6)\%$ for EC.

For the PMCS simulation and W candidate background subtraction, likelihood efficiency uses the same η_{det} and primary vertex z position binning as track matching efficiency. See figure 66 for plots vs η_{det} for all z vertex bins.

Background is negligible in the tag-probe sample used in finding electron likelihood efficiency since the probe must already satisfy all other cuts. Figure 58 verifies the amount of background present is too small to detect. However, a conservative systematic error of 0.5% is assigned to the efficiency due to variations in the central E_T distribution and at the phi module boundaries.

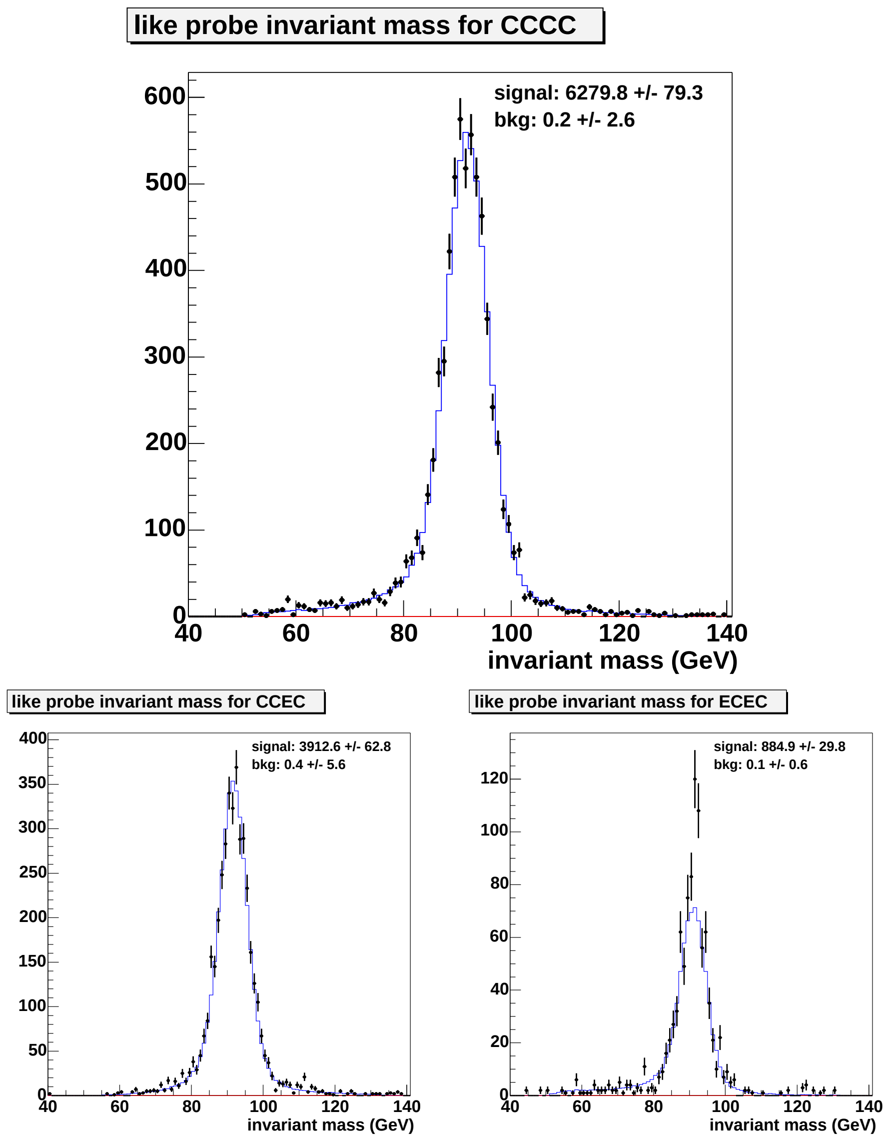

Figure 58: Invariant mass distribution of probes before likelihood requirement for CC-CC (top), CC-EC (left) and EC-EC (right).

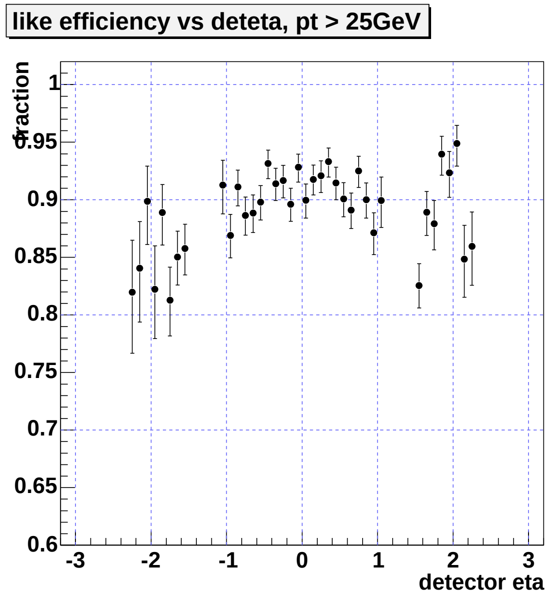

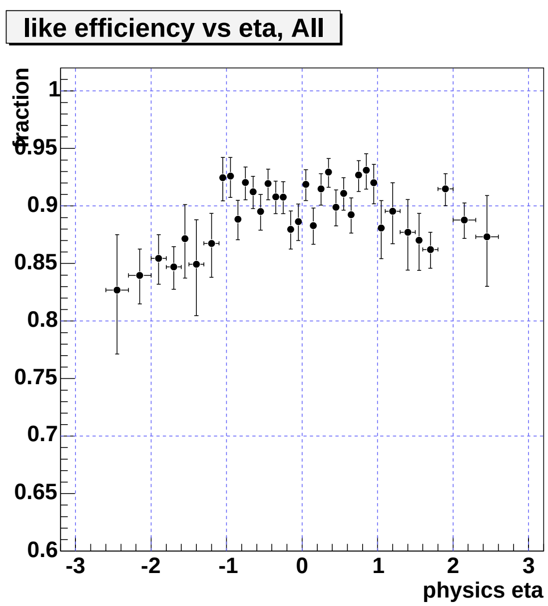

Figure 59: Likelihood efficiency vs. η_{det} (top) and η_{phys} (bottom).

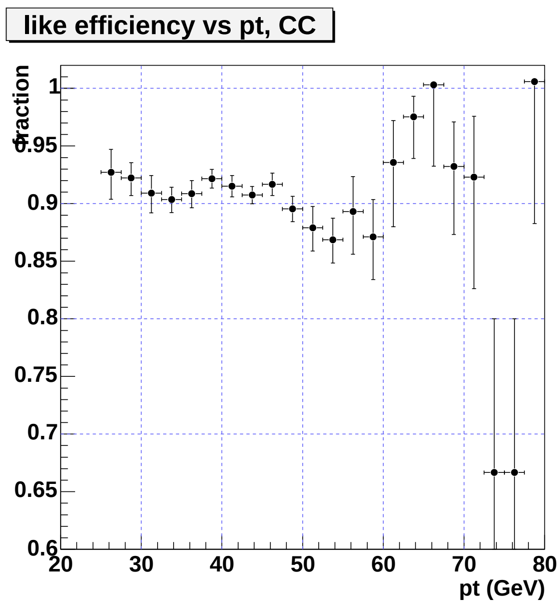

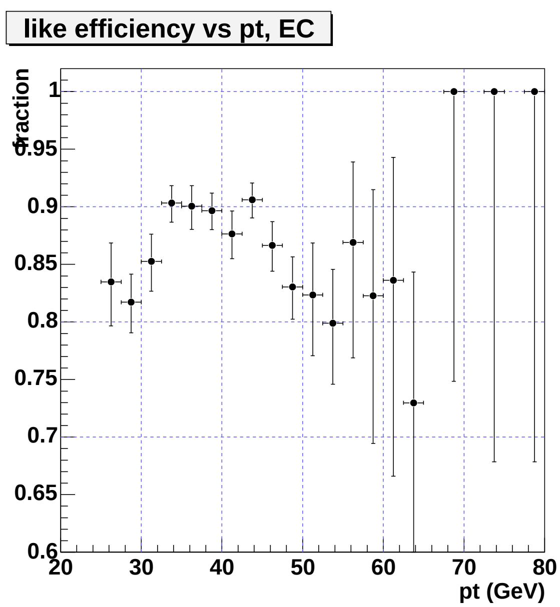

Figure 60: Likelihood efficiency vs. E_T for CC (top) and EC (bottom).

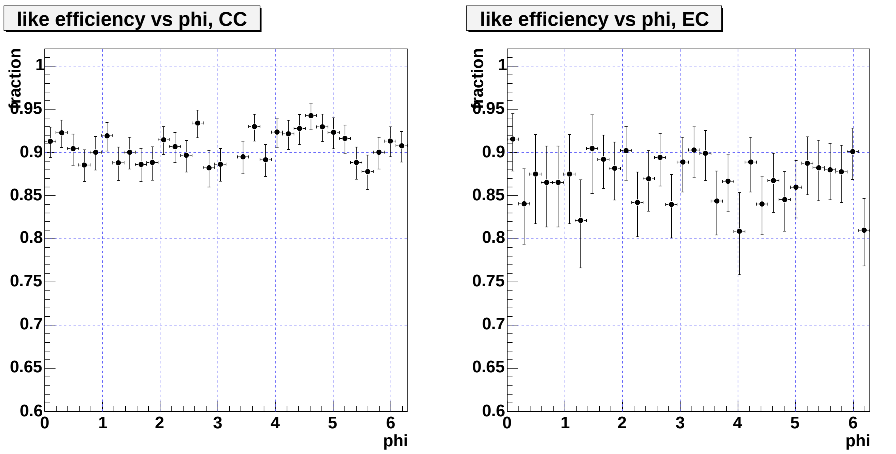

Figure 61: Likelihood efficiency vs. ϕ for CC (left) and EC (right).

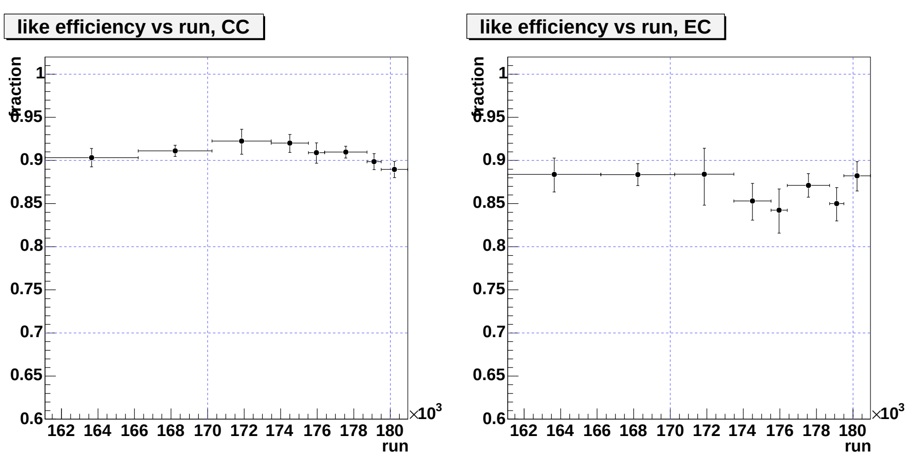

Figure 62: Likelihood efficiency vs. run number for CC (left) and EC (right).

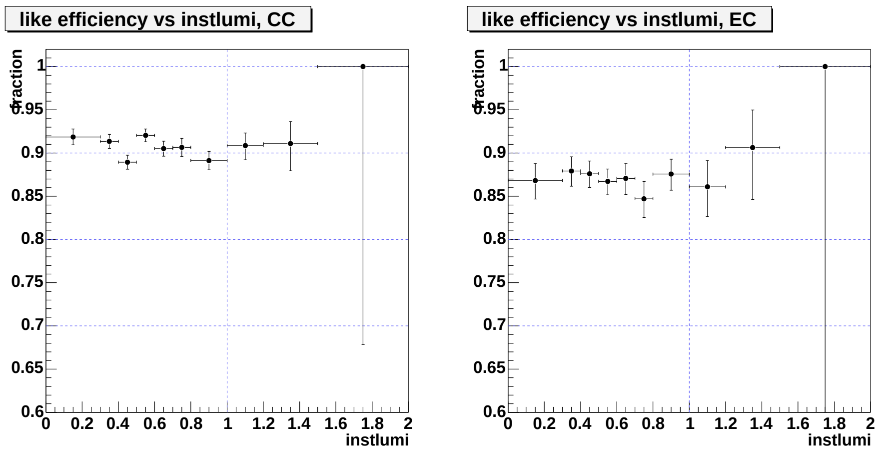

Figure 63: Likelihood efficiency vs. instantaneous luminosity ($10^{30} cm^{-2} s^{-1}$) for CC (left) and EC (right).

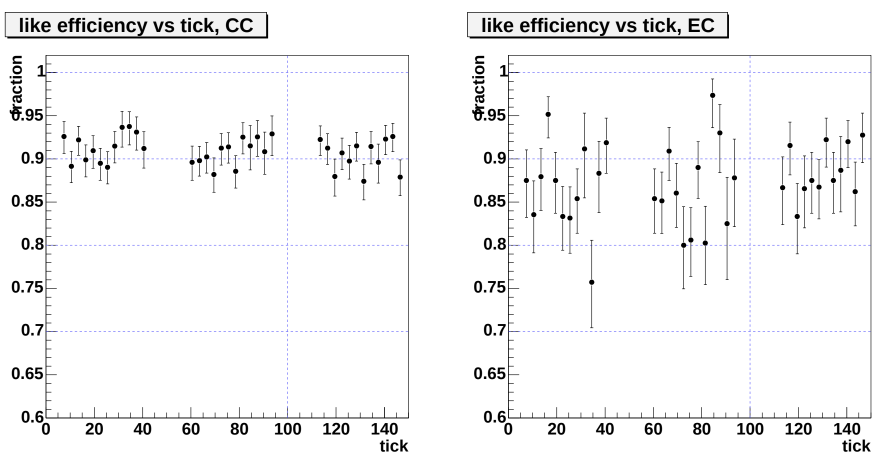

Figure 64: Likelihood efficiency vs. tick number for CC (left) and EC (right). This plot shows the 153 ticks, each representing 132 ns or 39.6 m, within the Tevatron circumference. This is divided into 3 groups of 12 bunches, with each bunch in a group separated by 3 ticks.

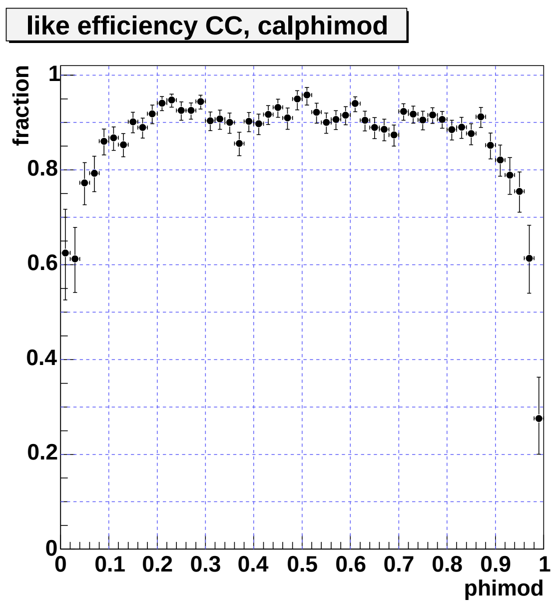

Figure 65: Likelihood efficiency vs phimod for CC using EM ϕ_{det}.

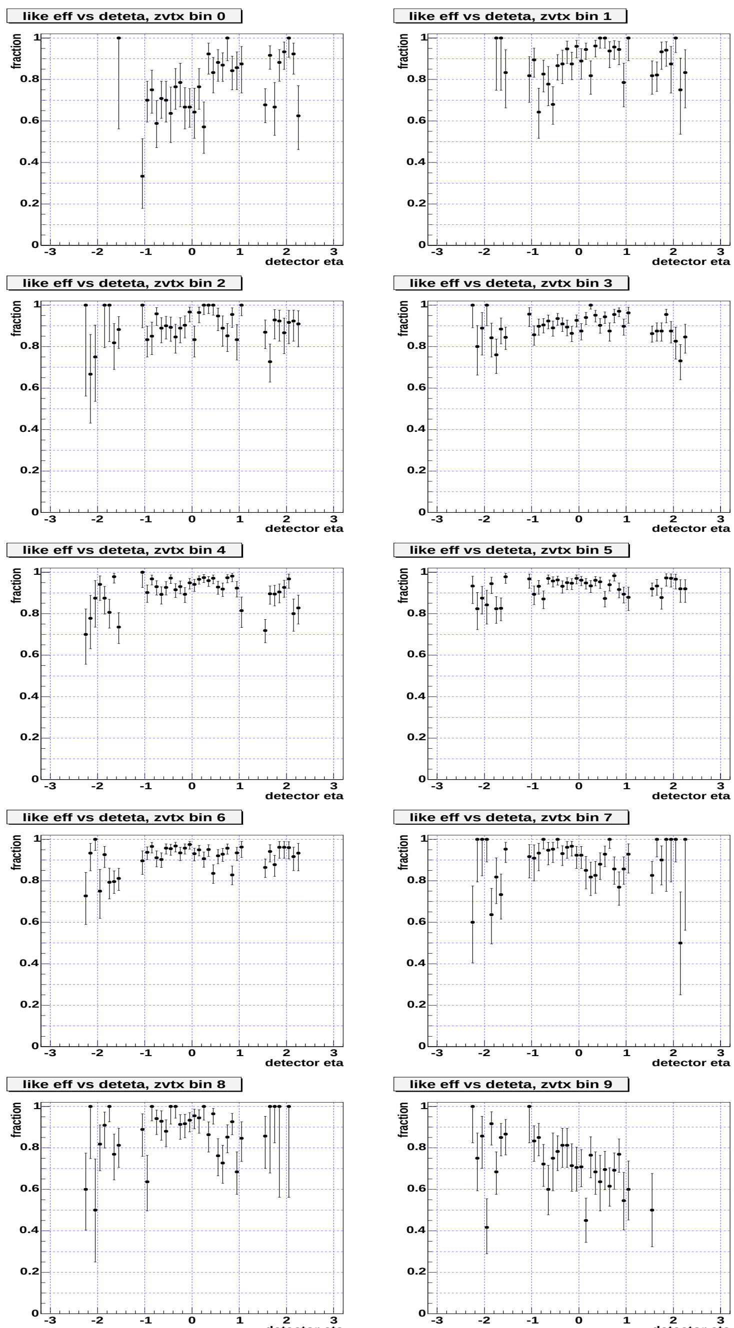

Figure 66: Likelihood efficiency vs η_{det} using primary vertex z bins as used for W background subtraction and input into PMCS. Z vertex bins are, going left to right from top to bottom: $<$ -39, -39 to -30, -30 to -23, -23 to -10, -10 to 0, 0 to 10, 10 to 23, 23 to 30, 30 to 39, and $>$ 39 cm.

5 Backgrounds

Events other than $Z \to ee$ or $W \to e\nu$ can sometimes pass the Z or W selection criteria and contaminate the data samples. In this section, we study the background for $Z \to ee$ and $W \to e\nu$ events.

5.1 QCD Background in the $Z \to ee$ Sample

Subtraction of QCD background from the Z event sample is needed for various efficiency measurements and to extract the number of Z events. We briefly describe the method of background subtraction here.

5.1.1 QCD Background Shape

The invariant mass distribution of the QCD background is determined directly from data. QCD background candidates are required to fulfill the following criteria:

- All criteria that are applied to loose electron candidates as described in section 3.2
- Electron Likelihood < 0.1
- Two of these objects per event.

In this way we select two jets with high electromagnetic energy content in the shower. Inversion of the electron likelihood cut is chosen as it is expected that this quantity has little impact on the kinematic properties of the background selection. The invariant mass distribution is determined separately for CC-CC and CC-EC events.
To subtract background from other distributions, QCD background from the di-EM mass distribution within 70 to 110 GeV is also plotted for all variables of interest. This background, scaled by the same amount as in the invariant mass fit, is subtracted from the sample. One additional requirement that must be considered is the dependence of track matching on the variable. Track matching has large dependencies on pseudorapidity and primary vertex, especially in the end caps. Separate background distributions are made for Z candidates where at least one track is required and for tag-probe events where the event is plotted once for each electron with a track.

5.1.2 QCD Background Subtraction for Z Events

The invariant mass distribution of the signal is taken from PMCS: $p\bar{p} \to Z/\gamma^* + X \to e^+e^- + X$ decays have been simulated with the PMCS Monte Carlo that has been tuned to match the data (see section 6). The energy scale has been tuned separately for the CC and the EC regions. Separate Monte Carlo signal shapes for Z events with electrons in the CC-CC and CC-EC regions have been used for the background subtraction.

The linear combination of the invariant mass distributions from background and signal Monte Carlo is fitted to the Z candidate data with the scale factors as free parameters to the fit. A χ^2 fit in the mass region 40 GeV to 140 GeV is used. These fits are shown in figures 84 and 85. This procedure is also carried out for EC-EC however uncertainty is large due to poor data-PMCS agreement in this region. See table 4 for statistics after background subtraction.

A systematic is estimated based on χ^2 fit errors, variations with alternate background choices and comparisons to matrix method background subtraction.

The uncertainty from the χ^2 fit is $\sqrt{\delta^2_{\chi^2} - \delta^2_{stat}}$ where δ_{χ^2} is the total uncertainty of the fit and δ_{stat} is the uncertainty due to limited z stats. This is found to be 0.35% for CC-CC and 0.46% for CC-EC or 0.39% combined.

To study the effect on the cross sections due to a systematic uncertainty in the background shape, several alternate background shapes were defined using different (and reasonable) inverse HMatrix cuts:

- likelihood < 0.1 (nominal)
- HM7 > 20 (CC) or HM8 > 25 (EC)
- HM8 > 35
- HM8 > 25
- $25 <$ HM7/8 < 60
- HM7/8 > 50

where HM7/8 means that the HM8 value was used in the EC region and twice the HM7 value was used in the CC region. The track-match efficiency, number of Z events, number of W events and the resulting cross sections were redetermined for each background choice. As a conservative estimate, the largest deviation from the normal cross section value is used. This is found to be 0.24% for CC-CC and 0.08% for CC-EC or -0.15% combined.

For the last check, a matrix method similiar to that used for W background subtraction is adapted for Z events. See 8.2 for a description. For this, electrons with a track in di-EM events are used as probes and the matrix method is applied in a similiar way as for W events as described in section 5.3.2. Compared to the nominal method of fitting to a peak and background shape, the number of background subtracted events predicted using the matrix method differs by 0.62% for CC-CC and -0.08% for CC-EC or 0.40% combined.

Combining these resulting in quadrature yields a background systematic of 0.75% for CC-CC, 0.47% CC-EC and 0.58% combined.

	signal	background percentage
CC-CC	5068	$2.0 \pm 0.7\%$
CC-EC	2732	$0.8 \pm 0.5\%$

Table 4: Z event signal and background statistics

5.2 Other Backgrounds in the $Z \to ee$ Sample

In addition to QCD background, two other backgrounds for $Z \to ee$ events were considered: physics background from Drell-Yan and $Z \to \tau\tau$ events.

5.2.1 Backgrounds from Drell-Yan events

The production of dielectron pairs is properly described by the Z boson, the off-shell photon propagator, and the interference between the two. To match with data, acceptance is found using full Z/γ^* monte carlo. The physical Z/γ^* cross section is then proportional to the number of Z candidates, after QCD background subtraction, over acceptance.

$$\sigma(Z/\gamma^*) \propto N_Z/A_{Z/\gamma^*} \tag{11}$$

In order to convert to a pure Z cross section, a Drell-Yan correction factor is introduced relating the Z/γ^* cross section to that expected purely from Z boson production:

$$\sigma(Z) = R_\sigma \times \sigma(Z/\gamma^*) \tag{12}$$

where $R_\sigma = 0.9547$ is the ratio of the pure Z to Z/γ^* cross sections. This ratio is obtained using 20 million pure Z, 2 million Z/γ^* interference, and 2 million pure γ^* events generated using Resbos [6] with the CTEQ6.1M NLO PDF sets and an invariant mass cut of 50 to 130 GeV to match the mass cut used in the acceptance calculation. A systematic error of 0.30% on the cross sections is estimated using Pythia and the CTEQ6.1M error PDF sets. This is discussed in Section 6.6.

5.2.2 Backgrounds from $Z \to \tau\tau$ events

The background from $Z \to \tau\tau$ processes, where both taus decay electronically is considered. However, electrons from τ decays have a softer E_T spectrum and a small branching ratio $B(\tau \to e\nu\nu)^2$, making this background negligible.

5.3 QCD Background in the $W \rightarrow e\nu$ Sample

5.3.1 Electron Likelihood Fake Rate

The probability for a fake electron to pass the electron likelihood cut, described in section 4.4, is determined from jet-jet events where one jet has been misidentified as an electron. The EM cluster has to pass all cuts except electron likelihood and be back-to-back with a jet in ϕ with a deviation of $\Delta\phi < 0.5$. Jet candidates are identified using the 0.7 cone algorithm. The fake rate is then the fraction of those EM objects that are found to pass the likelihood cut.

The p_T ratio of the leading jet and the EM object needs to be smaller than 2.0. The jet opposite to the electron candidate is required to pass the following criteria which are largely determined by the Jet-ID group:

- $N90 > 1$
- $0.05 <$ EM-fraction < 0.7
- CHF < 0.25
- Jet7_hotf $<= 5$
- F90 < 0.65
- $p_T > 20$ GeV
- at least 5 tracks within $\Delta R < 0.5$

The requirements on the EM fraction of the jet and the F90 variable are more stringent than the general recommendation. This reduces the background contamination in the jet sample. It also decreases the efficiency of the jet selection which is of no concern for this analysis. The electron candidate in the event must pass exactly the same selection criteria as the probe in the electron likelihood efficiency measurement. Missing E_T in the event must be smaller than 10 GeV in order to remove W + jet events from the sample.

The fake rate values used to determine the background in the W sample are shown in Figure 67. Binning is chosen to match that of electron likelihood efficiency. Fake rate is also determined separately versus E_T and MET as shown in figures 68 and 69. Fake rate with MET $<$ 10 GeV varies between 15 and 20% for both of these distributions in the central region and has an average value of (18.0 ± 0.2)% and for the end caps it is flat vs. MET and for E_T varies between 5 and 12% with an average of (10.61 ± 0.15)%. For high values of MET the data sample is contaminated by W + jet events causing the apparent increase in fake probability. We assume that background to the fake rate coming from physics processes other than QCD is negligible. In a previous analysis [5], Monte Carlo simulations for the central detector region estimated an absolute effect of only 0.05%.

Systematic error arising from the fake rate is found to be negligible. Variations found in the central region for the E_T and missing E_T distributions suggest a 25% uncertainty to be a rather conservative estimate. However, results are stable under even much larger variations. Setting the fake rate to zero results in a change of -0.03% in the cross section and increasing it by 50% results in a 0.13% change. This lack of sensitivity to variation in fake rate is due to the already high purity of the (loose) W candidate sample along with the relatively high efficiency of the likelihood cut.

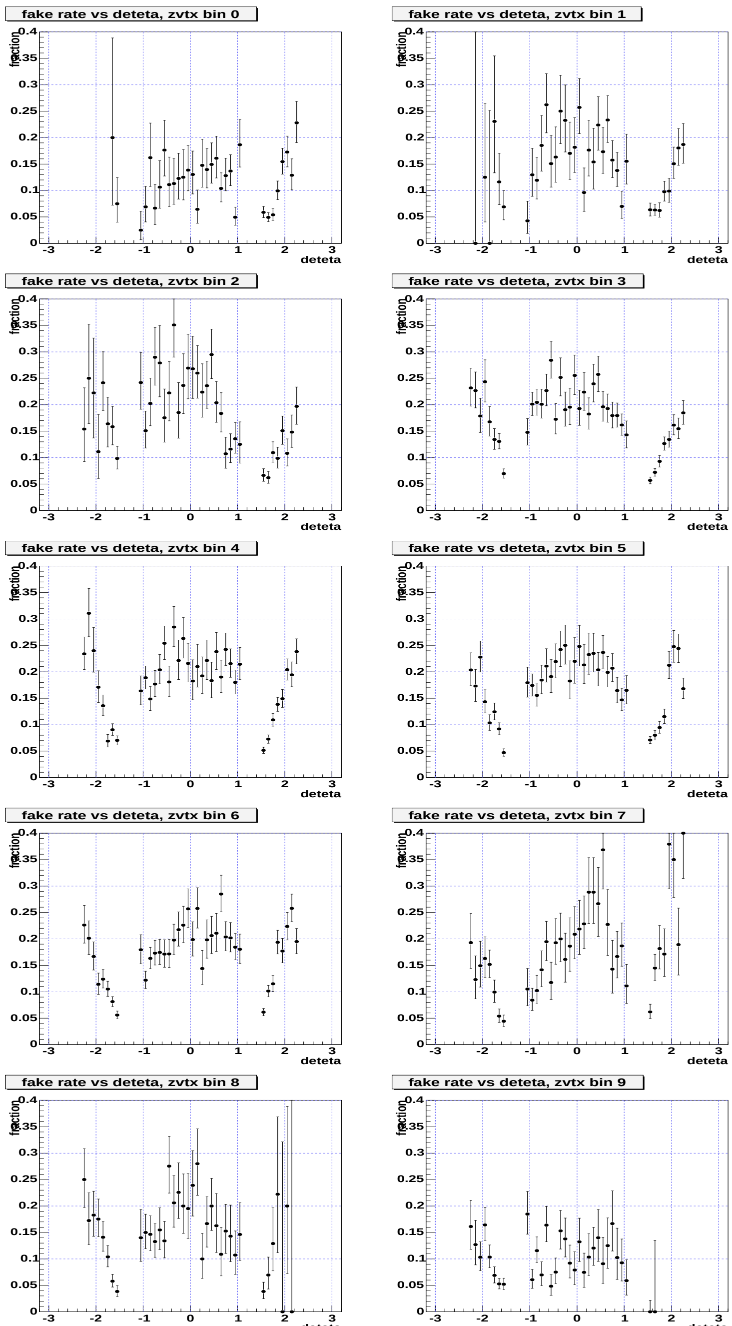

Figure 67: Electron likelihood fake rate as a function of η_{det} in primary vertex z bins as used for W background subtraction. Z vertex bins are, going left to right from top to bottom: $<$ -39, -39 to -30, -30 to -23, -23 to -10, -10 to 0, 0 to 10, 10 to 23, 23 to 30, 30 to 39, and $>$ 39 cm.

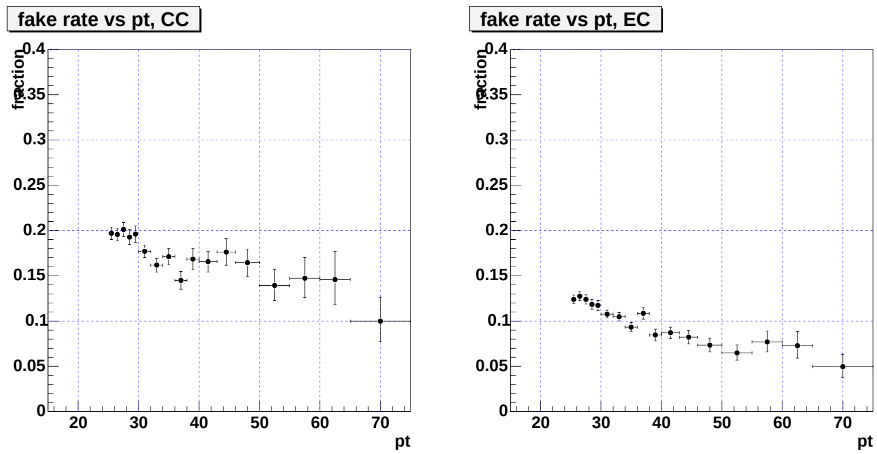

Figure 68: electron likelihood fake rate as a function of the electron E_T for CC (left) and EC (right)

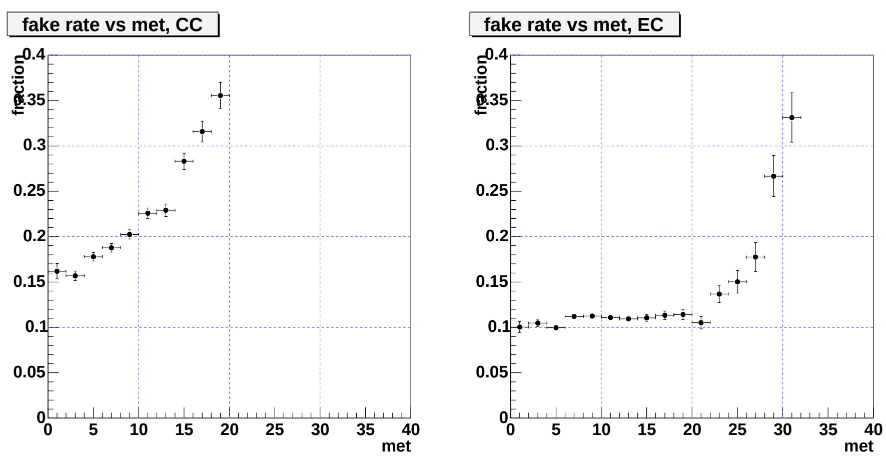

Figure 69: electron likelihood fake rate as a function of the missing E_T for CC (left) and EC (right)

5.3.2 Matrix method background subtraction

In order to subtract QCD background from W candidates we solve two linear equations using the number of W Candidates with and without the electron likelihood requirement as well as the likelihood efficiency and fake rate. The number of W bosons produced is extracted from the following equations.

$$N_{WCandidates} = N_W + N_{QCD}$$

$$N^{likelihood}_{WCandidates} = \epsilon_{likelihood} N_W + f_{QCD} N_{QCD}$$

Yielding

$$N_W = \frac{N^{likelihood}_{WCandidates} - f_{QCD} N_{WCandidates}}{\epsilon_{likelihood} - f_{QCD}}$$

where N_W is the true number of W bosons, $N_{WCandidates}$ is the number of W candidate events, $N^{likelihood}_{WCandidates}$ is the number of W candidate events passing the likelihood cut, f_{QCD} is the electron likelihood fake rate, and $\epsilon_{likelihood}$ is the likelihood efficiency.

The above equations are applied in bins of η_{det} and primary vertex z as shown in figures 66 and 67. The result of the matrix method for all bins is shown in Figure 70. The number of W events is determined to be

$$N_W^{CC} = 96799 \pm 731 \tag{13}$$

The quoted uncertainty includes the statistical uncertainty of the W sample as well as the propagated statistical uncertainties coming from the likelihood efficiency and the fake rate. This indicates a background of $1.0 \pm 0.7\%$ in the W sample.

This method of background subtraction is also used to determine additional properties of the W boson and the electron from W decay. The comparisons to PMCS in figures 93 to 105 are produced in this way.

Crosschecks for the matrix method are carried out using an alternate fake sample and alternate discriminants. This is described in sections 8.3 and 8.4.

5.4 Other Backgrounds in the $W \rightarrow e\nu$ Sample

In addition to QCD, two other backgrounds for $W \rightarrow e\nu$ events were considered: $W \rightarrow \tau\nu$ and $Z \rightarrow ee$.

5.4.1 Backgrounds from $W \rightarrow \tau\nu$ events

Events from $W \rightarrow \tau\nu$ production in which the τ decays to an electron are identical to $W \rightarrow e\nu$ events except that on average the electron E_T is lower. We generate 40 million $W \rightarrow e\nu$ events and 1 million $W \rightarrow \tau\nu$ events, and then apply W selection criteria on both samples. Assuming the cross section times branching ratio for $W \to e\nu$ and $W \to \tau\nu$ are the same, the background fraction from $W \to \tau\nu$ is $(1.80 \pm 0.36)\%$ for the central region using a conservative relative error of 20%.

5.4.2 Backgrounds from $Z \to ee$ events

A $Z \to ee$ can mimic a $W \to e\nu$ event if one electron is lost in a poorly instrumented region of the detector or is misidentified as a jet, and the transverse energy in the event is mismeasured and thus giving rise to a high MET. A sample of 2M $Z/\gamma^* \to ee$ MC events is prepared using PYTHIA, then processed through PMCS. After applying W selection criteria, we have 11574 events with electrons in CC region and 2112 events with electrons in EC region. The background fraction is then the product of the ratio of this acceptance ($A_{Z\to W}$) to the W acceptance A_W and the ratio of Z to W inclusive cross sections times branching ratio:

$$f_Z^W(CC) = \frac{\sigma(p\bar{p}\to Z\to ee)}{\sigma(p\bar{p}\to W\to e\nu)} \bullet \frac{A_{Z\to W}^{CC}}{A_W^{CC}} = \frac{\sigma(p\bar{p}\to Z\to ee)}{\sigma(p\bar{p}\to W\to e\nu)} \bullet \frac{11574/2000000}{A_W^{CC}}$$
$$f_Z^W(EC) = \frac{\sigma(p\bar{p}\to Z\to ee)}{\sigma(p\bar{p}\to W\to e\nu)} \bullet \frac{A_{Z\to W}^{EC}}{A_W^{EC}} = \frac{\sigma(p\bar{p}\to Z\to ee)}{\sigma(p\bar{p}\to W\to e\nu)} \bullet \frac{2112/2000000}{A_W^{EC}}$$

The ratio of production cross sections is taken from the theoretical calculations, we have $f_Z^W(CC) = (0.26 \pm 0.05)\%$ using a conservative relative error of 20%.

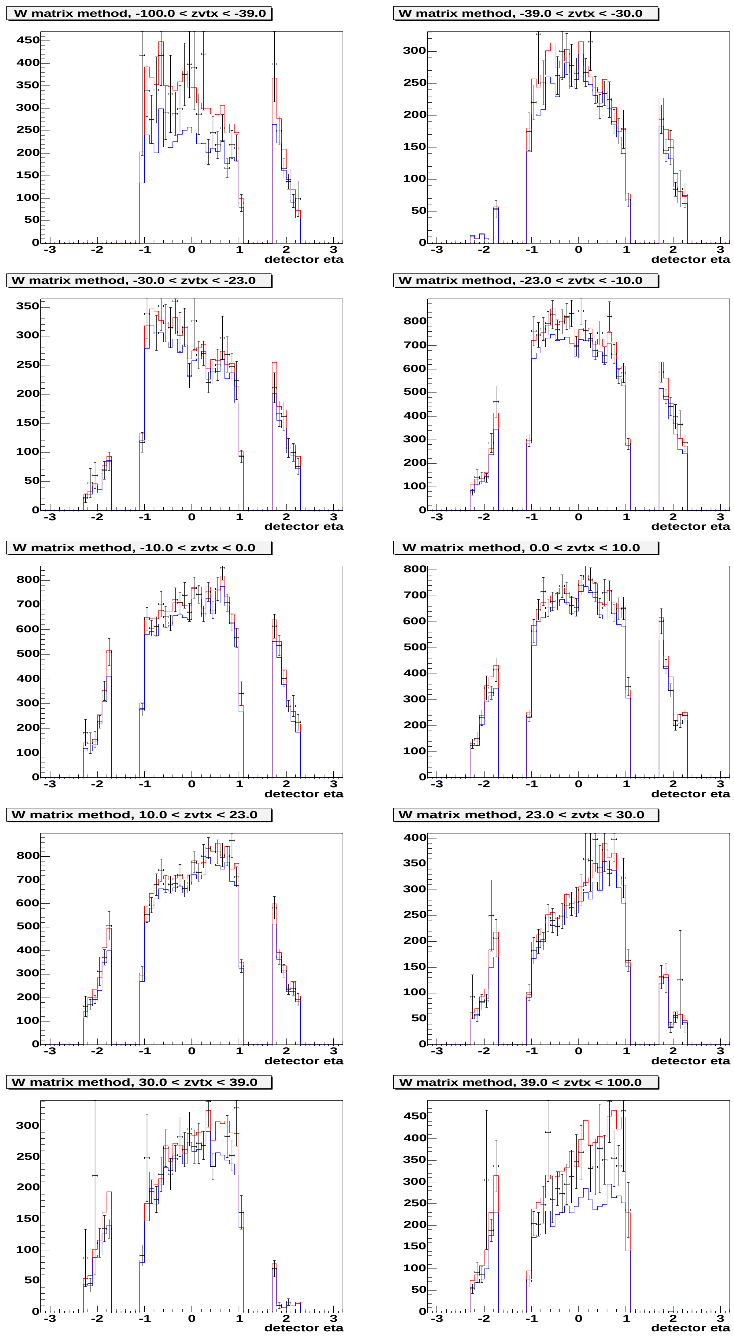

Figure 70: Background subtraction for W candidates as a function of η_{det} in bins of primary vertex z. Z vertex bins are, going left to right from top to bottom: $<$ -39, -39 to -30, -30 to -23, -23 to -10, -10 to 0, 0 to 10, 10 to 23, 23 to 30, 30 to 39, and $>$ 39 cm. The measured input variables are (loose) W candidates without the likelihood cut (the red histograms) and tight W candidates with the likelihood cut (the blue histograms). The true number of W events is shown at each bin with error resulting from event statistics and the measured likelihood efficiency and fake rate. Background from τ decays is treated separately.

6 Monte Carlo Simulation

A Monte Carlo Simulation program called PMCS (Parameterized Monte Carlo Simulation) is used to simulate the response of the detector, the effect of the geometric and kinematic cuts, and the effect of the electron selection and trigger efficiencies. Initially, Resbos [6] is used to generate

for $W \to e\nu$:

- 40 million $W^{\pm} \to e\nu$ events

and for $Z/\gamma^{*} \to ee$:

- 20 million $Z^{0} \to ee$ events
- 2 million $\gamma^{*} \to ee$ events
- 2 million Z/γ^{*} interference events.

All Z/γ^{*} events are generated within the mass range 50 to 130 GeV. The sets of events for Z/γ^{*} are weighted to represent equal relative integrated luminosities so that Z/γ^{*} acceptance can be found by running over all three samples at once. Each Resbos generated event has a unique weight which must be taken into account when filling histograms and calculating acceptance. Initial state QED radiation is accounted for in Resbos, while final state radiation is produced by running Photos [11] after Resbos. Both samples use the CTEQ6.1M next-to leading order PDF set. To each sample, PMCS applies the measured detector responses, selection efficiencies, and cuts on an event-by-event basis in order to obtain a single acceptance value for the sample.

6.1 PMCS Input Parameters

The input vertex distribution, detector response (or *smearing*) parameters, and efficiency distributions are described below. The smearing parameters are summarized in Table 6.

6.1.1 Vertex Distribution

The primary vertex distribution is generated as a Gaussian with a width of 28 cm to match the observed distribution. Figures 91 and 104 show the Z vertex distributions for Z and W candidates in the central calorimeter.

6.1.2 Electron Energy Scale

The energy scale and energy offset constants are determined using the maximum likelihood method and checked with the $< M_{ee} >$ method and Kolmogorov-Smirnov Test, these three different methods all give consistent results. Figure 75 shows the a maximum likelihood versus the energy scale and

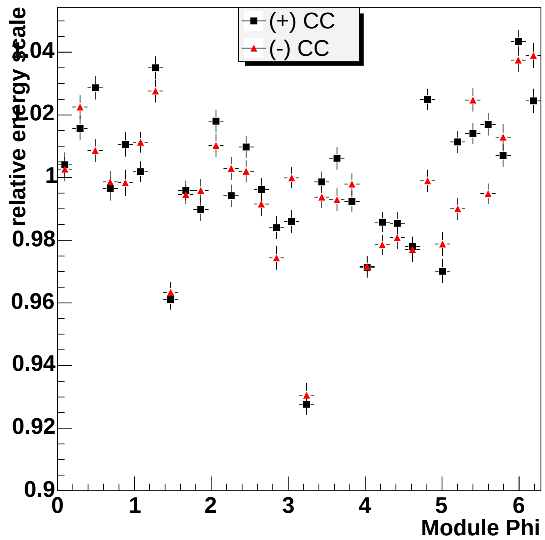

Figure 71: relative electron energy scale as a function of ϕ_{det} and divided into halves in η_{det} for CC

energy offset for CC-CC $Z \rightarrow ee$ candidates. Detailed information can be found in [12].

The electron energy scale is determined to be 1.0054 ± 0.0020 for CC, 0.9990 ± 0.0066 for positive EC and 0.9600 ± 0.0129 for negative EC. The errors are determined from a 0.5 change in the likelihood from the minimum value (see Figure 75). The electron energy scale is calibrated further in the central region. A histogram is made by taking the plot shown in figure 4, of peak calorimeter E_T over track p_T as a function phi module and η_{det} half, and dividing by the CC average peak value. The CC electron energy scale is then multiplied by the value in the corresponding (phi,η_{det}) bin in this histogram which is shown in figure 71.

The energy offset is determined to be 0.191 ± 0.048 GeV for the CC, 0.574 ± 0.300 GeV for positive EC and 0.070 ± 0.499 GeV for negative EC.

6.1.3 Electron Energy Resolution

The electron energy resolution is parameterized as

$$\Delta E/E = \sqrt{C^2 + S^2/E + N^2/E^2}, \tag{14}$$

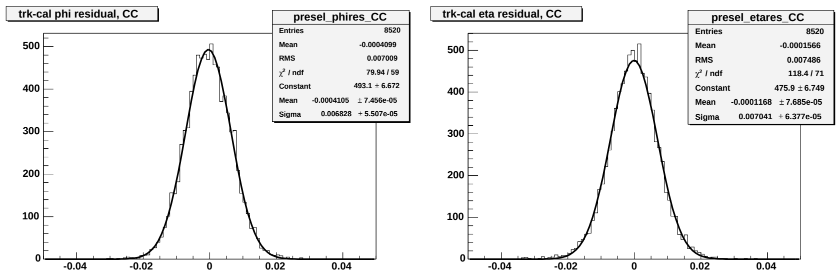

Figure 72: ϕ(left) and η(right) track - calorimeter residuals for CC

where the terms are called the constant, sampling, and noise term, respectively. The sampling term is determined from test beam data and has values of 0.15 GeV$^{1/2}$ for CC calorimeter and 0.206 GeV$^{1/2}$ for EC calorimeter. The noise term is very small relative to the other terms for the energy range encountered in this analysis. It has been set to 0.29 GeV [13] for CC and 0.125 for EC.

The value of C in the simulation is determined using maximum likelihood method and $Z \to ee$ width method until the rms from the MC invariant mass distribution matches with the width measured from the real data. For Z width method, we fit the invariant mass distribution with Breit-Wigner convoluted with a Gaussian function plus an exponential function (for Drell-Yan background). Figure 76 shows the maximum likelihood versus the CC constant term, we fit it with a quadratic function to get the minimum value and the statistical error. And it also shows the width of the CC-CC $Z \to ee$ candidates from Monte Carlo as a function of the CC constant term, along with the result from the data. The intersection of the two gives the constant term. The constant term in the CC is thus determined to be $(4.08 \pm 0.30)\%$, $(4.00 \pm 0.50)\%$ for positive EC and $(1.10 \pm 0.70)\%$ for negative EC.

6.1.4 Electron Position Resolution

Position resolutions for the EM calorimeter are determined from data using a sample of electrons required to pass preselection cuts (see section 4.1). The resolution is measured by fitting a gaussian shape to histograms of the track-calorimeter position residuals. The η and ϕ values are measured separately for CC and EC and assigned a conservative uncertainty of 50%. The η resolutions are $\sigma_\eta = 0.0070 \pm 0.0035$ for CC and $\sigma_\eta = 0.0029 \pm 0.0015$ for EC. The ϕ resolutions are $\sigma_\phi = 0.0068 \pm 0.0034$ for CC and $\sigma_\phi = 0.0041 \pm 0.0021$ rad for EC. For CC, however, σ_ϕ is found to be highly dependent on the position of the electron with respect to the EM tower boundaries and must be modeled more carefully. See section 6.1.5.

6.1.5 Electron Phimod Shift

As is described in section 2.1, the measured electron calorimeter detector phi positions tend to shift away from module boundaries and toward cell centers. Scatter plots of phimod shift vs track phimod position, as shown in figure 2, are used directly in PMCS to determine the amount to shift the CC electrons. The plot shown in figure 2 is actually divided into three bins in both p_T and $|\eta_{physics}|$ for PMCS. Figures 77 and 78 are PMCS to data comparisons of W and Z candidate electron phimod position after this correction is applied.

6.1.6 Hadronic Energy Scale

Of particular importance is the response of the detector to the recoil jet in W and Z production. The energy scale of the measured recoil momentum differs from the electron energy scale because the recoil measurement also includes energy from hadronic showers and suffers from the loss of energy in uninstrumented regions of the calorimeter. The response of the hadronic calorimeter relative to the response of the electromagnetic calorimeter was determined from $Z \rightarrow ee$ events. In $Z \rightarrow ee$ events the transverse momentum of the Z boson, p_T^Z, can be obtained from either the measurement of the transverse momenta of the two electrons $p_T^{\vec{ee}}$ or from the recoil activity in the event $-p_T^{\vec{rec}}$. To minimize the effects of the energy scale relative to the electromagnetic energy scale, the momentum imbalance was measured with respect to the (η, ξ)-coordinate system. The η axis is defined as the bisector of the two electron transverse directions. In the plane of the electrons, the axis orthogonal to the η axis is the ξ axis. See Figure 73.

The hadronic response is determined by plotting $p_T^{\vec{ee}} \bullet \hat{\eta}$ versus $< p_T^{\vec{rec}} \bullet \hat{\eta} >$, shown in Figure 79. The slope is determined to be $\kappa = 0.67 \pm 0.02$. The offset in response, obtained from the intercept of the fit is 0.10 ± 0.10 GeV, consistent with zero.

6.1.7 Hadronic Energy Resolution

The hadronic energy resolution is parameterized in the same way as the electron energy resolution, and from the studies done by the JES group [14], it is found to have a constant term of 0.05 ± 0.01 and a sampling term of 0.80 ± 0.20 GeV$^{1/2}$.

6.1.8 Underlying Event

The underlying event is modeled by randomly selecting an event from a sample of over 1,000,000 minimum bias events. A 2-D scatter plot of the x and y components of the MET for these events is input into PMCS and added to the recoil.

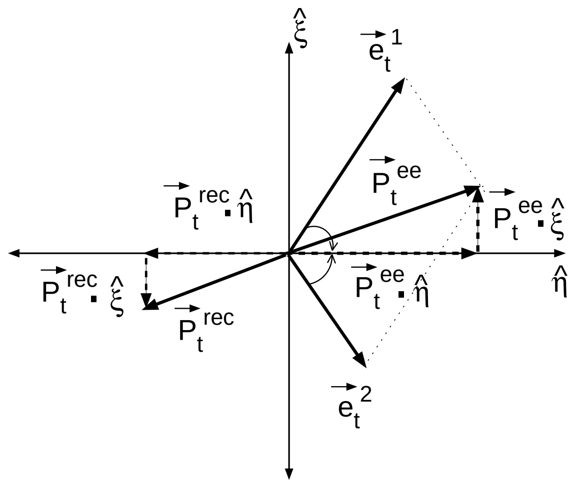

Figure 73: Definition of the η-ξ coordinate system in a $Z \to ee$ event. The $\hat{\eta}$ axis is the bisector of the electron directions and the $\hat{\xi}$ axis is perpendicular $\hat{\eta}$.

6.1.9 $u_{\parallel}$ correction

The electron energy is measured as the energy in a window of 5×5 towers, this region is excluded from the computation of MET. The size of the window is selected so that leakage of the electron shower out of the window is negligible, however, leakage of energy from the underlying event into the electron window can not be avoided, the underlying event energy in the electron window will bias the recoil measurement.

We must correct the recoil, u_T, for the momentum that is lost by excluding the electron window. The momentum that is lost always points in the direction of the electron and therefore biases the component of the recoil parallel to the electron, $u_{\parallel}$, towards negative values. Since for $p_T^W \ll M_W$

$$m_T \approx 2p_T(e) + u_{\parallel} \tag{15}$$

any $u_{\parallel}$ bias directly propagates into a bias on the transverse mass, we call this bias $\Delta u_{\parallel}$ and have to apply correction in the MC simulation.

The $u_{\parallel}$ correction is very sensitive to the ratio of W events with $u_{\parallel} > 0$ and $u_{\parallel} < 0$, we change the $u_{\parallel}$ correction in the Monte Carlo simulation until MC gives the same ratio as data. From Figure 81, we can determine the $u_{\parallel}$ correction to be -1.78 ± 0.01 GeV for CC region, -0.40 ± 0.40 GeV for the negative EC region, and -2.40 ± 0.40 GeV for the positive EC region.

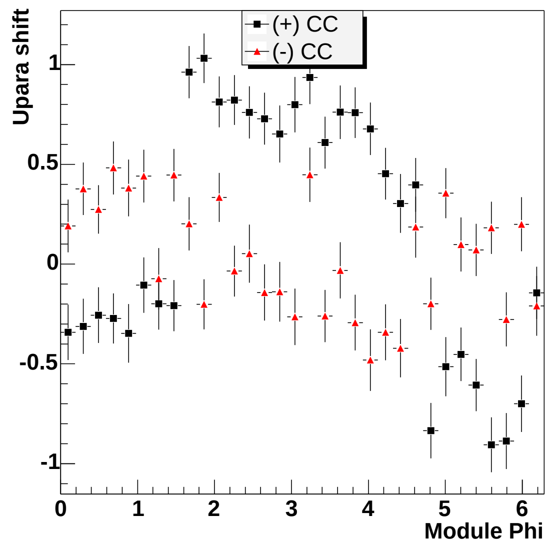

Figure 74: relative $u_{\|}$ shift as a function of ϕ_{det} and divided into halves in η_{det} for CC

The $u_{\|}$ correction is calibrated further in the central region. A histogram is made by taking the plot shown in figure 5, of the $u_{\|}$ cut equally dividing the W candidate sample as a function of phi module and η_{det} half, and subtracting the CC average cut. The corresponding (phi,η_{det}) bin in this histogram, shown in figure 74, is then added to the CC region $u_{\|}$ correction.

6.1.10 Electron Selection and Trigger Efficiencies

All efficiencies are input into PMCS, these include preselection, track matching, trigger and electron likelihood efficiency. The actual distributions used by PMCS have been shown in previous sections of the note. See table 5 for a summary of distributions used.

6.2 Acceptance Determination Method

For each generated event the following steps are applied in PMCS. First, final-state radiated photons within 0.2 in ΔR of an electron are added via four-vector addition into the generated electron. The radius of 0.2 very roughly corresponds to the reach of the EM clustering algorithm used in the data. Using the generated event vertex, the known magnetic field, and the known calorimeter geometry, the η and ϕ position of each generated electron

Efficiency	Binned according to..	shown in figure(s)
Preselection (CC)	track $phimod_{det}$	22
Preselection (EC)	track η_{det}	21
Track	η_{det} and z vertex	40
Trigger (runs $\leq$ 178721)	p_T, η_{det} and z vertex	46 and 47
Trigger (runs $\geq$ 178722)	p_T, η_{det} and z vertex	48 and 49
Electron Likelihood	η_{det} and z vertex	66

Table 5: Efficiency Input Histogram Summary

and photon at the third-layer of the EM calorimeter is determined.

In order to simulate efficiencies, a random number is generated in a flat distribution between zero and one for each of the electrons in the generated event. If larger than the respective efficiency, the electron is said to fail that efficiency.

Preselection is the first efficiency applied to the electrons. Those that fail are removed from consideration. For electrons in the CC region, the preselection efficiency is applied as a function of phimod position. In the EC region it is applied as a function of detector eta only.

After the preselection efficiency is applied, the phi and eta position of the remaining electrons is smeared. For CC electrons, the phimod shift described in section 6.1.5 is applied. For electrons in the EC region the phi position is smeared by the measured resolution. For all electrons, the eta position is smeared by the measured eta resolution.

A random run number (weighted by luminosity) from the list of runs used in the data sample is then assigned to the event. Electrons are rejected if they have an eta-phi position that falls into a bad calorimeter region that is active for the associated run.

The generator-level energy of each electron and photon is shifted and smeared by the measured electron energy scale and resolution, respectively. The transverse recoil energy (all energy except MET and electrons) is shifted and smeared by the measured hadronic energy scale and resolution, respectively. The adjusted transverse recoil energy, along with the adjusted electron energies, is used to recalculate the MET. The underlying event energy is then added to the MET, and the $u_{\parallel}$ correction is applied.

The geometric acceptance cuts (pseudorapidity cut and the is_in_fiducial requirement) and E_T cut are applied and the remaining efficiencies are simulated. W and Z event selection cuts are then applied in a manner similar to data.

The total Z (or W) acceptance is then given by the ratio of the number of accepted Z (or W) candidate events to the total number of generated events.

6.3 Comparisons to Data

6.3.1 Imbalance and Recoil

The η and ξ imbalance in Z events are defined as:

- $\eta_{imb} = (p_T^{\vec{ee}} + p_T^{\vec{rec}}) \bullet \hat{\eta}$
- $\xi_{imb} = (p_T^{\vec{ee}} + p_T^{\vec{rec}}) \bullet \hat{\xi}$

where $\hat{\eta}$ and $\hat{\xi}$ are unit vectors along the η and ξ axis respectively. Figure 82 compares the η and ξ imbalance for data and PMCS. There is good agreement in both the mean and width of each distribution, indicating that PMCS correctly models the hadronic energy resolution and energy scale.

We also compare $u_{\parallel}$ distribution for the electrons from W production in Figure 83. $u_{\parallel}$ is the projection of the momentum recoiling against the W boson along the electron: $u_{\parallel} = p_T^{\vec{rec}} \bullet \hat{e}$, where $\hat{e}$ is a unit vector in the electron direction. We observe good agreement between the data and PMCS.

6.3.2 General Distributions

PMCS is compared to data after acceptance and efficiency effects are applied. Z candidates are compared to a sum of PMCS and QCD background estimations with an additional histogram showing background only. Agreement with data in the central region is quite good overall. For W candidates, true W events after QCD background subtraction are compared directly to PMCS with an additional histogram for all W candidates. This representation for W events is preferable because it is possible for background estimation to be negative in some bins with large error due to dependence of the calculation on likelihood efficiency derived from Z data statistics. For W candidates, agreement is good in the central region with the possible exceptions of transverse mass and MET. So that the end caps can be examined, EC only events (W EC and Z EC-EC candidates) are allowed to have a tight electron in the end caps instead. EC only events are not used in this analysis and, for many distributions, agreement is poor. For data to PMCS comparisons, see Figures 84 to 92 for Z candidates and Figures 93 to 105 for W candidates (dots always for data, lines for PMCS).

Descriptor	Value
EM Energy Scale (CC)	1.0054 ± 0.0020
EM Energy Offset (CC)	(0.191 ± 0.048) GeV
EM Sampling Term (CC)	0.15 $\mathrm{GeV}^{1/2}$
EM Constant Term (CC)	$(4.08 \pm 0.30)\%$
EM Energy Scale (pEC)	0.9990 ± 0.0066
EM Energy Offset (pEC)	(0.574 ± 0.300) GeV
EM Energy Scale (nEC)	0.9600 ± 0.0129
EM Energy Offset (nEC)	(0.070 ± 0.499) GeV
EM Sampling Term (EC)	0.206 $\mathrm{GeV}^{1/2}$
EM Constant Term (pEC)	$(4.00 \pm 0.50)\%$
EM Constant Term (nEC)	$(1.10 \pm 0.70)\%$
Calorimeter Position Resolution $\sigma_{\eta^{det}}$ (CC)	0.0070 ± 0.0035
Calorimeter Position Resolution σ_{ϕ} (CC)	(0.0068 ± 0.0034) rad
Calorimeter Position Resolution $\sigma_{\eta^{det}}$ (EC)	0.0029 ± 0.0015
Calorimeter Position Resolution σ_{ϕ} (EC)	(0.0041 ± 0.0021) rad
HAD Energy Scale	0.67 ± 0.02
HAD Sampling Term	(0.80 ± 0.20) $\mathrm{GeV}^{1/2}$
HAD Constant Term	0.05 ± 0.01
Underlying Events	(3.02 ± 0.04) GeV
$u_{\parallel}$ Correction (CC)	(-1.78 ± 0.01) GeV
$u_{\parallel}$ Correction (nEC)	(-0.40 ± 0.40) GeV
$u_{\parallel}$ Correction (pEC)	(-2.40 ± 0.40) GeV
$\Delta R(e\gamma)$	0.2 ± 0.1

Table 6: Parameters used in PMCS

6.4 Acceptance Results

The acceptance values, after all event selection criteria are simulated in PMCS, are summarized in Table 7. The table also shows the acceptance value, A_R, for the ratio of the W to Z cross sections, where $A_R = A_W/A_Z$.

Acceptance	
$W \to e\nu$ (CC)	0.18254 ± 0.00007
$Z/\gamma^* \to ee$ (CC-CC)	0.10161 ± 0.00008
$Z/\gamma^* \to ee$ (CC-EC)	0.05518 ± 0.00006
$Z/\gamma^* \to ee$ (both)	0.15678 ± 0.00009

Table 7: Acceptance values calculated with PMCS. The errors shown reflect statistical uncertainties due to the number of generated events used in the sample. A complete accounting of the uncertainty on the acceptance values can be found in Section 6.5.

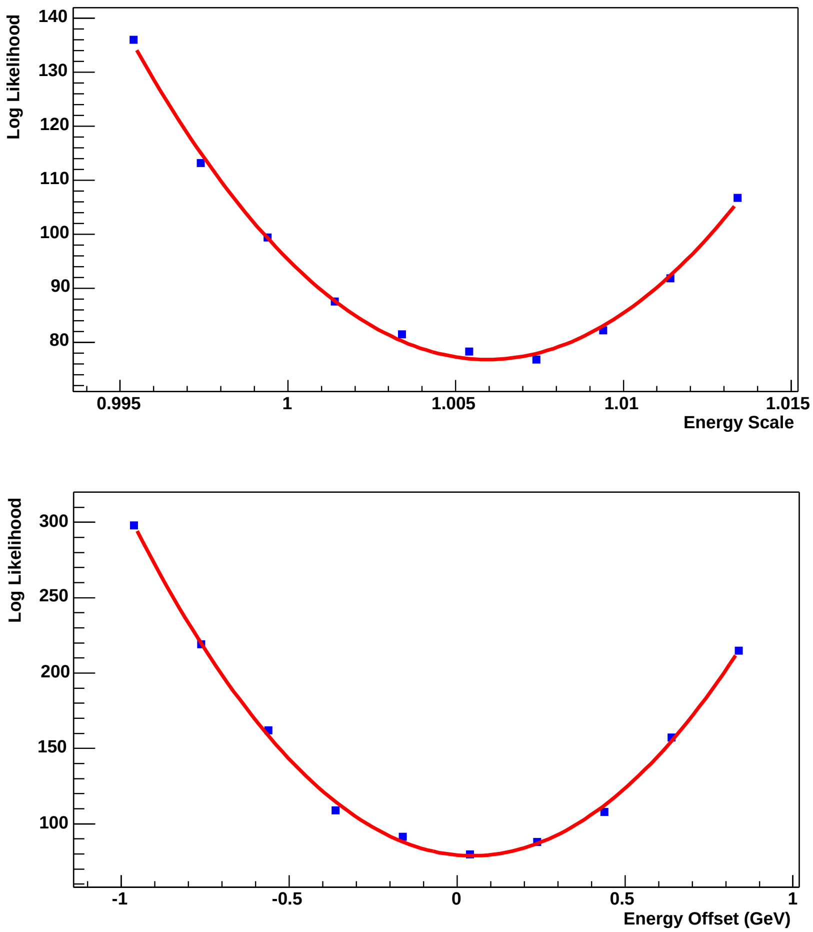

Figure 75: Maximum Likelihood vs CC energy scale and energy offset

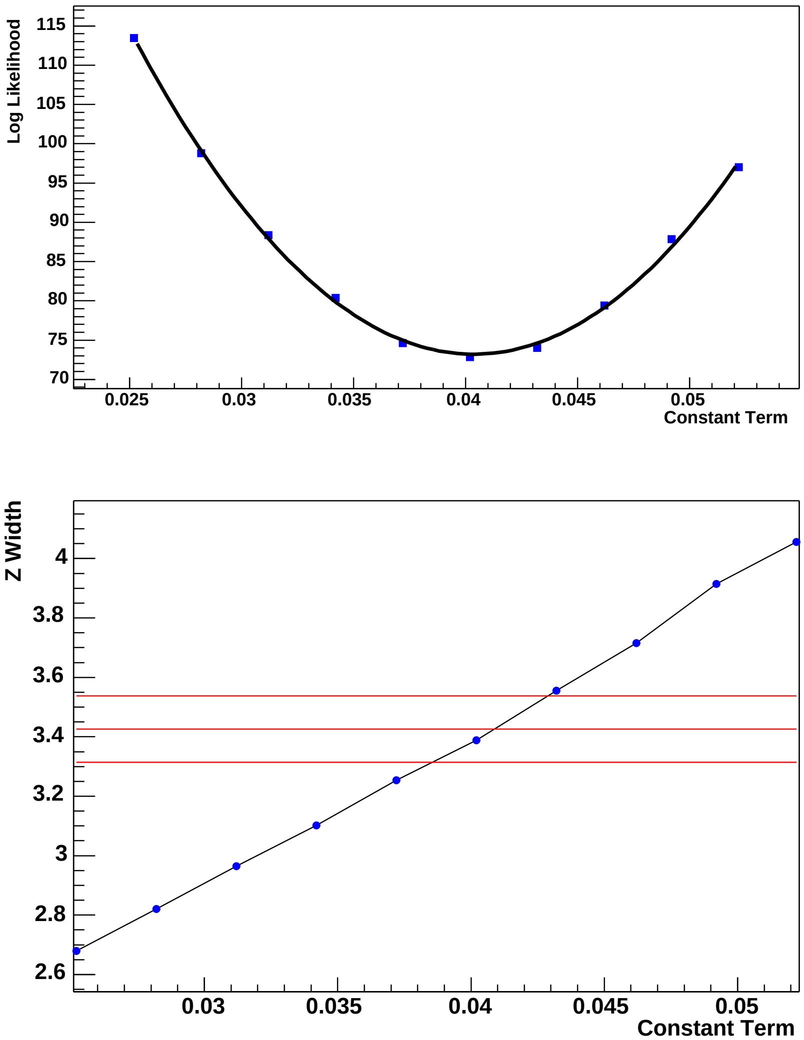

Figure 76: Maximum Likelihood vs CC constant term (Top) and Z width vs CC constant term (Bottom)

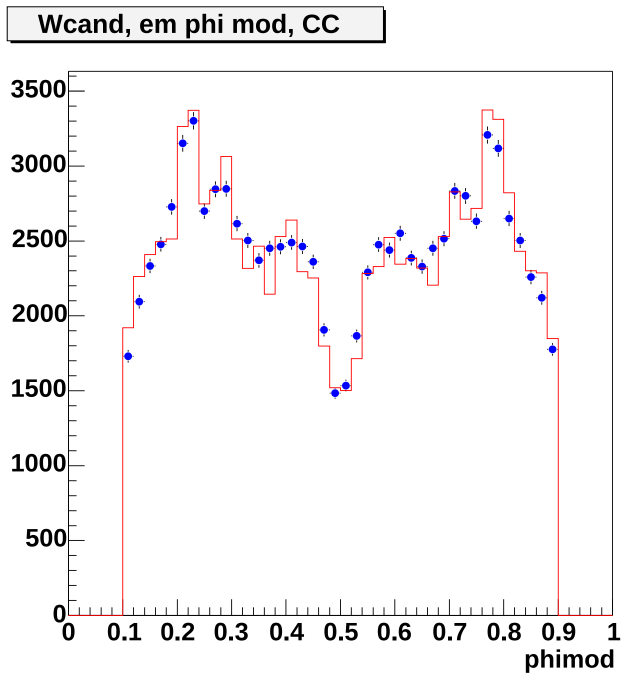

Figure 77: PMCS to data comparison for W candidate phimod position

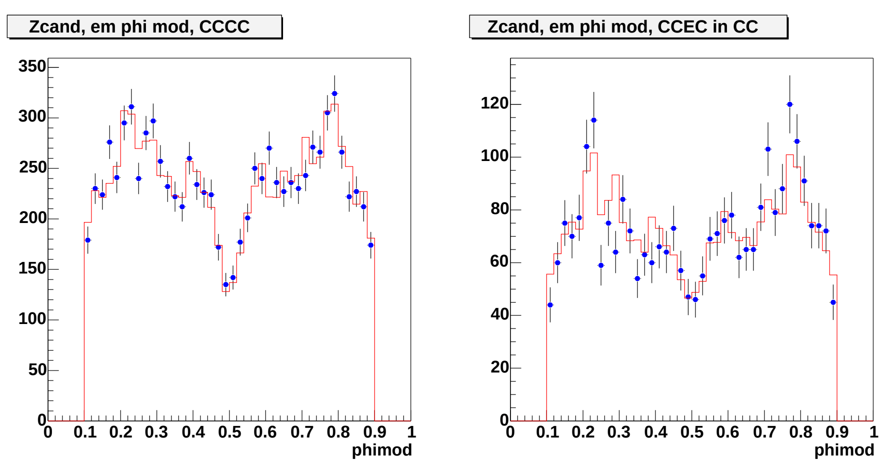

Figure 78: PMCS to data comparison for Z candidate phimod position CC-CC (Left) and CC-EC (Right)

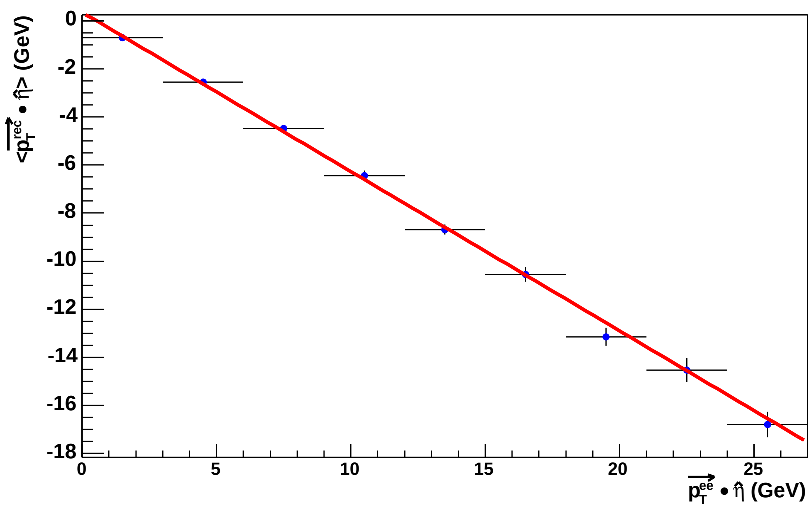

Figure 79: Average value of $p_T^{\vec{rec}} \bullet \hat{\eta}$ vs $p_T^{\vec{ee}} \bullet \hat{\eta}$ for $Z \rightarrow ee$ events, the line is obtained from a linear fit to the data

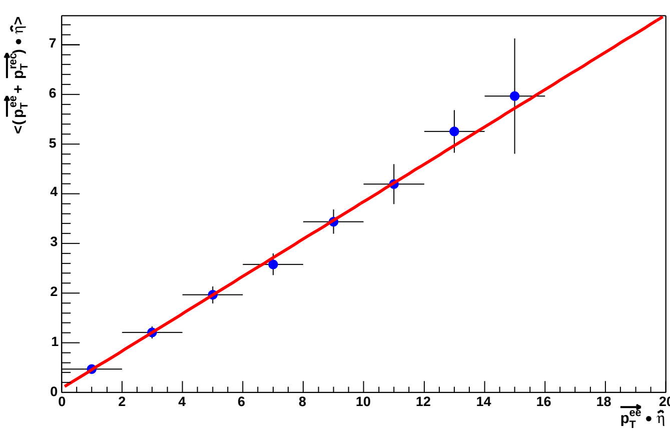

Figure 80: Average value of $(p_T^{\vec{ee}} + p_T^{\vec{rec}}) \bullet \hat{\eta}$ vs $p_T^{\vec{ee}} \bullet \hat{\eta}$ for $Z \rightarrow ee$ events, the line is obtained from a linear fit to the data

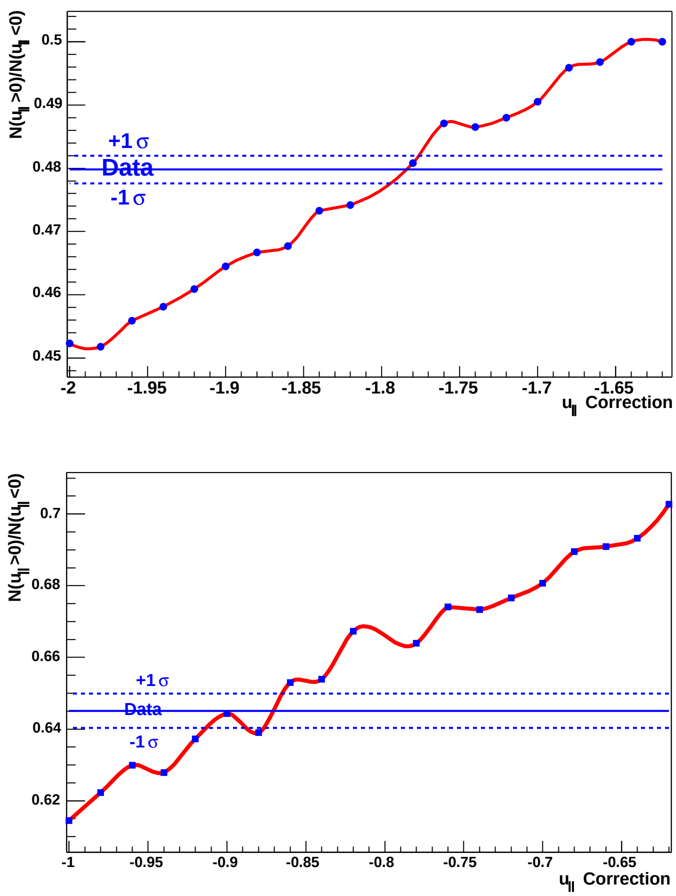

Figure 81: Determination of $u_{\parallel}$ correction $\Delta u_{\parallel}$ for CC region (Top) and EC region (Bottom). The curved r ed line connecting the Monte Carlo points shows the correlation between $u_{\parallel}$ correction vs $N(u_{\parallel} > 0)/N(u_{\parallel} < 0)$ from Monte Carlo. The horizontal solid line shows the ratio $N(u_{\parallel} > 0)/N(u_{\parallel} < 0)$ measured from data and the horizontal dashed lines the uncertainty on $N(u_{\parallel} > 0)/N(u_{\parallel} < 0)$. From the intersection of the data line with the curved line we determine the $u_{\parallel}$ correction to be -1.78 ± 0.01 GeV (CC) and -0.90 ± 0.02 GeV (EC).

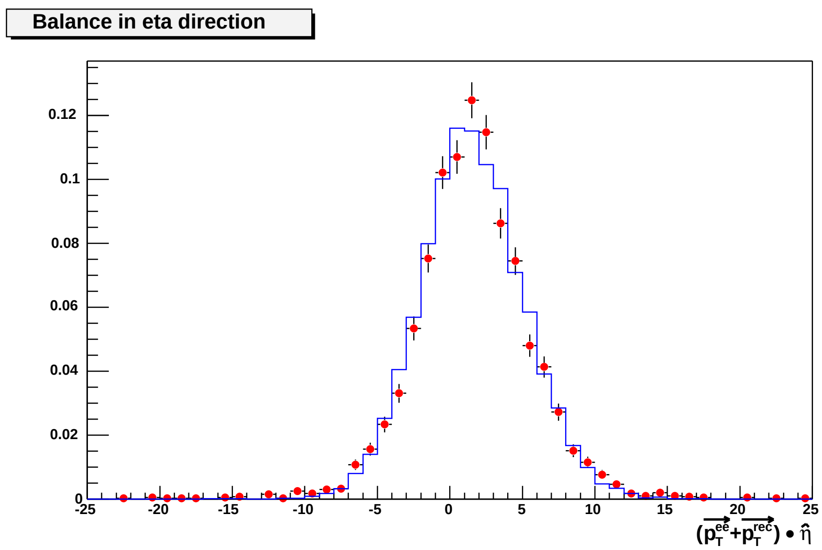

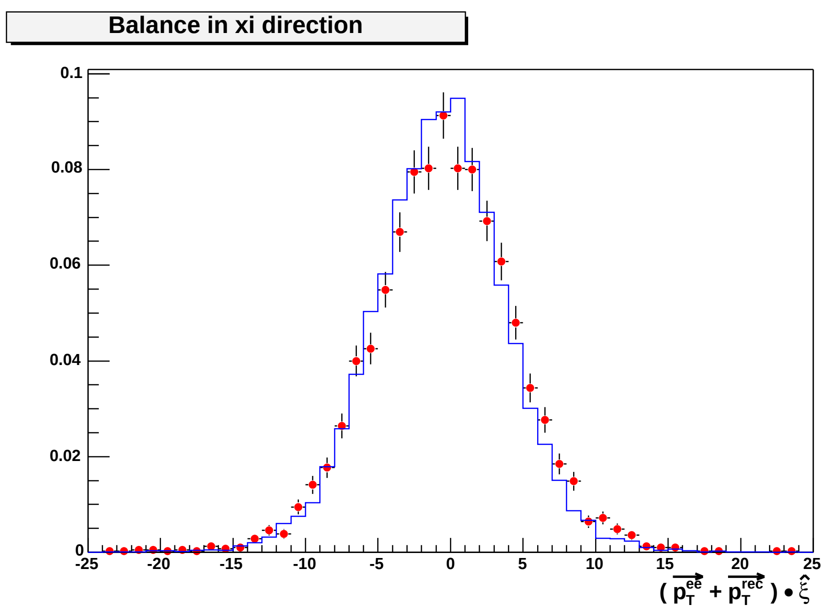

Figure 82: η and ξ balance for $Z \to ee$ events, Red dots for data, Blue histograms for PMCS, the total entries are normalized to 1

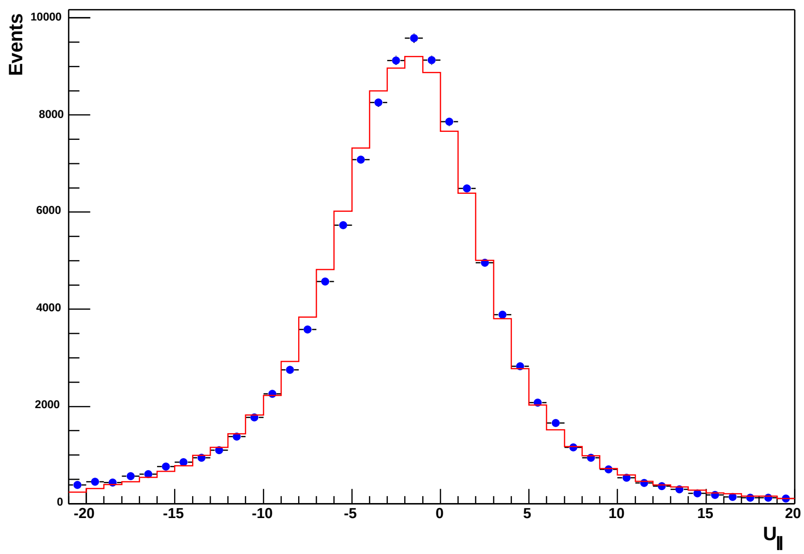

Figure 83: $u_{\|}$ distribution for all $W \to e\nu$ events (after subtracting QCD background using Matrix method), Blue dots for data, Red histograms for PMCS

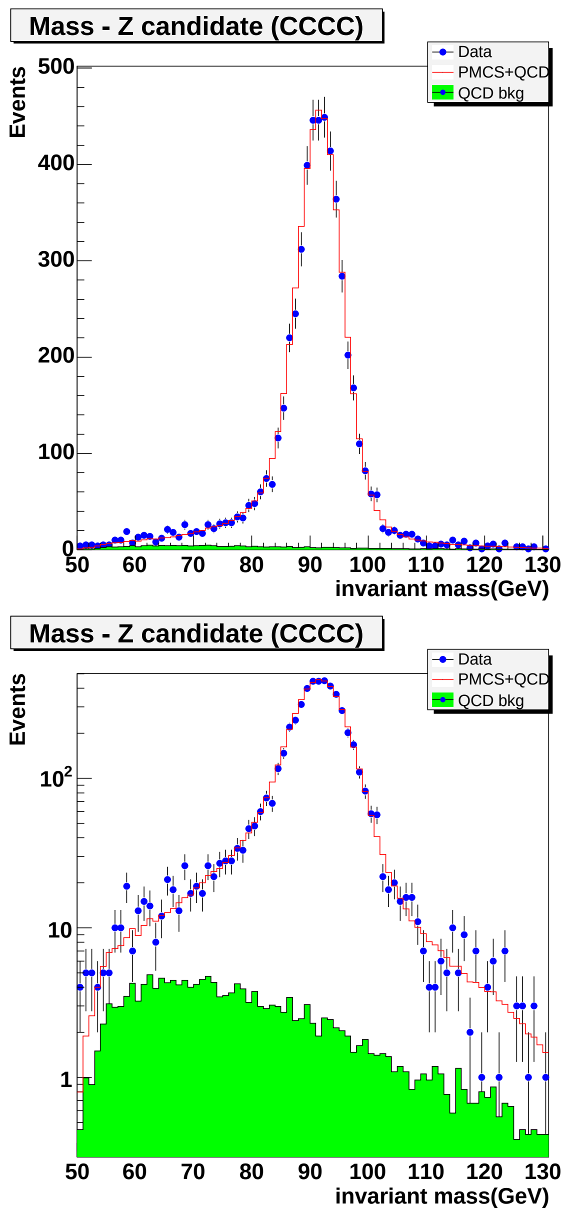

Figure 84: PMCS to data comparison of Z candidate invariant mass for CC-CC events shown with a linear scale (top) and log scale (bottom)

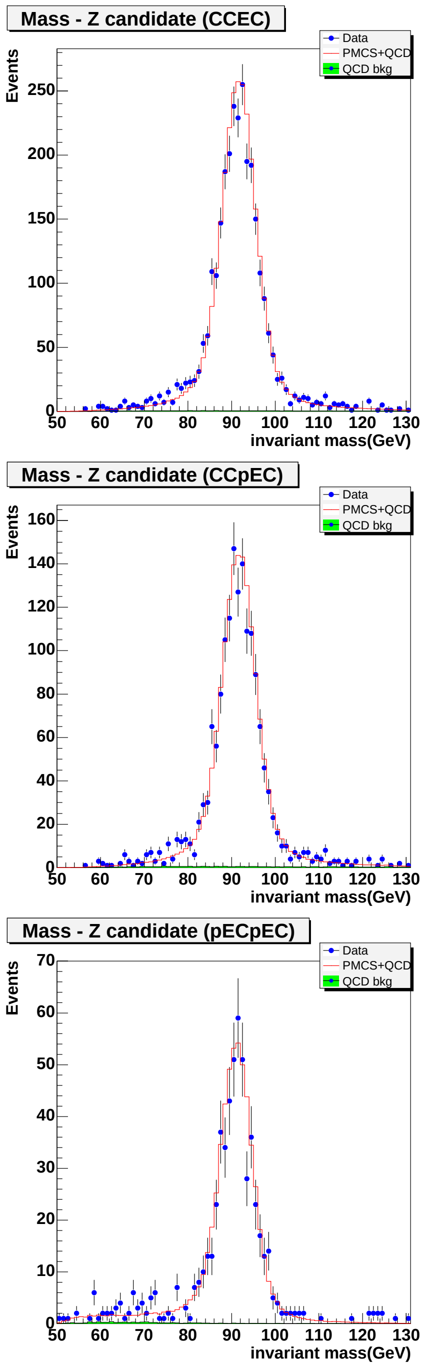

Figure 85: PMCS to data comparison of Z candidate invariant mass. The first row is CC-EC (left) and EC-EC (right), 2nd row is CC-EC where EC electron is in positive EC (left) and negative EC (right), third row is EC-EC where both electron are in positive EC (left) and negative EC (right).

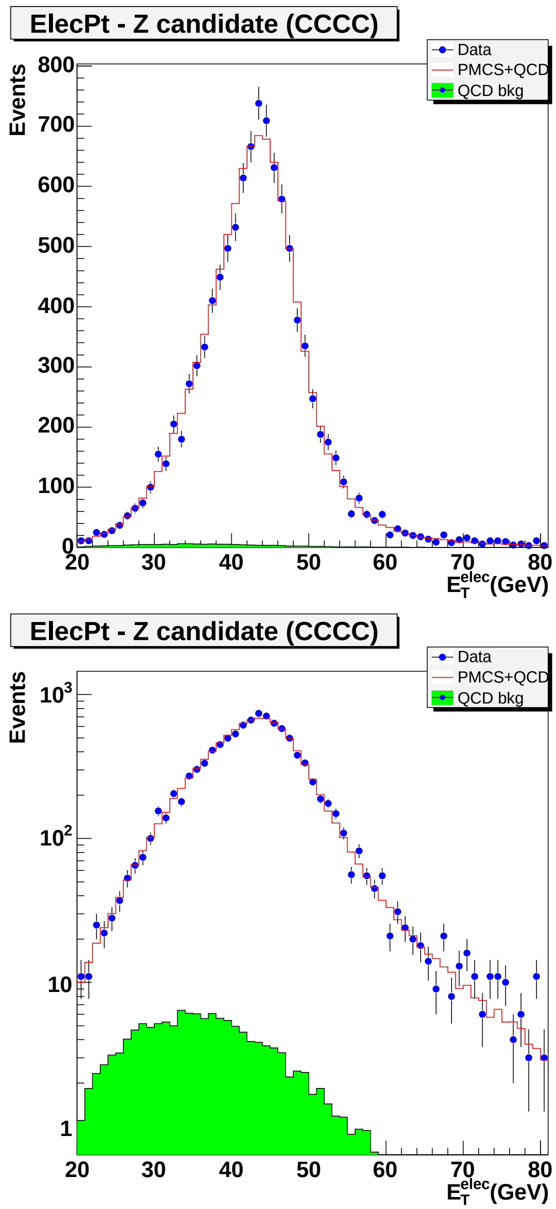

Figure 86: PMCS to data comparison of Z candidate electron E_T for CC-CC events shown with a linear scale (top) and log scale (bottom). The E_T cut is extended down to 20 GeV for this plot only in order to ensure reasonable behavior.

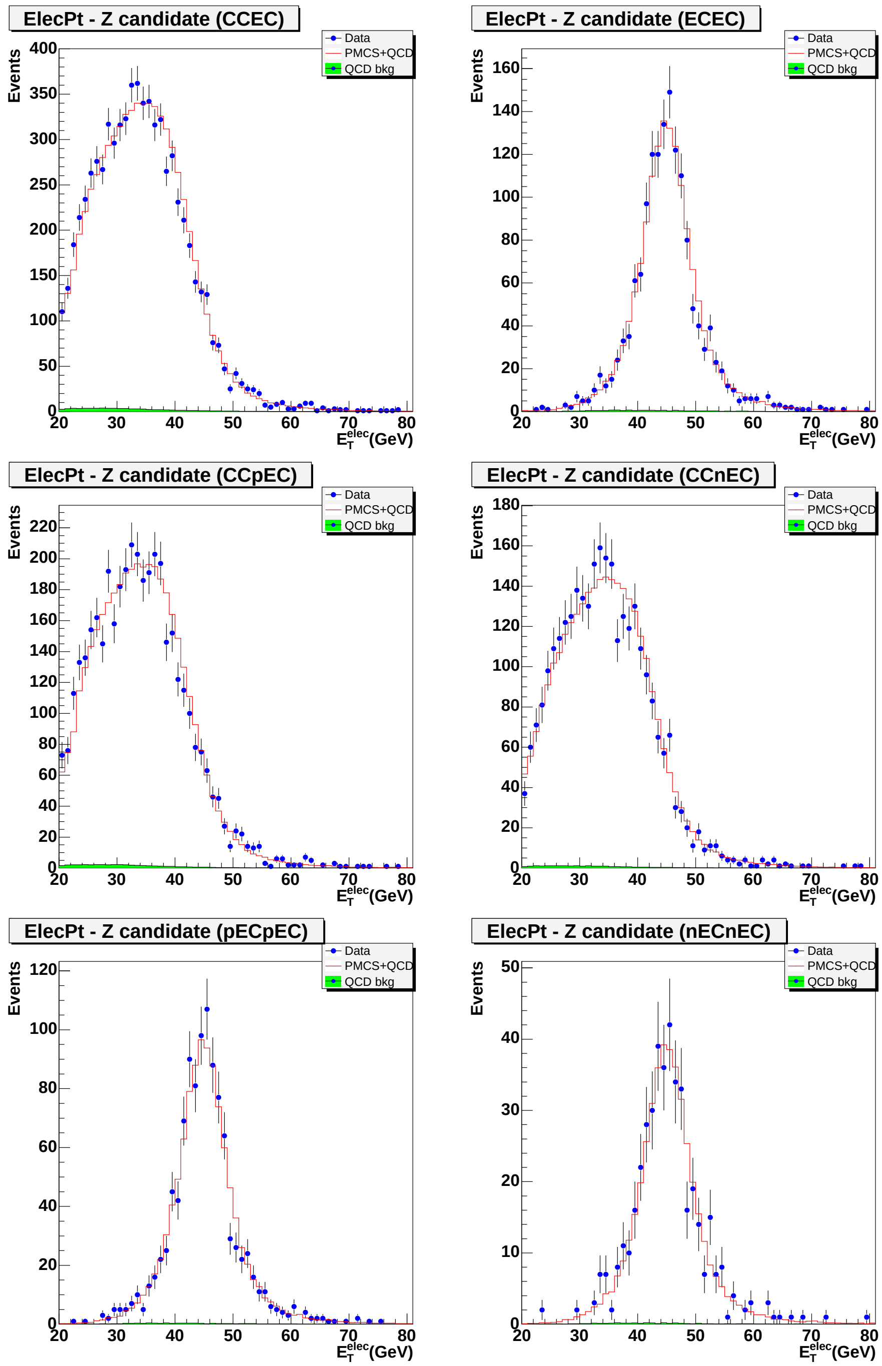

Figure 87: PMCS to data comparison of Z candidate electron E_T. The first row is CC-EC (left) and EC-EC (right), 2nd row is CC-EC where EC electron is in positive EC (left) and negative EC (right), third row is EC-EC where both electron are in positive EC (left) and negative EC (right). The E_T cut is extended down to 20 GeV for this plot only in order to ensure reasonable behavior.

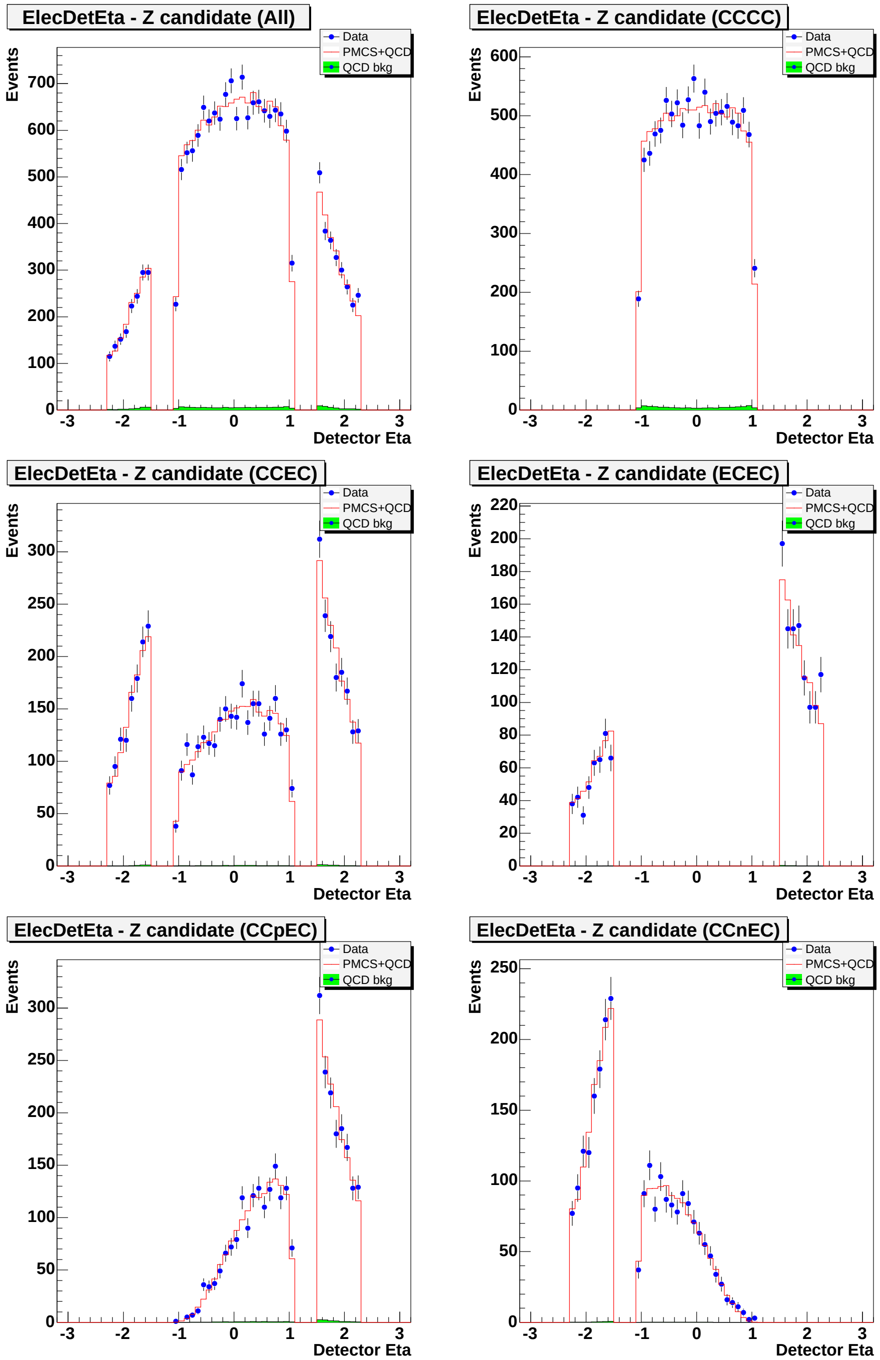

Figure 88: PMCS to data comparison of Z candidate electron η_{det}. The first row is for all events (left) and CC-CC (right), 2nd row is CC-EC (left) and EC-EC (right), 3rd row is CC-EC where EC electron is in positive EC (left) and negative EC (right).

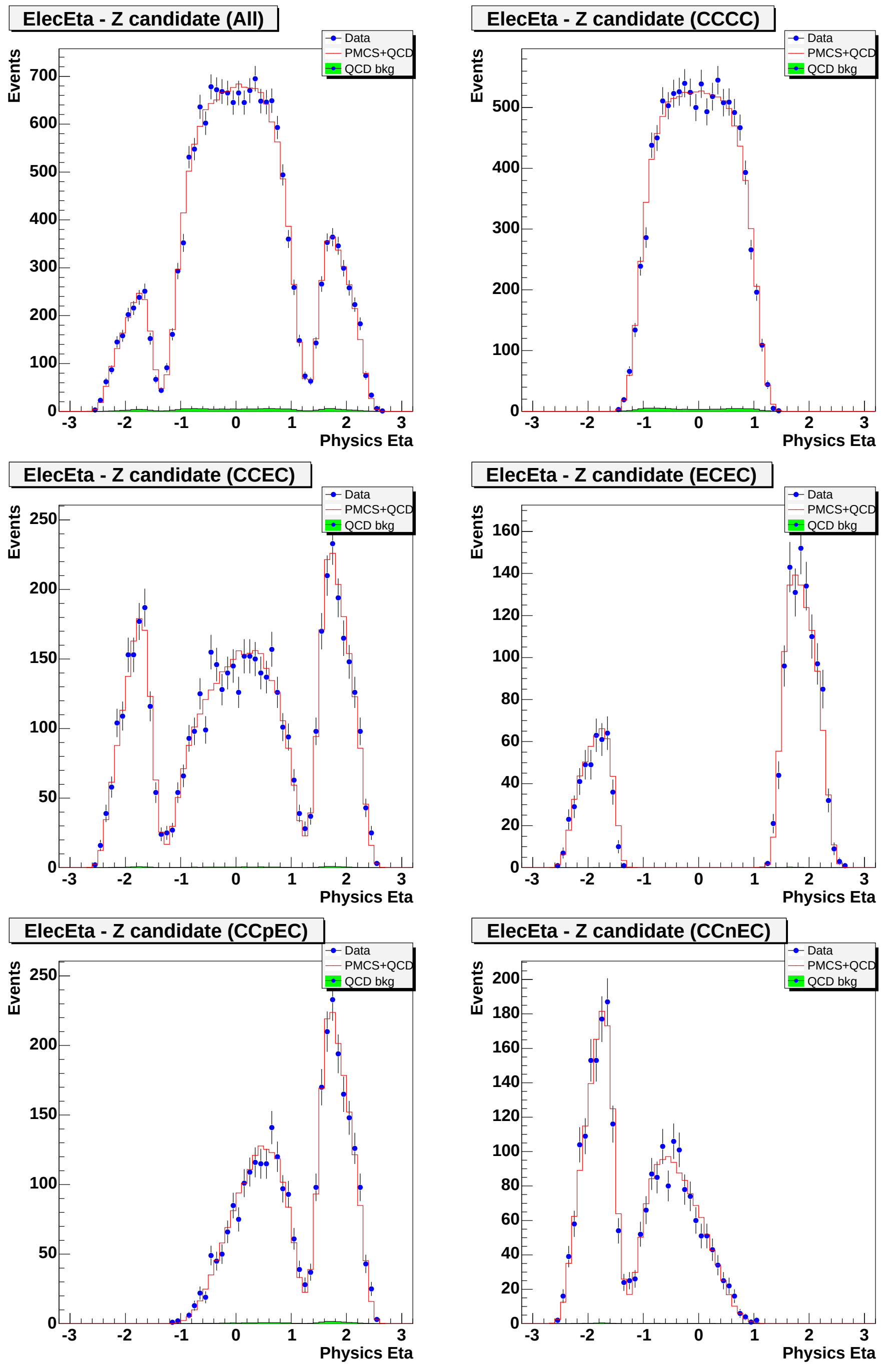

Figure 89: PMCS to data comparison of Z candidate electron $\eta_{physics}$. The first row is for all events (left) and CC-CC (right), 2nd row is CC-EC (left) and EC-EC (right), 3rd row is CC-EC where the EC electron is in positive EC (left) and negative EC (right).

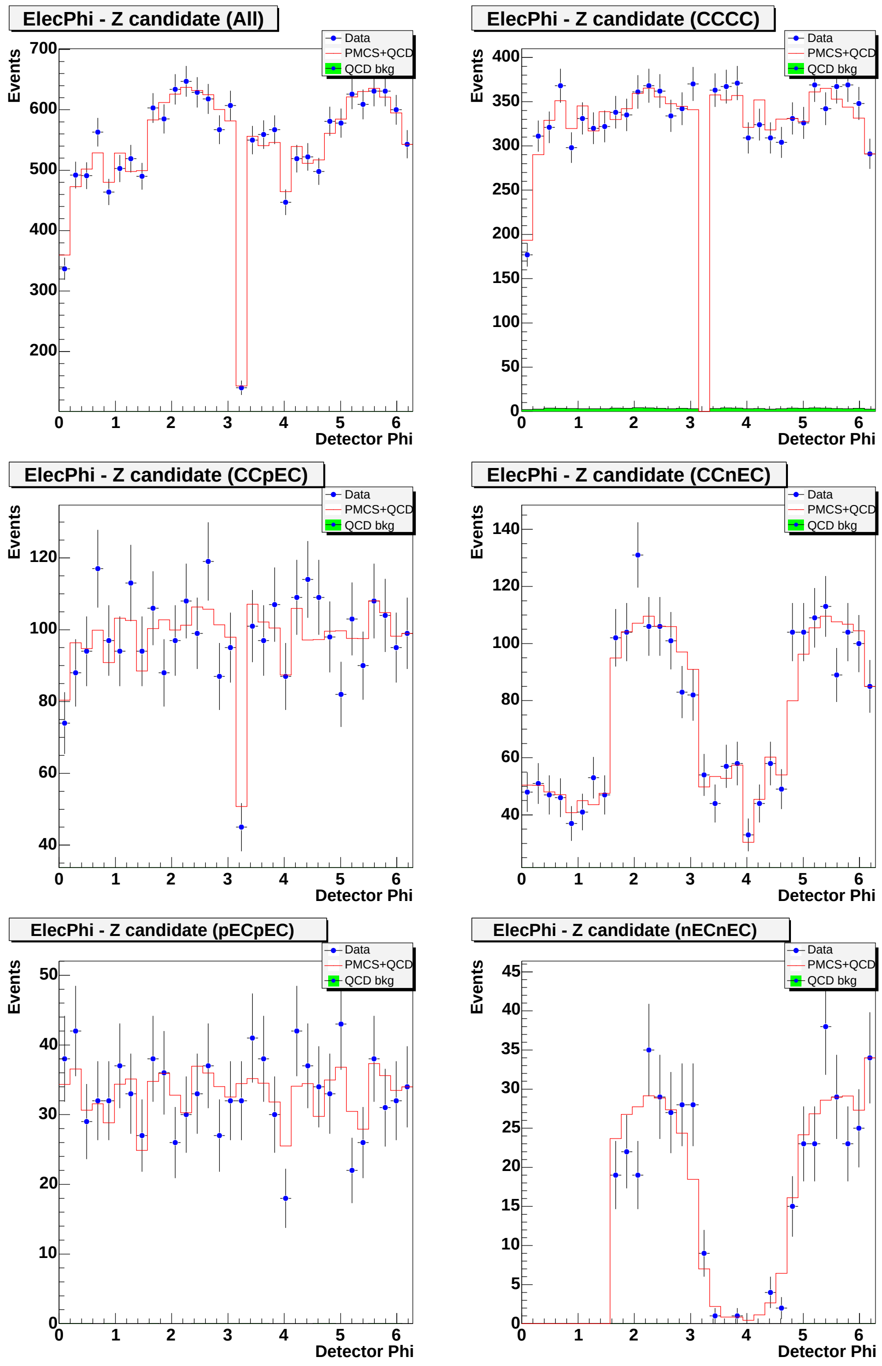

Figure 90: PMCS to data comparison of Z candidate electron ϕ. The first row is for all events (left) and CC-CC (right), 2nd row is CC-EC where EC electron is in positive EC (left) and negative EC (right), 3rd row is EC-EC where both electron are in positive EC (left) and negative EC (right).

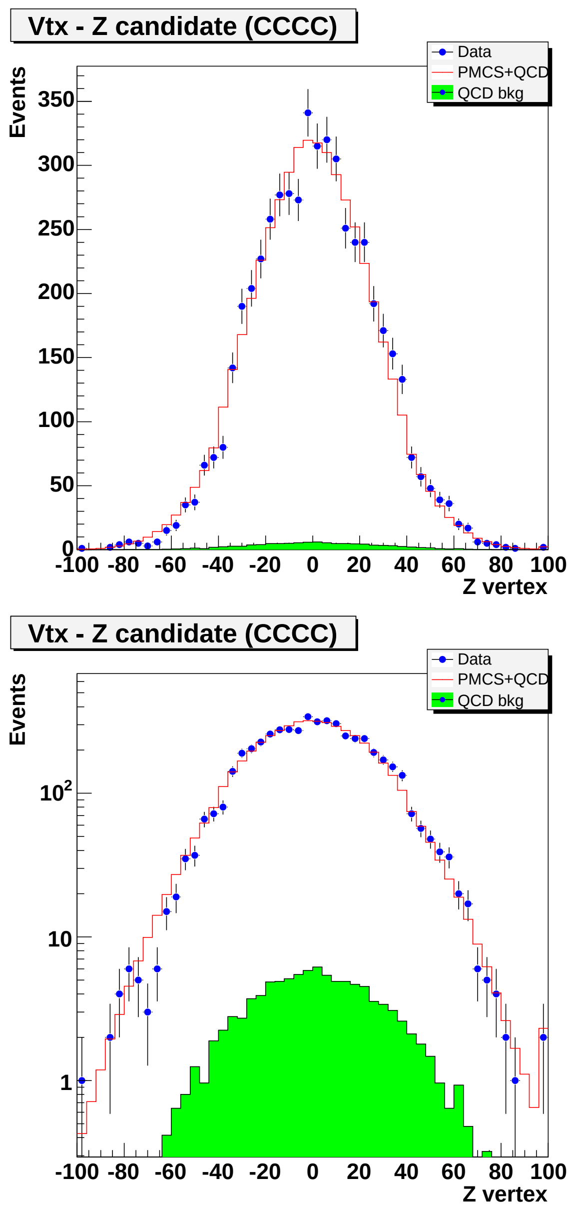

Figure 91: PMCS to data comparison of Z candidate primary vertex z for CC-CC events shown with a linear scale (top) and log scale (bottom)

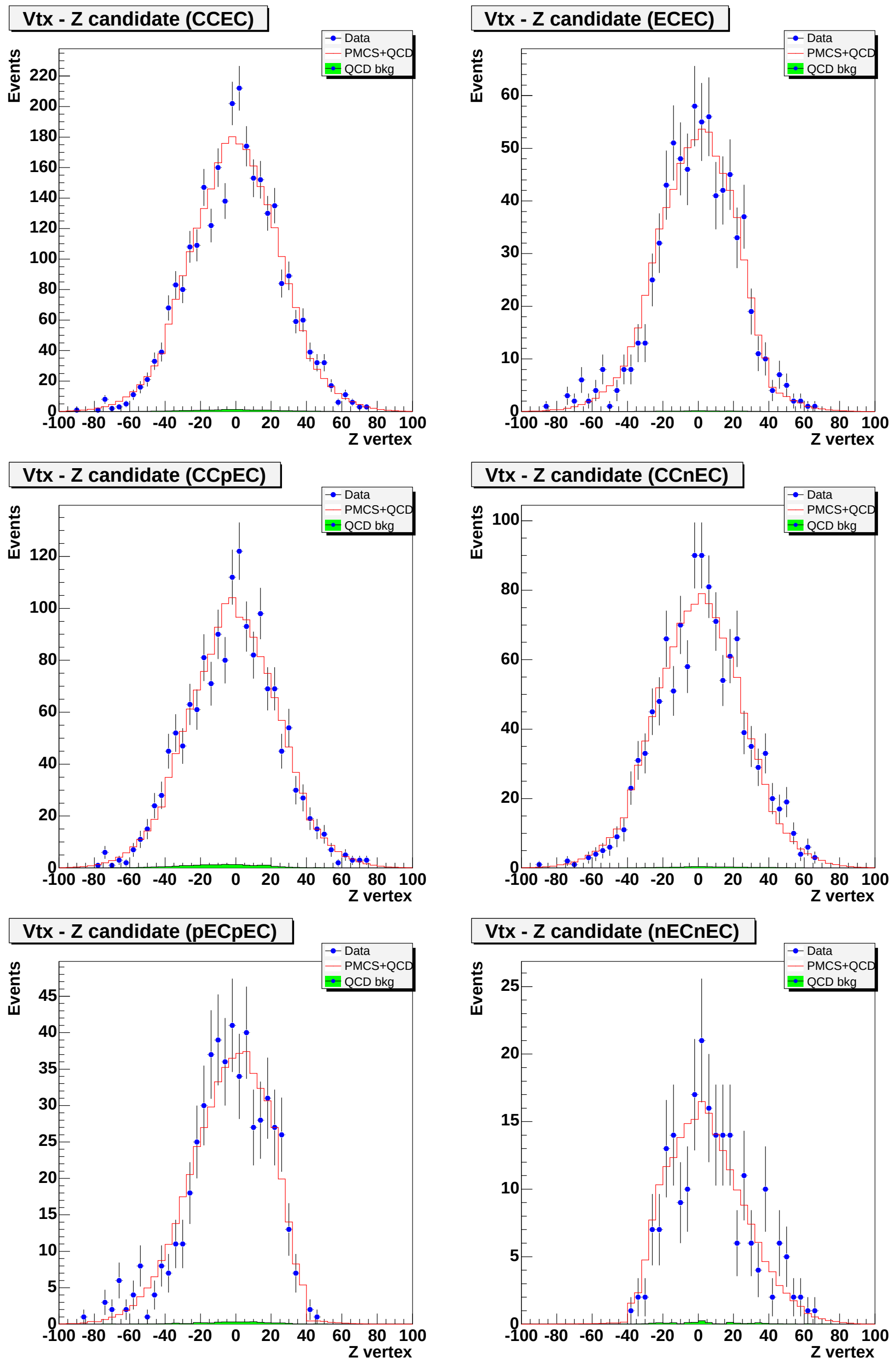

Figure 92: PMCS to data comparison of Z candidate primary vertex z. The first row is CC-EC (left) and EC-EC (right), 2nd row is CC-EC where EC electron is in positive EC (left) and negative EC (right), third row is EC-EC where both electron are in positive EC (left) and negative EC (right).

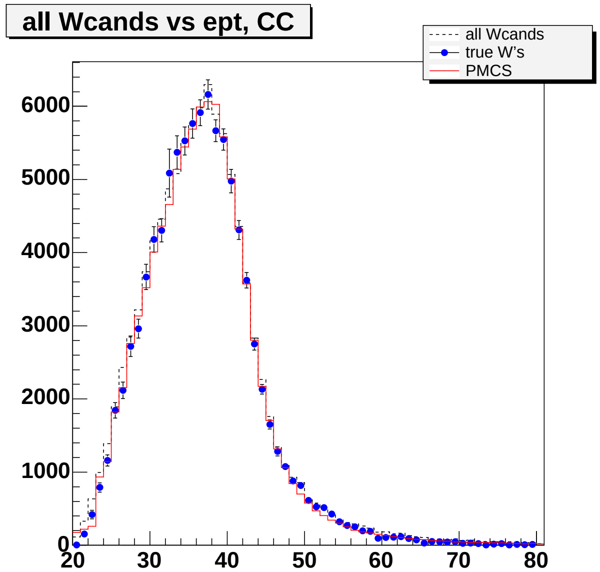

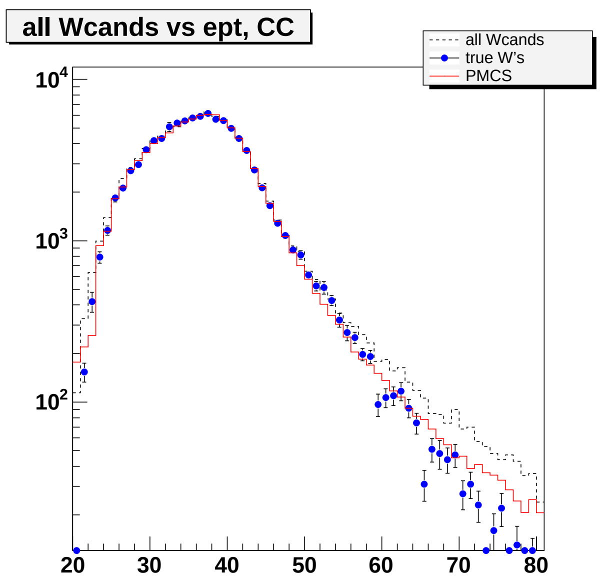

Figure 93: PMCS to data comparison of W background subtracted electron E_T for CC using a linear scale (top) and log scale (bottom). W candidates before background subtraction are represented by the black dashed histogram. The E_T cut is extended down to 20 GeV for this plot only in order to ensure reasonable behavior.

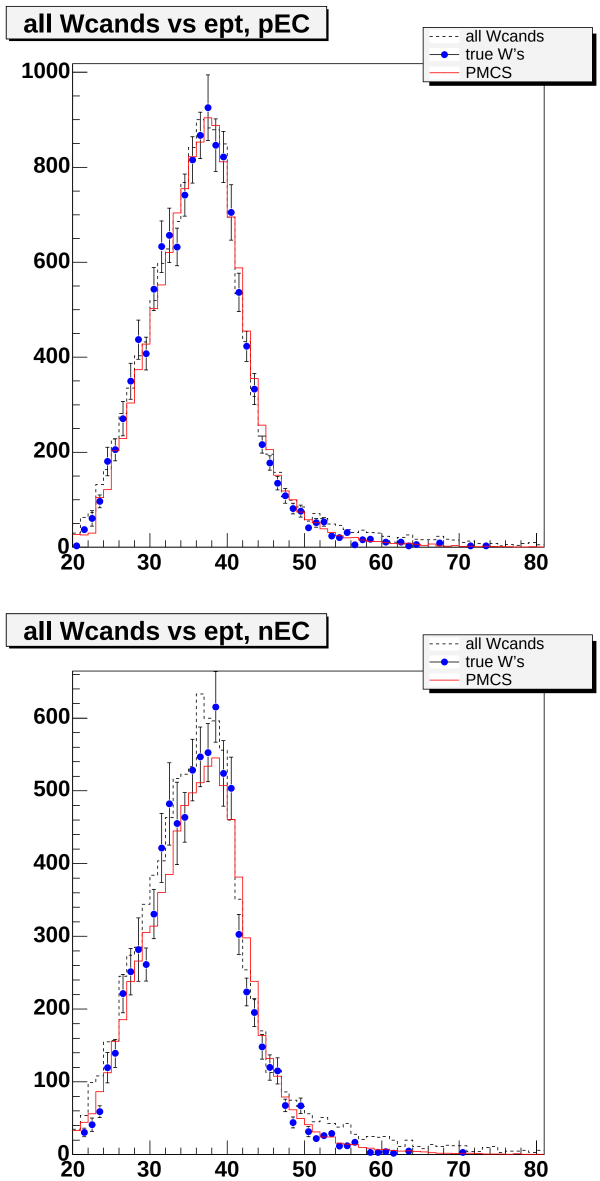

Figure 94: PMCS to data comparison of W background subtracted electron E_T for positive EC (top) and negative EC (bottom). W candidates before background subtraction are represented by the black dashed histogram. The E_T cut is extended down to 20 GeV for this plot only in order to ensure reasonable behavior.

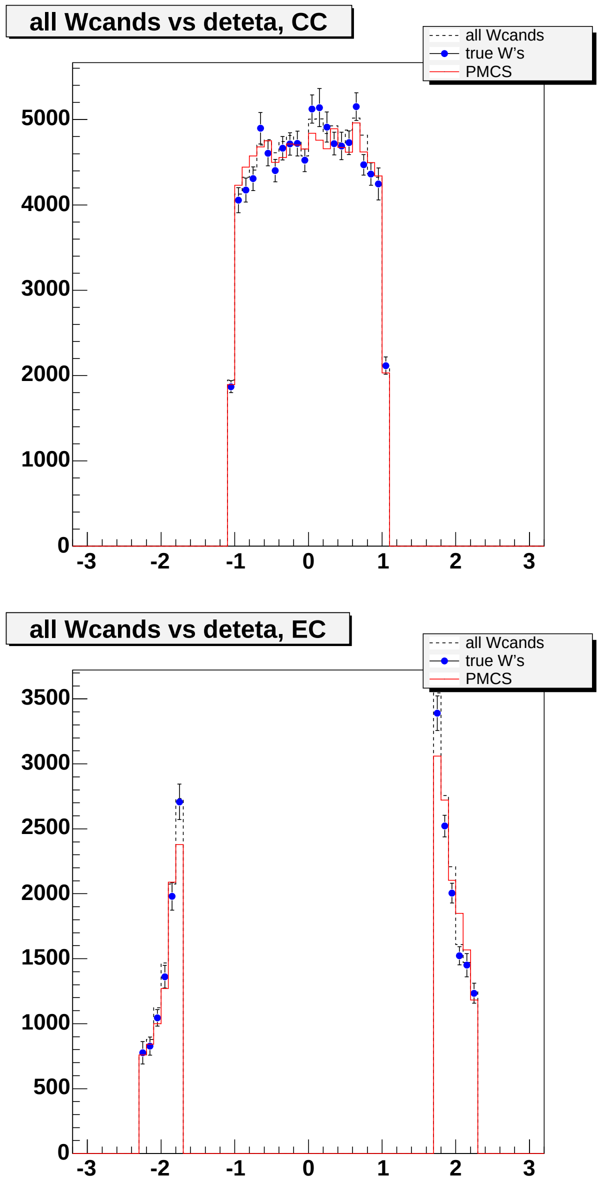

Figure 95: PMCS to data comparison of W background subtracted electron η_{det} for all events (top), CC (bottom left) and EC (bottom right). W candidates before background subtraction are represented by the black dashed histogram.

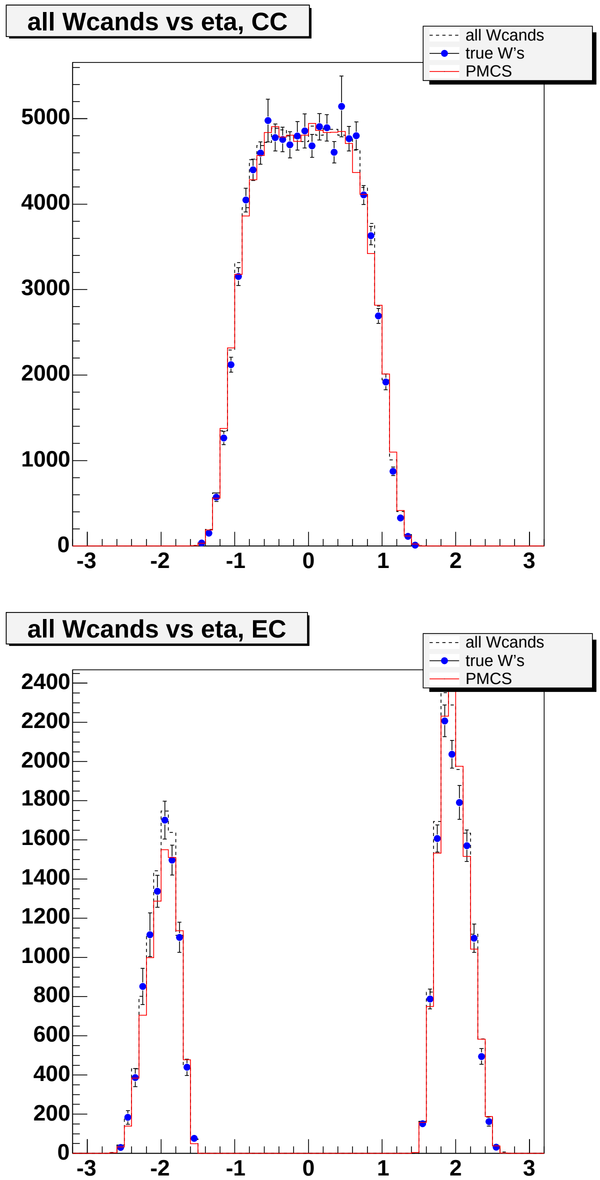

Figure 96: PMCS to data comparison of W background subtracted electron $\eta_{physics}$. The first row is for CC (left) and EC (right) and the 2nd row is positive EC (left) and negative EC (right). W candidates before background subtraction are represented by the black dashed histogram.

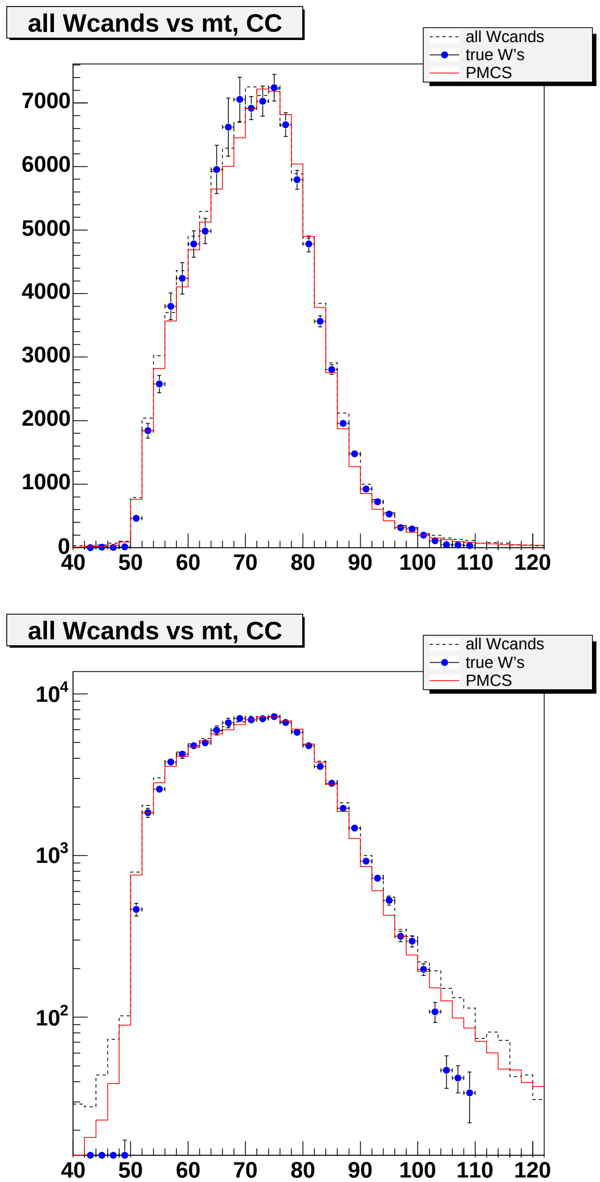

Figure 97: PMCS to data comparison of W background subtracted transverse mass for CC using a linear scale (top) and log scale (bottom). W candidates before background subtraction are represented by the black dashed histogram.

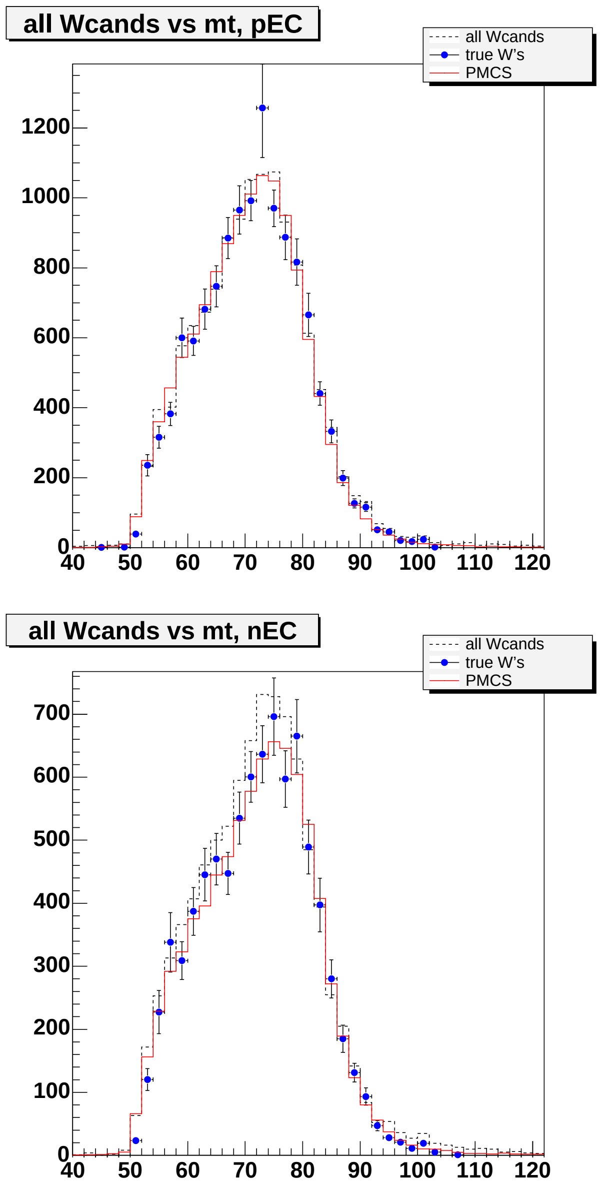

Figure 98: PMCS to data comparison of W background subtracted transverse mass for positive EC (top) and negative EC (bottom). W candidates before background subtraction are represented by the black dashed histogram.

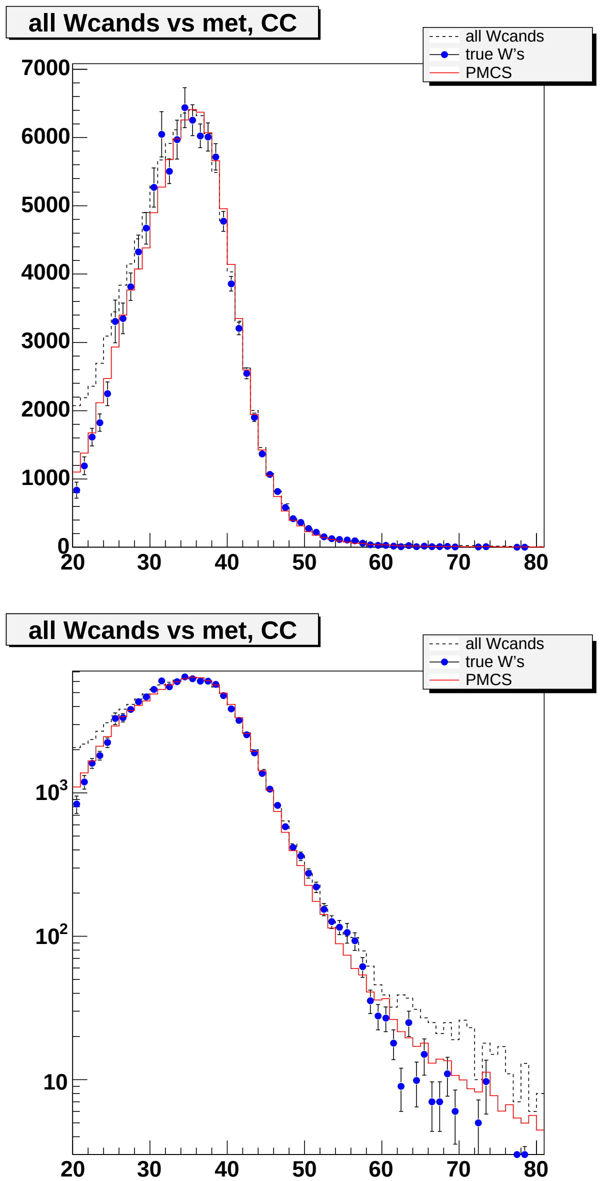

Figure 99: PMCS to data comparison of W background subtracted missing E_T for CC using a linear scale (top) and log scale (bottom). W candidates before background subtraction are represented by the black dashed histogram. The missing E_T cut is extended down to 20 GeV for this plot only in order to ensure reasonable behavior.

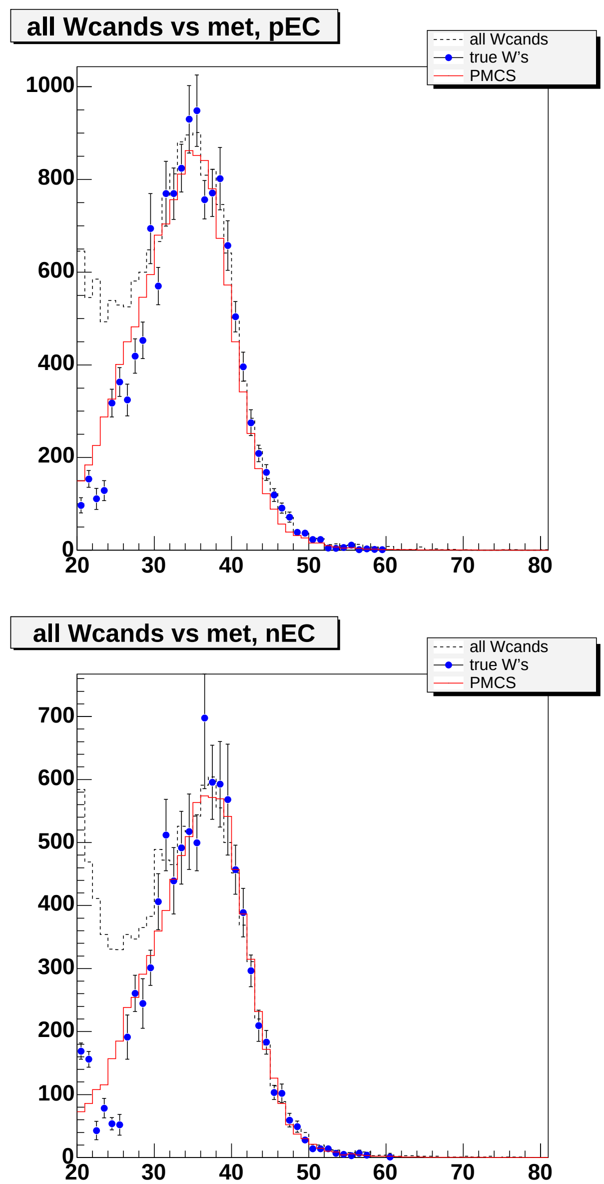

Figure 100: PMCS to data comparison of W background subtracted missing E_T for positive EC (top) and negative EC (bottom). W candidates before background subtraction are represented by the black dashed histogram. The missing E_T cut is extended down to 20 GeV for this plot only in order to ensure reasonable behavior.

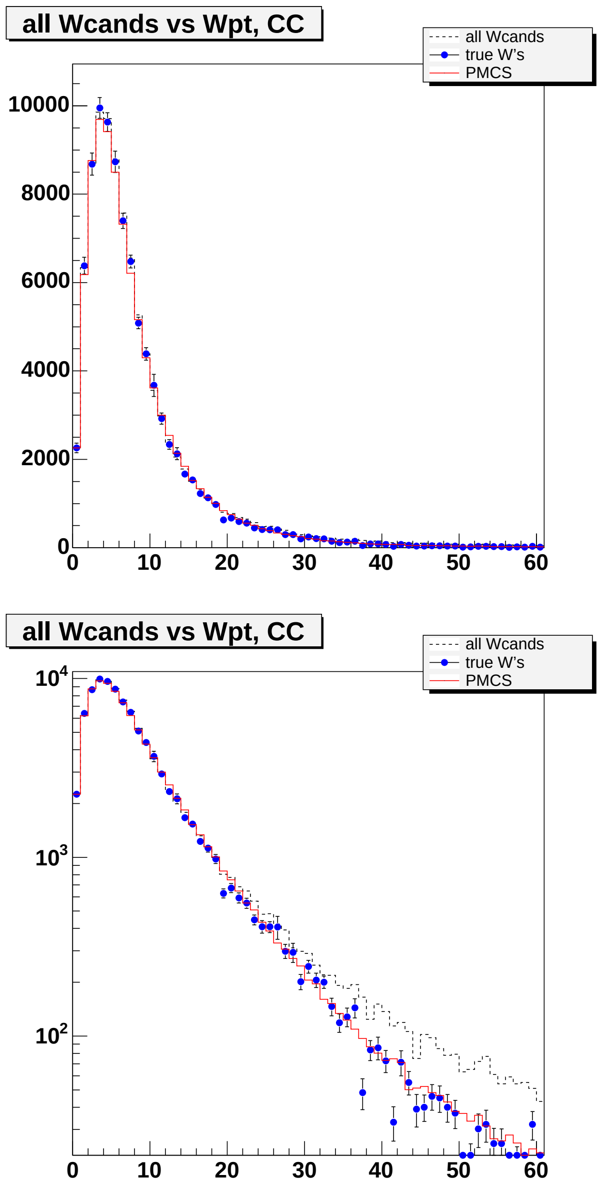

Figure 101: PMCS to data comparison of W background subtracted E_T for CC using a linear scale (top) and log scale (bottom). W candidates before background subtraction are represented by the black dashed histogram.

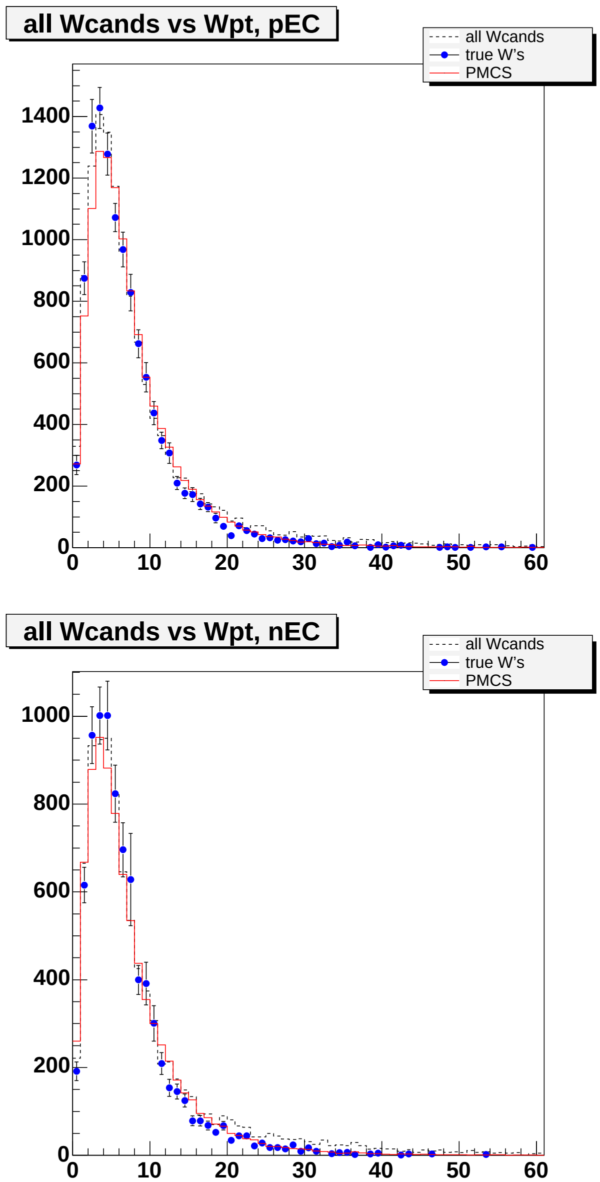

Figure 102: PMCS to data comparison of W background subtracted E_T for positive EC (top) and negative EC (bottom). W candidates before background subtraction are represented by the black dashed histogram.

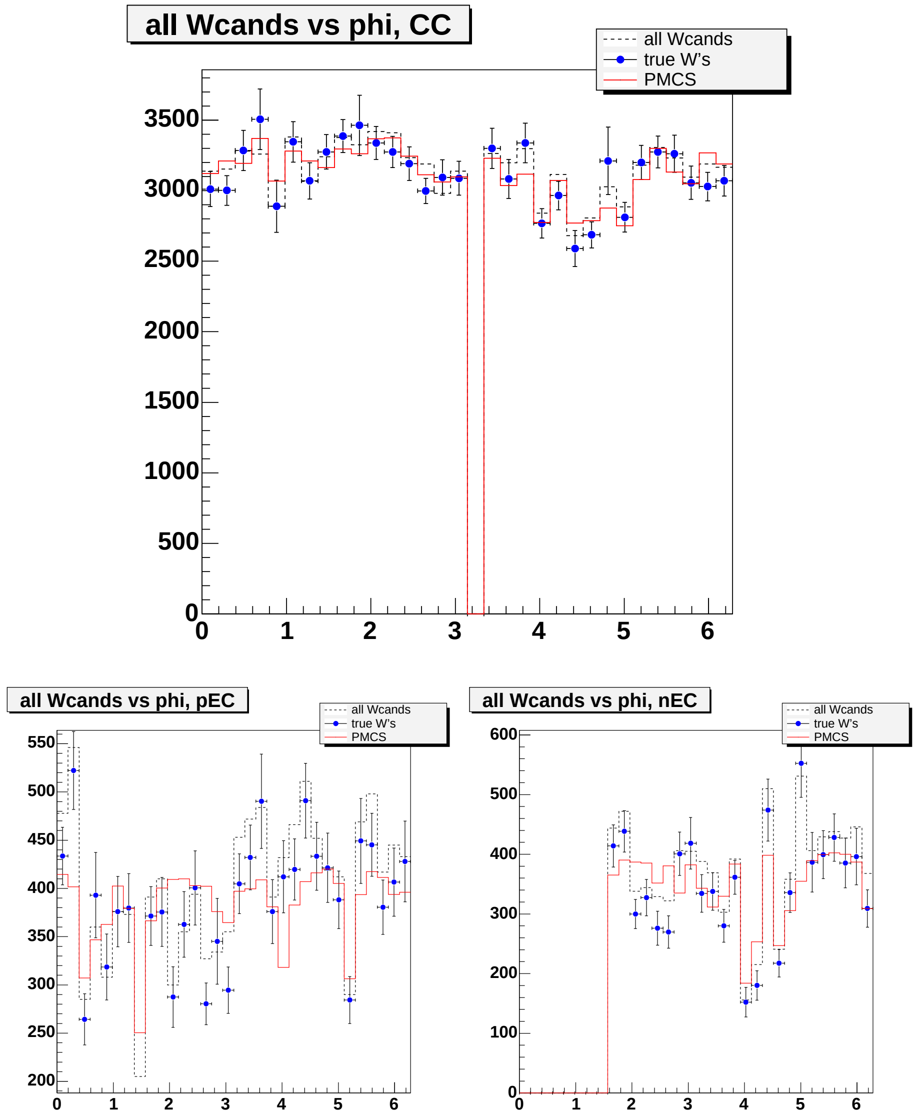

Figure 103: PMCS to data comparison of W background subtracted electron ϕ for CC (top), positive EC (left) and negative EC (right). W candidates before background subtraction are represented by the black dashed histogram.

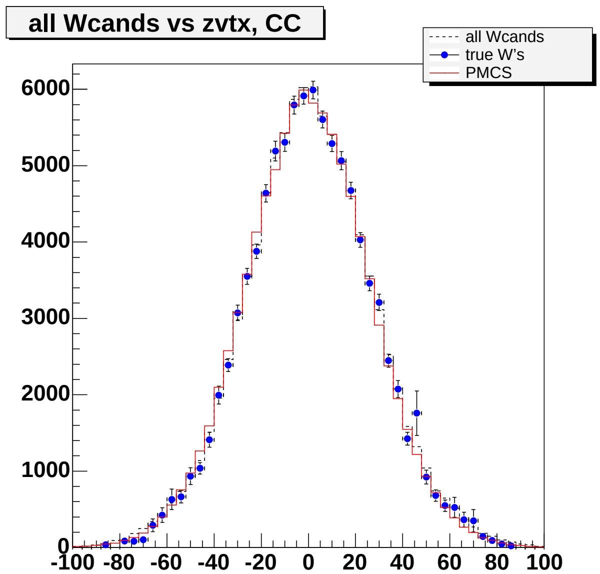

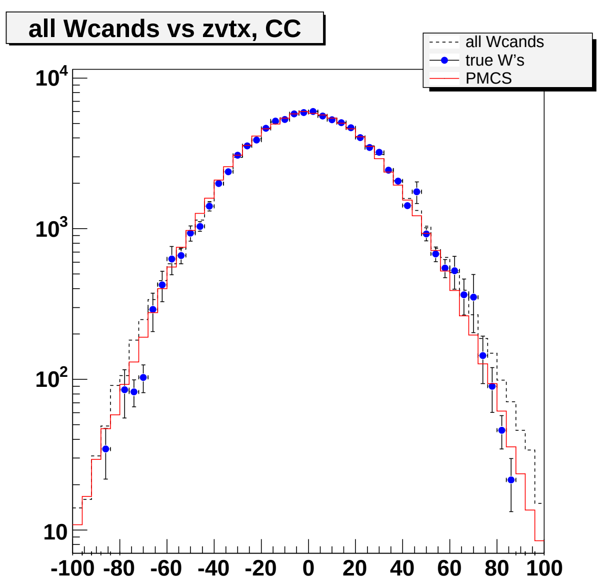

Figure 104: PMCS to data comparison of W background subtracted primary vertex z for CC using a linear scale (top) and log scale (bottom). W candidates before background subtraction are represented by the black dashed histogram.

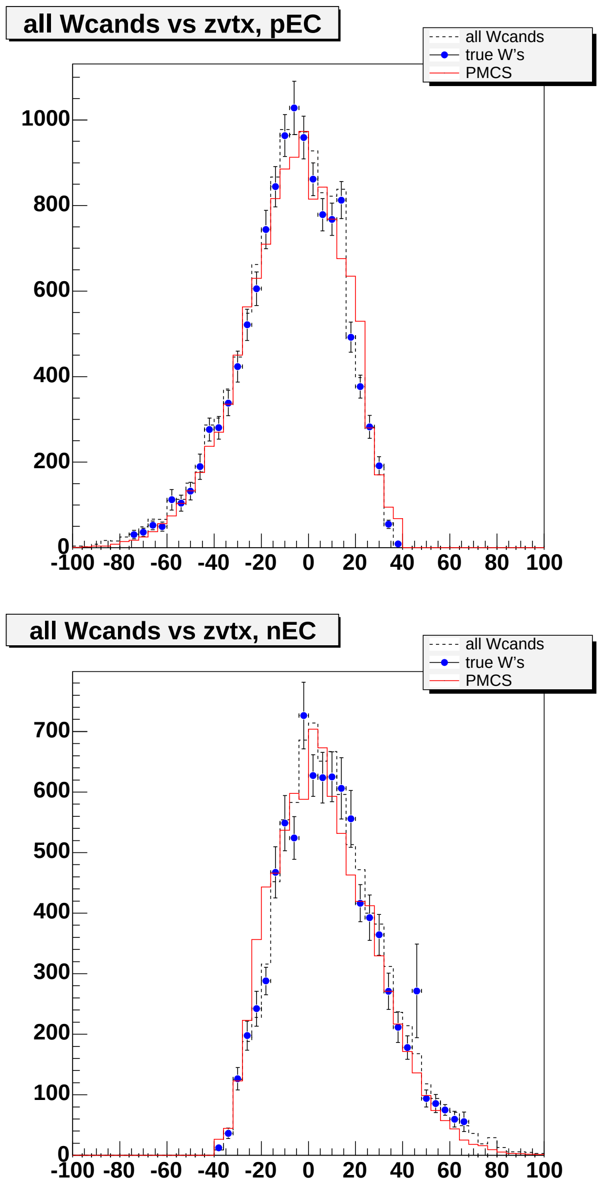

Figure 105: PMCS to data comparison of W background subtracted primary vertex z for positive EC (top) and negative EC (bottom). W candidates before background subtraction are represented by the black dashed histogram.

6.5 Uncertainty Estimate

The uncertainty of the MC acceptance value is assumed to arise solely from the uncertainties of the inputs into the MC simulation:

- Positional resolution in η and ϕ (EC only) of the electron, and the phimod shift applied to CC electrons.
- Electron energy scale: slope and offset parameters for the CC and EC calorimeter regions.
- Electron energy resolution for the CC and EC calorimeter regions, which is parameterized in three terms: *constant*, *sampling*, and *noise*. The sampling term is considered a fixed value with no error. The noise term is also considered fixed with no error: its contribution to the energy resolution is very small for the electron energy range in this analysis. Therefore only the uncertainty on the constant term affects the uncertainty on the acceptance value.
- Hadronic energy scale: slope and offset parameters. Only the slope parameter is considered in the uncertainty estimate. As discussed in Section 6.1.6, the offset parameter (and its error) is very close to zero, so it has been set to zero and is considered to have no error.
- Hadronic energy resolution, which is parameterized in three terms: *constant*, *sampling*, and *noise*. The noise term is small relative to the others, and is considered fixed (at zero) with no error.
- Underlying Event
- Electron preselection, electron track-match, electron ID, and electron trigger efficiencies. These have both statistical and systematic uncertainties.
- Parton distribution functions.

6.5.1 Uncertainty from the Smearing Parameters

For the case of the smearing parameters, the uncertainty on the acceptance value due to the uncertainty of each parameter is estimated by independently varying each parameter up and down by one sigma of its estimated uncertainty and noting the effect on the resulting acceptance value. Results are shown in table 8.

By varying the parameters independently, any correlations between parameters have been ignored. Significant correlation is expected only between the electron energy scale slope and offset parameters. Due to the method used to determine these parameters (see Section 6.1), the magnitude of the correlation is difficult to determine. Therefore, to avoid underestimating this source of uncertainty, these two parameters are considered fully correlated and added linearly together before being added in quadrature with the other results. For each parameter tested, the largest shift in the result between the up and down checks is taken to be the symmetric uncertainty which is used to find the total uncertainty estimate shown in the last row of table 8.

Phimod Shift

The uncertainty on the final cross section due to the uncertainty of the phimod shift (section 6.1.5) is handled separately from the other input parameters. It is estimated by varying the phi-fiducial cut in both data and PMCS by the phi resolution, and noting the variation in the cross section. However, the cut cannot be made looser, since this would accept electrons for which the energy scale is not well measured. Therefore, the cut is only made tighter, and the resulting uncertainty estimate assumed to be symmetric. The result is shown in Table 8.

6.5.2 Statistical Uncertainty of the Efficiencies

The uncertainty on the acceptance value due to the statistical uncertainties of the electron preselection, ID, track-match and trigger efficiencies is determined by calculating the acceptance value many times, each time with a different set of input efficiency distributions. Each set of input efficiency distributions is determined by simultaneously varying each nominal efficiency value by a gaussian distribution of size equal to the value of the statistical error. The resulting acceptance values using 500 trials over the entire W and Z samples are shown in figure 106. These are fit to gaussian distributions with the widths (one standard deviation) determining the uncertainty on the nominal acceptance values. The results are 0.60%, 0.59%, and 0.45% for the W, Z, and R acceptance, respectively.

6.5.3 Systematic Uncertainty of the Efficiencies

Systematic uncertainties on the cross sections due to efficiencies are found by running separate trials in PMCS increasing(+) and decreasing(-) each efficiency by the systematic error. The uncertainty is conservatively assumed to be symmetric with the larger error used. Since the cross section is inversely proportional to acceptance, shifting the efficiency up is expected to increase acceptances and therefore lower the cross sections. Symmetric errors are summarized in in table 9.

Electron Preselection Efficiency

As described in section 4.1, there is an approximate 0.7% relative uncertainty on the electron preselection efficiency which will enter once in the W acceptance and twice in the Z acceptance. Uncertainties for Z (CC-CC + CC-EC) are -0.74%(+) and +1.22%(-) and for W are -0.52%(+) and +0.77%(-).

% change in acceptance

	Z/γ^*			W	R
PMCS parameters	CC-CC	CCEC	both	CC	CC/both
Phimod Shift	+0.71	+0.57	+0.64	+0.92	+0.28
EC Position Res ϕ (up)	N/A	+0.04	+0.01	N/A	-0.04
EC Position Res ϕ (down)	N/A	-0.28	-0.10	N/A	+0.10
CC Position Res η (up)	-0.07	+0.12	-0.01	+0.02	+0.02
CC Position Res η (down)	+0.24	-0.21	+0.08	+0.01	-0.07
EC Position Res η (up)	N/A	-0.26	-0.04	N/A	+0.04
EC Position Res η (down)	N/A	-0.12	-0.09	N/A	+0.09
CC EM-Scale Slope (up)	+0.17	+0.29	+0.21	+0.27	+0.05
CC EM-Scale Slope (down)	-0.13	-0.24	-0.17	-0.28	-0.12
EC EM-Scale Slope (up)	N/A	+0.63	+0.22	N/A	-0.22
EC EM-Scale Slope (down)	N/A	-0.56	-0.20	N/A	+0.20
CC EM-Scale Offset (up)	-0.04	+0.01	-0.02	+0.25	+0.28
CC EM-Scale Offset (down)	+0.09	-0.07	+0.03	-0.03	-0.06
EC EM-Scale Offset (up)	N/A	+0.53	+0.19	N/A	-0.19
EC EM-Scale Offset (down)	N/A	-0.25	-0.09	N/A	+0.09
CC EM Resolution (up)	+0.01	-0.06	-0.01	-0.06	-0.04
CC EM Resolution (down)	+0.09	-0.05	+0.04	+0.09	+0.05
EC EM Resolution (up)	N/A	-0.20	-0.07	N/A	+0.07
EC EM Resolution (down)	N/A	-0.06	-0.02	N/A	+0.02
FSR Radius (up)	+0.26	+0.40	+0.31	+0.09	-0.22
FSR Radius (down)	-0.25	-0.59	-0.37	-0.20	+0.17
Had. E-Scale Slope (up)	N/A	N/A	N/A	-0.13	-0.13
Had. E-Scale Slope (down)	N/A	N/A	N/A	+0.33	+0.33
Had E-Res Constant (up)	N/A	N/A	N/A	+0.03	+0.03
Had E-Res Constant (down)	N/A	N/A	N/A	+0.16	+0.16
Had E-Res Sampling (up)	N/A	N/A	N/A	+0.05	+0.05
Had E-Res Sampling (down)	N/A	N/A	N/A	-0.09	-0.09
CC $u_{\parallel}$ (up)	N/A	N/A	N/A	+0.06	+0.06
CC $u_{\parallel}$ (down)	N/A	N/A	N/A	+0.01	+0.01
Underlying Event (up)	N/A	N/A	N/A	+0.01	+0.01
Underlying Event (down)	N/A	N/A	N/A	-0.02	-0.02
Total PMCS Uncertainty	0.83	1.49	0.88	1.15	0.78

Table 8: Relative uncertainty on the MC acceptance value due to uncertainties on the inputs of the MC simulation.

	Relative Uncertainty on W	Relative Uncertainty on Z	Relative Uncertainty on R
Preselection	0.77%	1.22%	0.46%
Trigger	0.38%	0.07%	0.39%
Track Match	0.40%	0.24%	0.19%
Likelihood	0.64%	0.34%	0.35%

Table 9: Relative systematic uncertainty on the cross sections based on systematic error of the given input efficiency.

Trigger Efficiency

The systematic for Z (CC-CC + CC-EC) candidates is found by finding the shift in acceptance when the trigger efficiency probe is not required to have a matched track. This difference is +0.07%. Uncertainties for W are found from differences in the W cross section using CMT 8 to 11 vs CMT 12 triggers and is found to be 0.38%.

Track-Match Efficiency

As described in section 4.2, there is an approximate 0.5% relative uncertainty on the electron track-match efficiency. For the same reason as trigger efficiency, Z uncertainty should be very small and is found to be -0.17%(+) and +0.24%(-) for (CC-CC + CC-EC). Uncertainties for W are -0.37%(+) and +0.40%(-).

Electron Likelihood Efficiency

As described in section 4.4, there is an approximate 0.5% relative uncertainty on the electron ID efficiency. For the same reason as track-match efficiency, Z uncertainty should be very small and is found to be -0.34%(+) and +0.29%(-) for (CC-CC + CC-EC). Uncertainties for W are -0.63%(+) and +0.64%(-). Since the likelihood cut is only used in W background subtraction it has no affect on acceptance. This uncertainty is on the number of W events after background subtraction.

6.6 PDF Uncertainty

The CTEQ6.1 PDF set includes 20 pairs of error PDFs, that can be used to determine the uncertainty of an observable quantity due to the uncertainty of the default PDF. These error PDFs were not available for Resbos so Pythia is used in the PDF uncertainty calculations. Each pair of error PDFs tests one of twenty free parameters. The effect is recorded for the observable, X , when the parameter is displaced 'up' (S^+) and 'down' (S^-) by its uncertainty. Following the prescription given by the CTEQ collaboration [9, 10]:

	X_{-}	X_{+}
$W \to e\nu$ (CC)	0.97%	1.91%
$Z/\gamma^{*} \to ee$ (CC-CC + CC-EC)	1.22%	1.48%
$R(W(CC)/Z/\gamma^{*}$ (CC-CC + CC-EC))	0.70%	1.12%
$R_{\sigma}(\ \sigma(Z)/\sigma(Z/\gamma^{*})\ )$	0.28%	0.23%

Table 10: Relative PDF uncertainty on the cross sections.

$$\Delta X_{\pm} = \left(\sum_{i}^{pairs} [X(S_i^{\pm}) - X(S_0)]^2 \right)^{1/2} \tag{16}$$

where the uncertainty on an observable X is ΔX, the sum runs over the pairs of PDFs, and $X(S_i^{\pm})$ are the values of X determined using the PDF pairs $S_i^{\pm}$.

PDF uncertainties for W and Z/γ^{*} cross sections and the ratio, R(W/($Z/\gamma*$), are found by replacing X in the equation above by the corresponding acceptances. R_{σ}, the Drell Yan correction factor, is found in a similiar manner using the ratio of pure Z to Z/γ^{*} cross sections. Calculations are made with 2 million events generated using Pythia and the CTEQ6.1 NLO pdf set for the default and each of the 20 pairs of error PDF's for W, Z/γ^{*} and pure Z. The resulting uncertainties are shown in Table 10. R_{σ} uncertainty is small and for simplicity is set to $\pm 0.28\%$ which contributes an uncertainty of 0.30% to the cross sections.

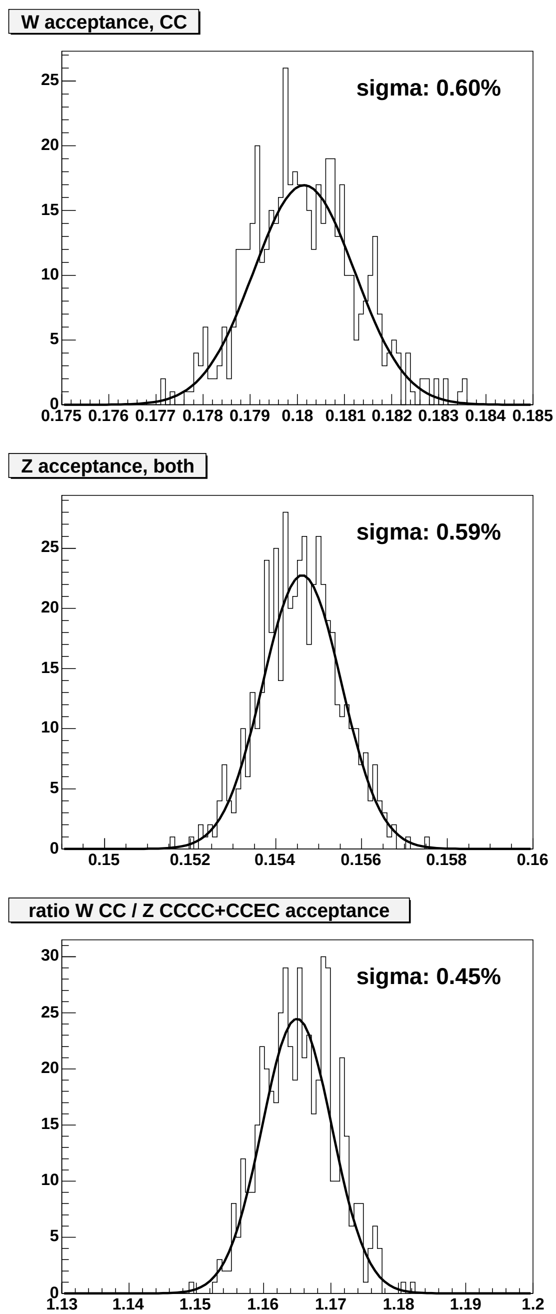

Figure 106: The distribution of acceptance values produced by PMCS that results from simultaneously varying the input efficiency values by their statistical error.

7 Results

7.1 Input Parameters

The mean values of the input parameters for the Z cross section calculation are summarized in table 11.

	Total	CC-CC	CC-EC
N_Z	7793	5068	2725
A_{Z/γ^*}	0.15678	0.10161	0.05518
R_σ		0.9547	
$\mathcal{L}$ (pb^{-1})		177.3	

Table 11: Summary of input parameters to the $Z \to ee$ cross section results

The mean values of the input parameters for the W cross section calculation are summarized in table 12.

	CC
N_W	96799
A_W	0.18254
f_Z^W (%)	0.26
f_τ^W (%)	1.80
$\mathcal{L}$ (pb^{-1})	177.3

Table 12: Summary of input parameters to the $W \to e\nu$ cross section result

7.2 Cross Section Calculation

The W and Z cross sections time branching ratios are finally calculated using

$$\sigma_{Z/\gamma^*} \times B(Z/\gamma^* \to e^+e^-) = \frac{N_Z}{\mathcal{L}} \frac{1}{A_{Z/\gamma^*}}$$
$$\sigma_Z \times B(Z \to e^+e^-) = \sigma_{Z/\gamma^*} \times B(Z/\gamma^* \to e^+e^-) \quad R_\sigma$$
$$\sigma_W \times B(W \to e^\pm \overset{(-)}{\nu}) = \frac{N_W}{\mathcal{L}} \frac{1}{A_W}(1 - f_\tau^W - f_Z^W)$$
$$R = \frac{\sigma_W \times B(W \to e^\pm \overset{(-)}{\nu})}{\sigma_Z \times B(Z \to e^+e^-)} = \frac{N_W}{N_Z} \frac{A_{Z/\gamma^*}}{A_W} \frac{1 - f_\tau^W - f_Z^W}{R_\sigma}$$

where N_Z and N_W are the number of Z and W events after QCD background subtraction. $\mathcal{L}$ is the integrated luminosity for the data sample. R_σ is the Drell-Yan correction factor for $Z \to ee$ events, f_τ^W is the fraction of $W \to \tau\nu$ events that pass the $W \to e\nu$ selection criteria and f_Z^W is the fraction of Z boson events misidentified as W bosons. A_Z/γ^* and A_W are the acceptances for Z/γ^* and W events found from the Monte Carlo. These acceptance values include the trigger efficiency for EM objects, the EM preselection efficiency (cluster finding, EM fraction and isolation), track matching efficiency, and electron likelihood efficiency.

Using values summarized in tables 11 and 12, the following results are calculated:

The physical Z/γ^* cross section within the mass range 50 to 130 GeV is:

$\sigma_{Z/\gamma^*} \times B(Z/\gamma^* \rightarrow e^+e^-) =$
(CC-CC): 281.3 ± 3.9 $(stat)$ pb
(CC-EC): 278.5 ± 5.3 $(stat)$ pb
Combined:
280.4 ± 3.1 $(stat) \pm 1.7$ $(sys\_stat) \pm 4.7$ (sys) $^{+\mathbf{4.1}}_{-\mathbf{3.4}}$ $(pdf) \pm 18.2$ $(lumi)$ pb

Multiplying by R_σ yields the pure Z cross section for all masses:

$\sigma_Z \times B(Z \rightarrow e^+e^-) =$
(CC-CC): 268.6 ± 3.7 $(stat)$ pb
(CC-EC): 265.9 ± 5.1 $(stat)$ pb
Combined:
267.7 ± 3.0 $(stat) \pm 1.6$ $(sys\_stat) \pm 4.5$ (sys) $^{+\mathbf{4.0}}_{-\mathbf{3.3}}$ $(pdf) \pm 17.4$ $(lumi)$ pb

The W (CC) cross section is:

$\sigma_W \times B(W \rightarrow e^\pm \overset{(-)}{\nu}) =$
2929 ± 9 $(stat) \pm 30$ $(sys\_stat) \pm 49$ (sys) $^{+\mathbf{56}}_{-\mathbf{28}}$ $(pdf) \pm 190$ $(lumi)$ pb

and the ratio, W(CC)/Z(CC-CC + CC-EC), of the cross sections is:

$R = \frac{\sigma_W \times B(W \rightarrow e^\pm \overset{(-)}{\nu})}{\sigma_Z \times B(Z \rightarrow e^+e^-)} =$
10.94 ± 0.13 $(stat) \pm 0.07$ $(sys\_stat) \pm 0.14$ (sys) $^{+\mathbf{0.12}}_{-\mathbf{0.08}}$ (pdf)

7.3 Uncertainties

The uncertainties on the cross sections and the ratio are summarized in Table 13. The uncertainties are divided into five categories:

stat

This uncertainty results from the statistical uncertainty of the number of W and Z candidate events before any background subtraction.

sys_stat

Stat Error on Efficiencies. This uncertainty results from statistical uncertainty of the measured preselection, track-match, trigger and electron likelihood efficiencies. This uncertainty is directly related to the size of the Z event sample that was used to determine the efficiencies.

For the Z cross section, this uncertainty results from the the uncertainty on the acceptance value due to the statistical uncertainty of the measured preselection, track-match, trigger and electron likelihood efficiencies. Thus the relative uncertainty on the cross section is the same as that on the Z acceptance determined in Section 6.5.2.

For the W cross section, however, the electron likelihood efficiency enters through the matrix method (Section 5.3.2) and not the acceptance. Therefore in this case, the method in Section 6.5.2 is followed, except the quantity N_W/A_W is determined for 500 trials using separate sets of smeared input efficiencies, where N_W the number of W events after matrix method background subtraction and A_W is the W acceptance. The result is shown in Figure 107. The relative uncertainty on the ratio is determined in a similar way by calculating N_W/A_R, where A_R is the ratio of the W and Z acceptances. The result is also shown in Figure 107.

sys

$W \rightarrow \tau\nu$ and $Z \rightarrow ee$ Background A conservative uncertainy of 20% is assigned to the background in the $W \rightarrow e\nu$ sample from the $W \rightarrow \tau\nu$ and $Z \rightarrow ee$ backgrounds.

Drell Yan Correction The uncertainty arising from the Drell Yan correction is found using the CTEQ6.1M error PDF sets as described in Section 6.6. For Z/γ^*, the total systematic does not include Drell Yan correction uncertainty.

Background Subtraction. The number of Z events and the track-match efficiency calculation rely on the background subtraction technique described in section 5.1.2. Uncertainties are estimated based on χ^2 fit errors, variations with alternate background choices and comparisons to matrix method background subtraction. See section 5.1.2 for more details.

PMCS Parameters. This is the uncertainty on the cross section due to the uncertainty on the input parameters to PMCS, which affect the acceptance values as determined in Section 6.5.1.

Trigger, Preselection, and Track-Match Eff. This is the uncertainty on the cross section due to the systematic uncertainty of the trigger, preselection, and track-match efficiencies, which affect the acceptance values as determined in Section 6.5.3.

Electron Likelihood Eff. This is the uncertainty on the cross section due to the systematic uncertainty of the electron likelihood efficiency determined in Section 4.4. It affects the Z cross section via the acceptance value as determined in Section 6.5.3. It affects the W cross section via the matrix method (Section 5.3.2).

Total sys. All **sys** uncertainties are added in quadrature.

pdf

This uncertainty results from the uncertainty on the acceptance values due the uncertainty on the input parton distribution functions. Described in Section 6.6.

lumi

This uncertainty results from the uncertainty on the integrated luminosity. This value is determined by the luminosity group [15].

Source	Relative Uncertainty (%) on σ_W	σ_Z	R
stat			
Number of Events	0.32	1.12	1.17
sys_stat			
Stat Error on Efficiencies	1.03	0.59	0.66
sys			
$W \to \tau\nu$ and $Z \to ee$ Background	0.36	n/a	0.36
Drell Yan Correction	n/a	0.30	0.30
QCD Background Subtraction	n/a	0.58	0.58
PMCS Parameters	1.15	0.88	0.78
Preselection Eff	0.77	1.22	0.46
Trigger Eff	0.38	0.07	0.39
Track-match Eff	0.40	0.24	0.19
Likelihood Eff	0.64	0.34	0.35
Total **sys**	1.66	1.69	1.30
pdf			
PDF	$^{+1.91}_{-0.97}$	$^{+1.48}_{-1.22}$	$^{+1.12}_{-0.70}$
lumi			
Luminosity	6.5	6.5	n/a

Table 13: Summary of Uncertainties. All values are relative and given in percent.

7.4 σ_W/σ_Z calculation

The ratio of total inclusive W and Z cross sections, σ_W/σ_Z, is calculated using ZWPROD [16] with the CTEQ6.1M PDF set. The result for σ_W/σ_Z is found to be 3.381 ± 0.051. Table 14 summarizes the total uncertainty estimated by varying each input parameter by its uncertainty. This is similiar to the procedure used in combining CDF and DØ indirect width results in Run I [17]. One change to the procedure is that PDF uncertainty is calculated with the CTEQ6.1M PDF error sets using Equation 16.

Input Parameter	σ_W/σ_Z	$\Delta(\sigma_W/\sigma_Z)$
PDF uncertainty		
$\Delta(\sigma_W/\sigma_Z)_-$		-0.022
$\Delta(\sigma_W/\sigma_Z)_+$		$+0.015$
$M_W = 80.425 \pm 0.038$ GeV/c^2		
$M_W = 80.387$ GeV/c^2	3.3831	$+0.002$
$M_W = 80.463$ GeV/c^2	3.3797	-0.002
Factorization Scale (Mean = M_W)		
Factorization Scale = M_W / 2	3.3791	-0.002
Factorization Scale = $M_W \times 2$	3.3823	$+0.001$
Renomalization Scale (Mean = M_W)		
Renormalization Scale = M_W / 2	3.3784	-0.003
Renormalization Scale = $M_W \times 2$	3.3834	$+0.002$
$sin^2_{\theta_W}$ (effective Born approx. = 0.23124)		
$sin^2_{\theta_W}$(on - shell) = 0.22267	3.3357	-0.046
Total symmetric uncertainty = ± 0.051		

Table 14: Summary of major uncertainties on the σ_W/σ_Z calculation found by varying the input parameters by their uncertainties. A symmetric total uncertainty is obtained by combining in quadrature the largest $\Delta(\sigma_W/\sigma_Z)$ for each input parameter

7.5 $Br(W \to e\nu)$ and Γ_W

Based on our measurement of R given in Section 7.2 and external Standard Model based inputs, indirect results for the W leptonic branching ratio, $Br(W \to e\nu)$, and W total width, Γ_W, are extracted based on

$$R \equiv \frac{\sigma(p\bar{p} \to W + X) \times Br(W \to e\nu)}{\sigma(p\bar{p} \to Z + X) \times Br(Z \to ee)} = \frac{\sigma_W}{\sigma_Z} \times \frac{Br(W \to e\nu)}{Br(Z \to ee)}. \tag{17}$$

Solving for $Br(Z \to ee)$ and Γ_W yields

$$Br(W \to e\nu) = R \times \frac{[Br(Z \to ee)]}{[\sigma_W/\sigma_Z]} \tag{18}$$

and

$$\Gamma_W \equiv \frac{[\Gamma(W \to e\nu)]}{Br(W \to e\nu)} \quad = \quad \frac{1}{R} \times \frac{[\Gamma(W \to e\nu)] \times [\sigma_W/\sigma_Z]}{[Br(Z \to ee)]} \tag{19}$$

where the externally determined parameters, based on Standard Model predictions, are

$Br(Z \to ee) = (3.3655 \pm 0.0022)\%$ [18]

$\sigma_W/\sigma_Z = 3.381 \pm 0.051$ (Section 7.4), and

$\Gamma(W \to e\nu) = 0.22656 \pm 0.00024$ GeV [18].

The results are

$$B(W \to e\nu) = (10.89 \pm 0.13\ (stat) \pm 0.07\ (sys\_stat) \pm 0.14\ (sys)\ {}^{+\mathbf{0.12}}_{-\mathbf{0.08}}\ (pdf) \pm 0.16\ (ext)\ )\%$$

and
$$\Gamma_W = 2.080 \pm 0.024\ (stat) \pm 0.014\ (sys\_stat) \pm 0.027\ (sys)\ {}^{+\mathbf{0.023}}_{-\mathbf{0.015}}\ (pdf) \pm 0.031\ (ext)\ \mathrm{GeV}$$

where the last source of uncertainty comes from the external parameters. Results are in good agreement with the Standard Model predictions [18]:

(SM) $Br(W \to e\nu) = (10.822 \pm 0.016)\%$ and
(SM) $\Gamma_W = 2.0936 \pm 0.0022$ GeV,

and are also consistent with the world averages [19]:

(WA) $Br(W \to e\nu) = (10.72 \pm 0.16)\%$ and
(WA) $\Gamma_W = 2.124 \pm 0.041$ GeV.

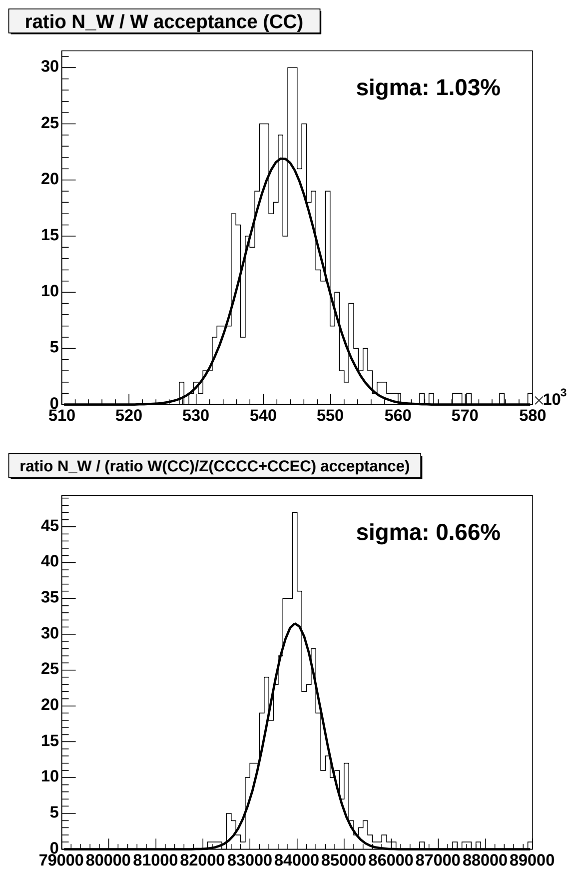

Figure 107: The distribution of N_W/A_W and N_W/A_R values produced by PMCS and the matrix method that results from simultaneously varying the input efficiency values by their statistical error.

8 Cross Checks

8.1 Efficiency method checks using full Monte Carlo simulation

To check out methods for determining efficiency we use 247000 Z/γ events using the full monte carlo simulation with reco version p14.06.00 and d0correct p1405. Our methods for calculating efficiency of a cut using the tag and probe method are applied in exactly the same manner as for data and compared to the actual number of generated electrons which pass the same cut.

Shown in figure 108 is a comparison for our track matching efficiency method divided in bins of primary vertex z, see section 4.2. In bins of z vertex, agreement is quite good. Plotting tracking efficiency as a function of deteta only, shown in figure 109, shows a measured efficiency greater than the actual value for EC. This is due to the bias caused by the tag and probe sharing the same primary vertex and illustrates one reason why z vertex binning is important.

Figure 110 shows good agreement for our likelihood efficiency method divided in bins of primary vertex z, see section 4.4. Likelihood efficiency as a function of deteta only, shown in figure 111, shows no bias in our method for either CC or EC, but primary vertex bins are still used since likelihood efficiency is applied after tracking efficiency.

Figures 112 and 113 are comparisons for preselection efficiency vs. $\eta_{\mathrm{d}et}$ and phimod. This monte carlo suggests a small dependence on the presence of a track with $p_T > 27GeV$ as indicated by the blue dashed line in the figures. The actual efficiency drops off in the bins (-1.05,1.00) and (1.00,1.05) much more than with our preselection efficiency method. The cause of this disagreement appears to be from the necessity of having a tight electron as a tag. If at least one tight electron is required in an event, these drops disappear. With this requirement, the efficiency as seen in figure 114 is consistent with our method although biased slightly higher due to the tight electron requirement.

8.2 Consistency of matrix method and peak fit background subtraction using Z events

Z events are used to check the consistency of the matrix method with the peak fit method where data are fitted to a signal and background shape. Events are chosen with 2 EM objects passing preselection cuts and invariant mass between 70 and 110 GeV. Both EM objects are considered as possible probes for each event with the other EM object taking on a role similiar to missing E_T in the W sample. Probe samples are selected using nominal loose and tight electron cuts with the loose sample requiring a track with $P(\chi^2) > 0.01$ and the tight sample adding electron likelihood > 0.9. The matrix and peak fit methods are found to agree quite well. See table 15 for results and figure 115 for peak fit plots.

	total probes	after background subtraction	background percentage
loose probes, peak fit	9139	8756 ± 98	4.2 ± 0.3
loose probes, matrix	9139	8771 ± 116	4.0 ± 1.3
tight probes, peak fit	7893	7801 ± 91	1.2 ± 0.3
tight probes, matrix	7893	7828 ± 94	0.8 ± 1.2

Table 15: Comparison of Z probe sample background subtraction using the matrix and peak fit methods.

	loose W cand background
nominal	1.0 ± 0.7%
likelihood > 0.5	1.3 ± 0.6%
hm7 < 12	1.4 ± 1.5%
hm7 < 16	0.2 ± 1.1%
iso < 0.08, EMfrac > 0.97	2.1 ± 0.9%
track $P(\chi^2) > 0$	0.6 ± 0.9%

Table 16: W background checks using nominal method

8.3 W QCD background checks

Checks are made on the W QCD background by varying definitions for 'loose' and 'tight' cuts placed on the W candidate and fake samples when applying the matrix method described in section 5.3.2. The nominal 'loose' and 'tight' sample requirements are given in section 3.5 with the difference being the addition of the electron likelihood > 0.9 cut in the tight sample. The first four checks change the cut added in the tight sample. For the first test, the electron likelihood > 0.9 cut is replaced by electron likelihood > 0.5, for the second Hmatrix7 < 12, for the third Hmatrix7 < 16 and for the fourth Isolation < 0.08 and EMFraction > 0.97. In the last check the loose sample uses a relaxed track requirement with $P(\chi^2) > 0$ and the nominal loose sample, with track $P(\chi^2) > 0.01$, becomes the tight sample. Table 16 compares the resulting background percentages on the nominal loose W candidate sample.

8.4 W background with single EM fake sample

An alternative fake sample is created by removing the requirement of a jet opposite the fake electron. Doing this removes any possible bias from this requirement, however more signal is allowed into the fake sample which is at least partially responsible for an increased fake rate compared to the nominal method with an opposite jet. This signal is evident by the peak at around 40 GeV in the single EM fake rate vs. E_T plot shown in figure 116 but not in

	loose W cand background (using single EM)
nominal	0.8 ± 0.9%
likelihood > 0.5	1.4 ± 0.6%
hm7 < 12	1.6 ± 1.7%
hm7 < 16	-1 ± 5%
iso < 0.08, EMfrac > 0.97	2.3 ± 1.1%
track $P(\chi^2) > 0$	1.6 ± 0.7%

Table 17: W background checks using single EM

	background
nominal(3D track, no hmatrix)	1.0 ± 0.7%
Run I	4.6 ± 1.4%
spatial track, hmatrix7 < 12	1.9 ± 0.7%
spatial track, hmatrix7 < 16	3.0 ± 0.7%
no track, hmatrix 7 < 12	47.9 ± 0.5%

Table 18: W background comparison to Run I

the nominal plot. One nice feature of this fake sample is a flat fake rate as a function of MET below 10 GeV, see figure 117. Given the increased signal, this method is a good estimate for an upper bound on systematic uncertainty on the fake rate and its effect on background percentage is negligible at -0.2% for the nominal method. W QCD background percentages are found using the same cuts for 'loose' and 'tight' samples in section 8.3. See table 17 for results.

8.5 W background comparison to Run I

The background in the Run I W sample was found to be 4.6±1.4% in the central region which is much larger than found here. The main differences in the Run I candidate sample are the addition of an hmatrix cut and the use of a spatial only track match. In order to get an idea of why our background percentage, 1.0 ± 0.7% , is so much smaller, cuts simliar to Run I are tested on our data. As table 18 shows, the background percentage is extremely sensitive to the quality of the track match. Background increases when switching from a 3D track with an E_T/P_T cut to spatial only even when an hmatrix cut is included and jumps to nearly 50% without a track requirement. Reduced background in Run II can be easily explained by improvements in track matching.

8.6 Stability checks

The following checks are made to ensure the stability of the cross sections as a function of measurement method or fiducial region. See figure 19 for a summary of checks made and their effects on the cross sections.

8.6.1 Extended bad calorimeter region cut boundaries

Boxes placed around bad calorimeter cells are extended slightly beyond the cell in order to take into account effects on electrons in neighboring cells. In order to verify that these extensions are large enough, the cross sections were found with the boxes extended an additional cell length, 0.1 in η and ϕ, beyond the nominal cut boundaries. The Z (CCCC) cross section increased by 0.30% and W (CC) decreased by 0.36%. These differences are small enough to be explained by the loss in stats of 29.5% for Z (CCCC) and 16.2% for W (CC) with the extended cuts.

8.6.2 Primary vertex binning choice

The number of primary vertex z bins used is limited by statistics, especially at high vertex z where the greatest track match efficiency dependence is. To check that the number of vertex z bins is adequate, the cross sections are found using two alternate primary vertex bin sets. The first set has five bins: $<$ -39, -39 to -10, -10 to 10, 10 to 39 and $>$ 39 cm, and the second has six bins: $<$ -30, -30 to -10, -10 to 0, 0 to 10, 10 to 30, and $>$ 30 cm. Agreement is very good with all three vertex bin sets. Compared to the nominal binning, the Z (CCCC) cross section decreases by 0.04% using the first set and 0.15% using the second. For the W (CC) cross section, the result decreases by 0.19% for the first set and 0.26% for the second.

8.6.3 Run number, η_{det} and ϕ_{det}

Figure 118 shows the W cross section as a function of run number, η_{det} and ϕ_{det} using small bins and including only statistical errors in the error bars. For figure 119, W cross sections are found with the detector split in half in η_{det} and ϕ_{det}. In this case error bars include all errors except luminosity in order to check that both halves are consistent with each other.

8.6.4 Inclusion of CC phi module 17

Phi module 17, extending the length of the central calorimeter in η and from $1/2\pi < \phi_{det} > 17/16\pi$, has an energy response approximately 8% lower than the average. To see if this problem has a large effect on the result, cross sections are found without it removed. Including the phi module results in an increase of statistics of 6.4% for Z (CCCC) and 2.7% for W (CC) with the Z cross section increasing by 0.08% and the W cross section decreasing by 0.47%.

stability check	$\sigma(W)$ change	$\sigma(Z)$ change
extend badcal cut by 0.1	+0.30%	-0.36%
use 5 z vertex bins	-0.04%	-0.19%
use 6 z vertex bins	-0.15%	-0.26%
don't remove phi module 17	-0.47%	+0.08%

Table 19: Stability checks

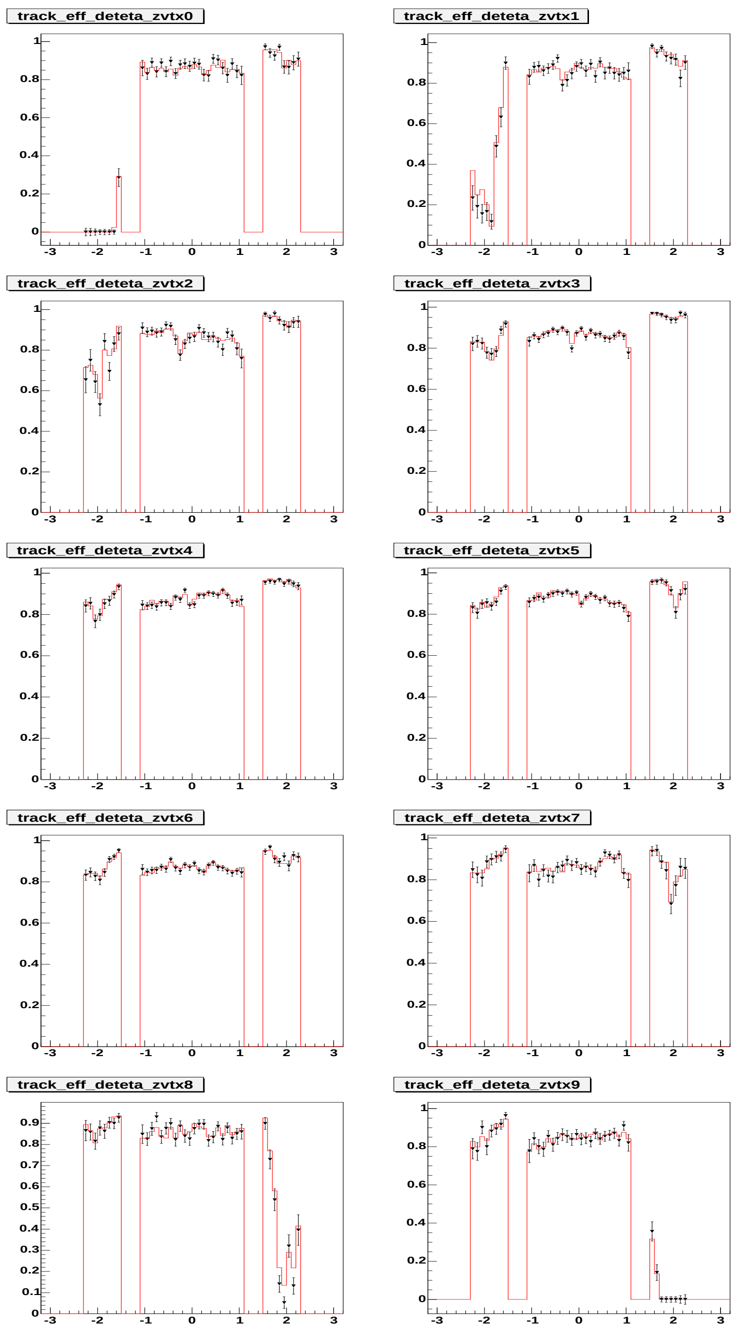

Figure 108: A comparison for track matching efficiency vs η_{det} in primary vertex z bins using the full monte carlo simulation. The points are for the track efficiency tag and probe method and the histograms are actual efficiencies. Z vertex bins are, going left to right from top to bottom: < -39, -39 to -30, -30 to -23, -23 to -10, -10 to 0, 0 to 10, 10 to 23, 23 to 30, 30 to 39, and > 39 cm.

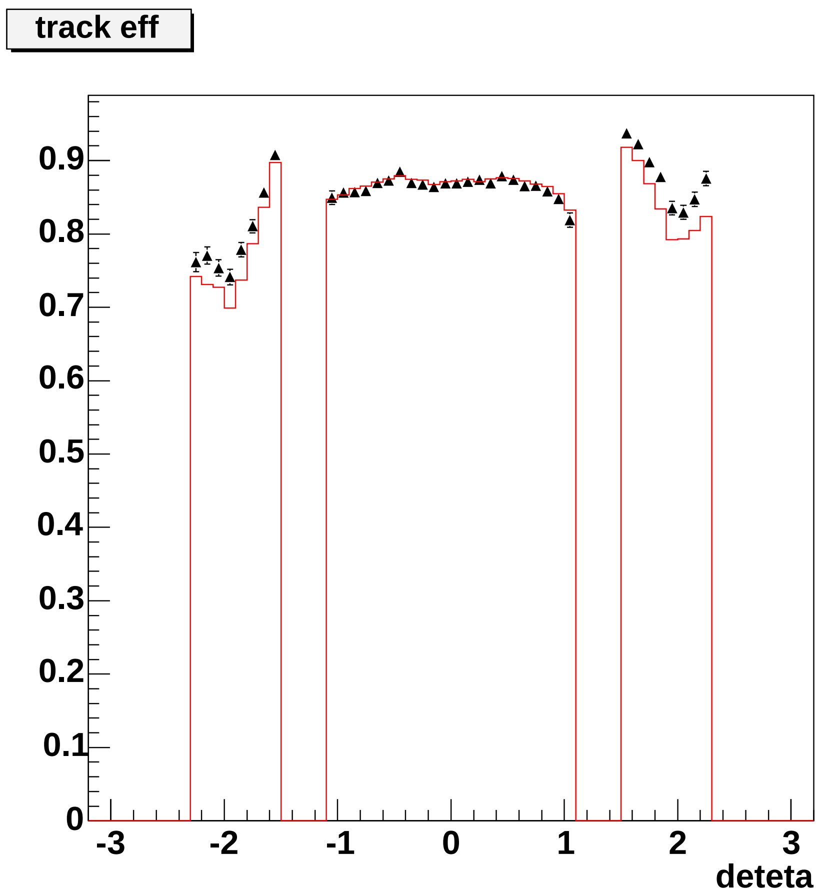

Figure 109: A comparison of track matching efficiency vs η_{det} for all vertex z using the full monte carlo simulation. The points are for the track efficiency tag and probe method and the histogram is actual efficiency. Disagreement in EC is from primary vertex z bias.

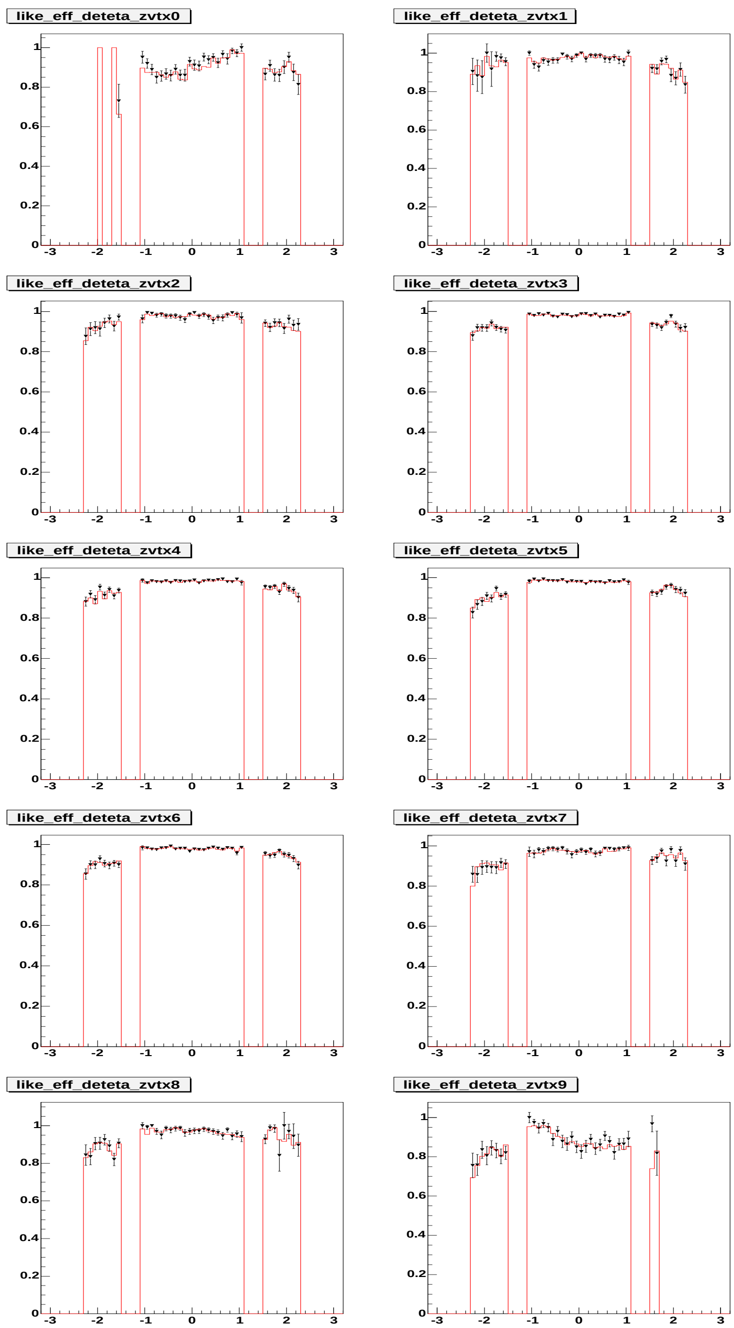

Figure 110: A comparison for likelihood efficiency vs η_{det} in primary vertex z bins using the full monte carlo simulation. The points are for the track efficiency tag and probe method and the histograms are actual efficiencies. Z vertex bins are, going left to right from top to bottom: $<$ -39, -39 to -30, -30 to -23, -23 to -10, -10 to 0, 0 to 10, 10 to 23, 23 to 30, 30 to 39, and $>$ 39 cm.

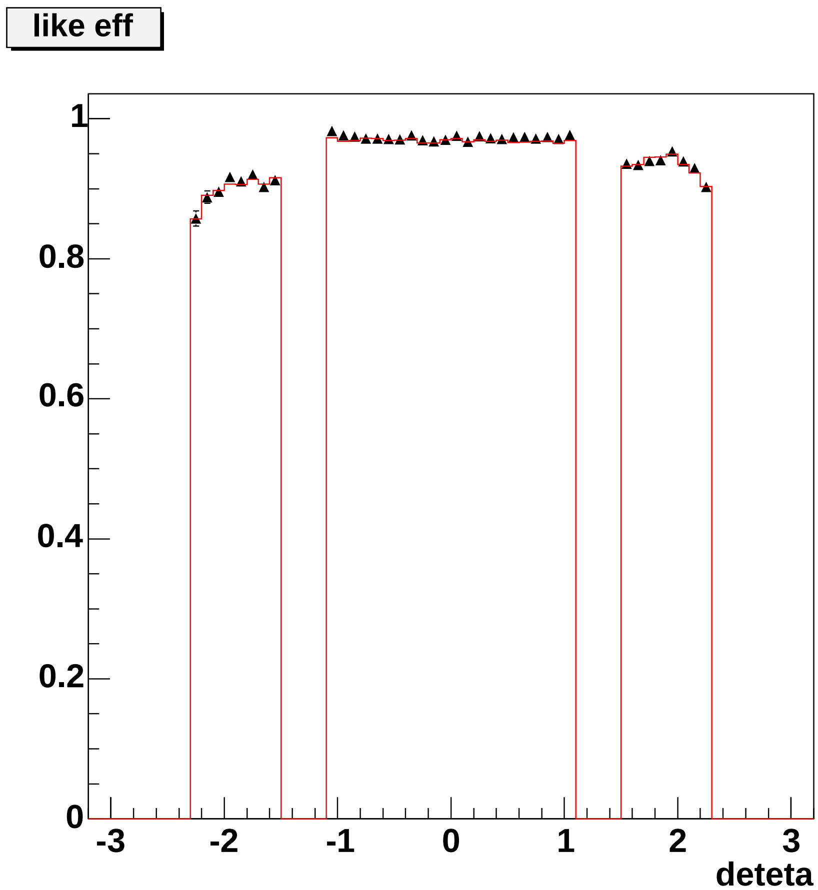

Figure 111: A comparison of likelihood efficiency vs η_{det} for all vertex z using the full monte carlo simulation. The points are for the likelihood efficiency tag and probe method and the histogram is actual efficiency.

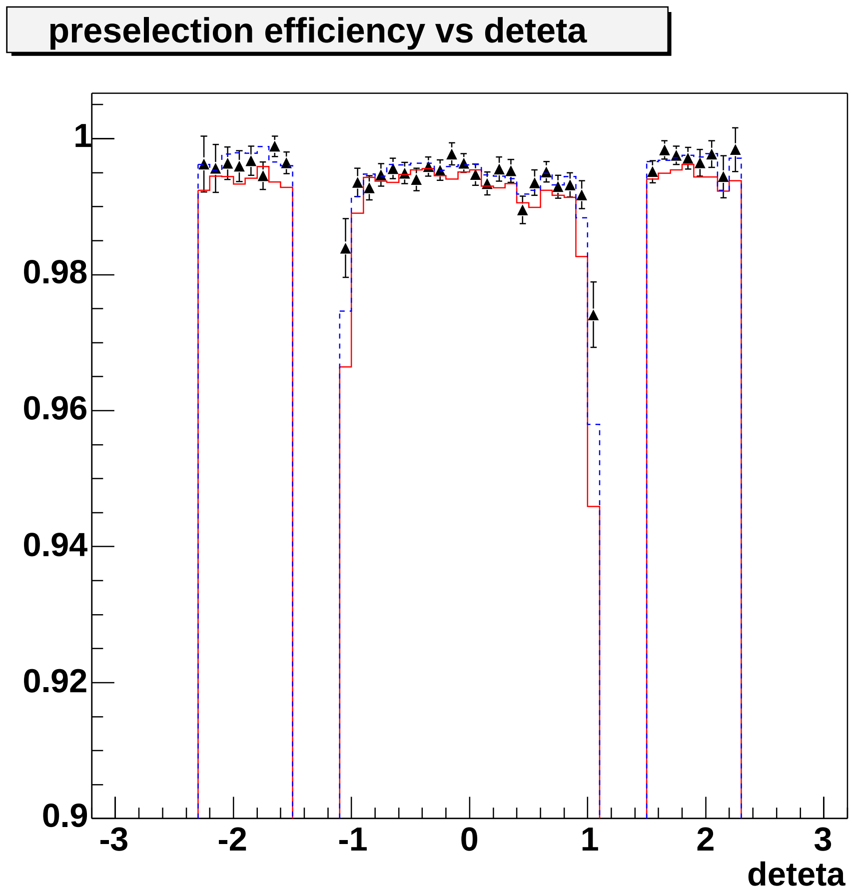

Figure 112: A comparison of preselection efficiency vs η_{det} using the full monte carlo simulation. The points are for the preselection efficiency tag and probe method and the histograms are actual efficiencies. The blue dashed histogram is with a track match with $p_T > 27$ and the red is with no track required.

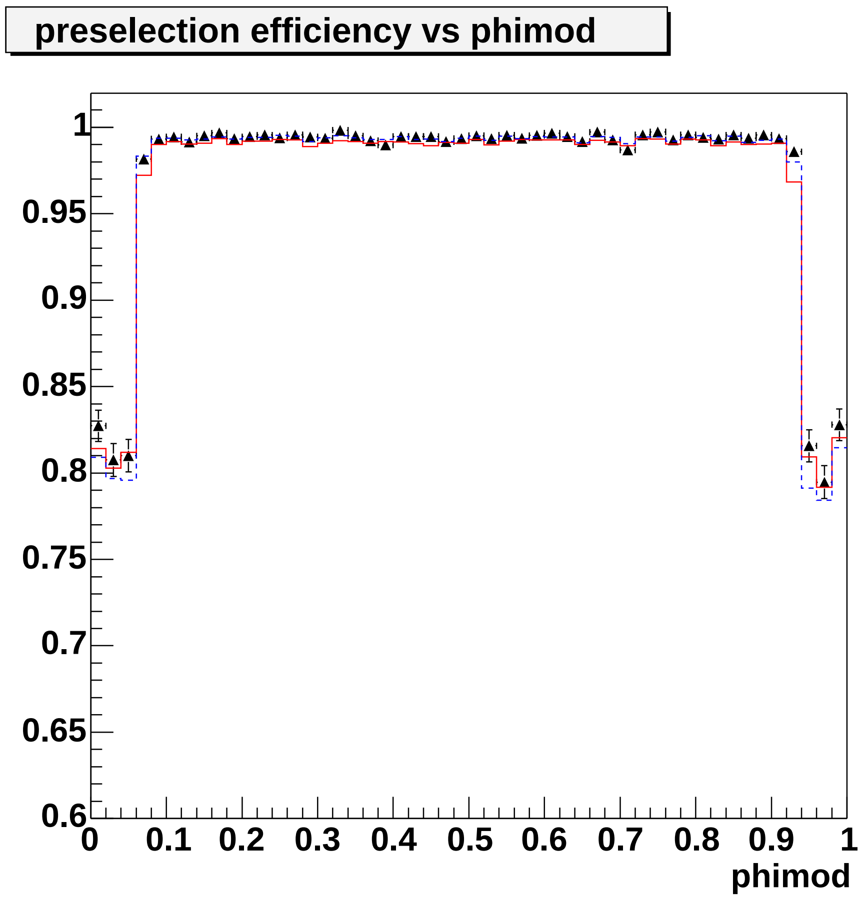

Figure 113: A comparison of preselection efficiency vs phimod using the full monte carlo simulation. The points are for the preselection efficiency tag and probe method and the histograms are actual efficiencies. The blue dashed histogram is with a track match with $p_T > 27$ and the red is with no track required.

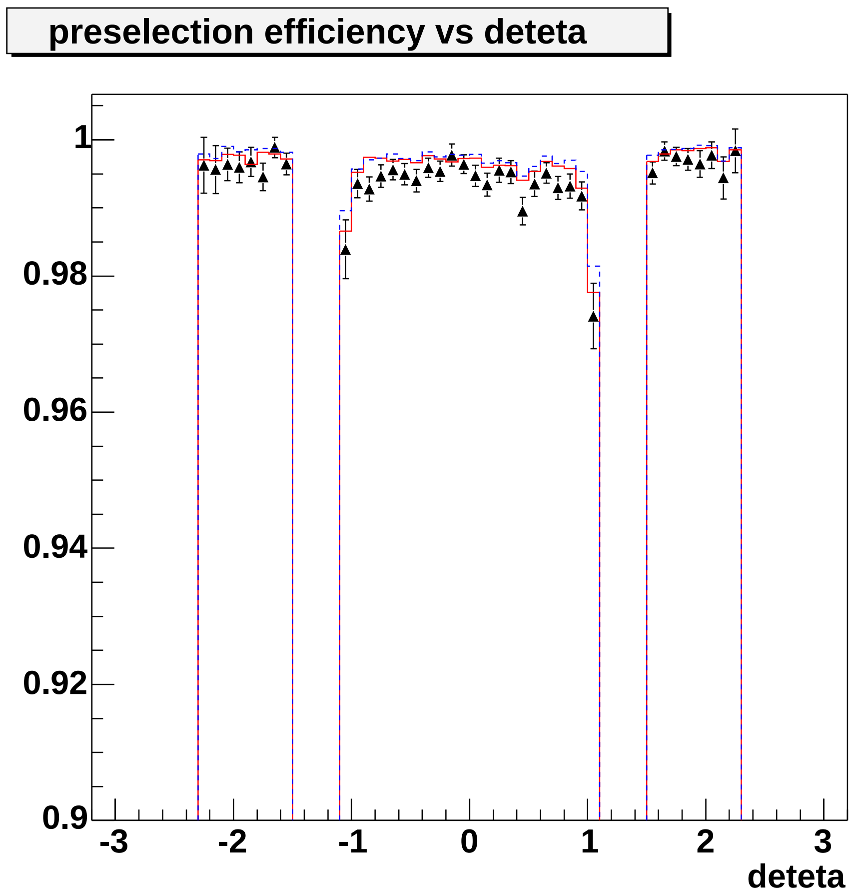

Figure 114: A comparison of preselection efficiency vs η_{det} using the full monte carlo simulation. The points are for the preselection efficiency tag and probe method and the histogram is actual efficiency with at least one tight electron per event. The better agreement at high CC η_{det} suggests the tag and probe method is biased by the requirement of a tight electron for the tag.

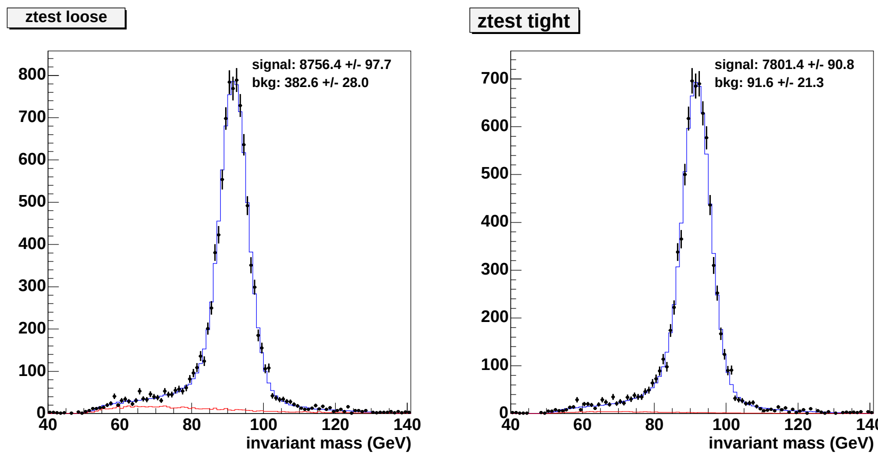

Figure 115: Background subtraction by fitting the Z probe data peak to a signal plus background shape. Shown are the invariant mass distributions of the loose probe sample (left) and tight probe sample (right).

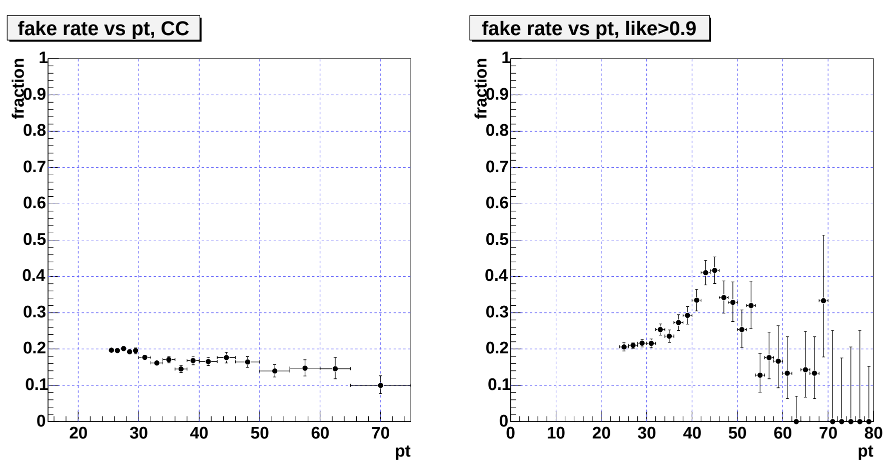

Figure 116: Comparison of CC fake rate as a function of E_T(MET < 10 GeV) with the nominal opposite jet requirement(left) and the single EM fake rate sample(right).

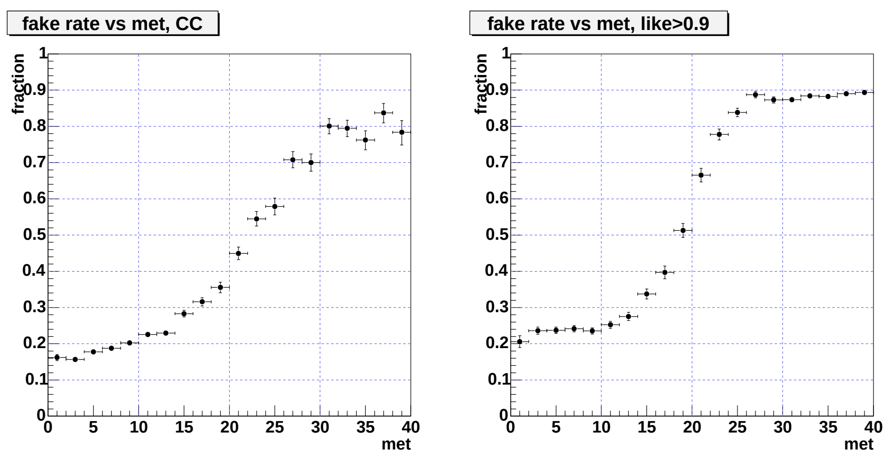

Figure 117: Comparison of CC fake rate as a function of MET with the nominal opposite jet requirement(left) and the single EM fake rate sample(right).

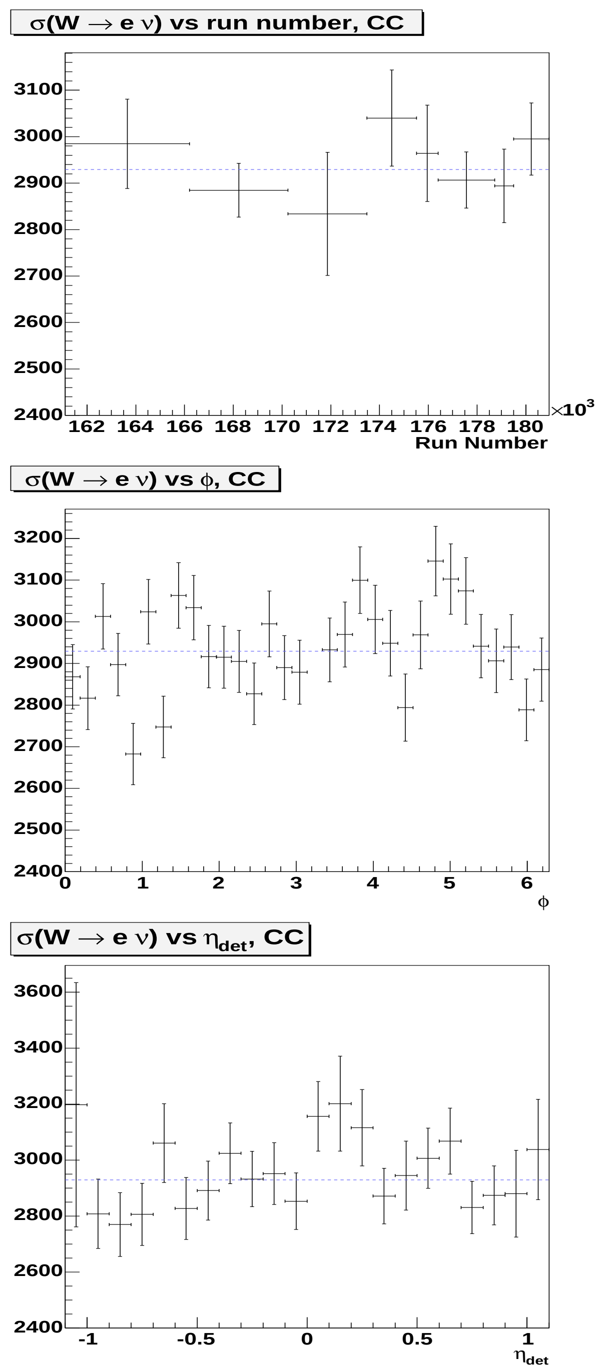

Figure 118: A comparison of W cross sections as a function of run number(top), ϕ_{det}(middle) and η_{det}(bottom). Error bars include only stat amd sys_stat errors. The horizontal dashed line represents the mean cross section.

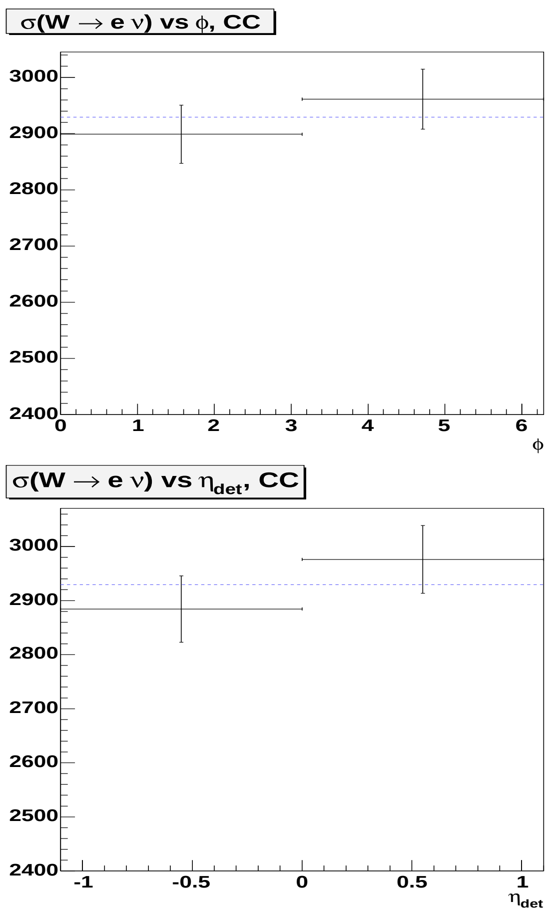

Figure 119: A comparison of W cross sections split into two halves for ϕ_{det}(top) and η_{det}(bottom). Error bars include all sources of error except PDF and luminosity. The horizontal dashed line represents the mean cross section.

References

[1] J. Stark, "Correction of the tower two problem in the calorimeter data", D0 Note 4268.

[2] J. Stark, "Correction of the energy sharing problem in the calorimeter data", D0 Note 4267.

[3] J. Kozminski et al, "Electron Likelihood in p14", D0 Note 4449.

[4] J. Gardner, "Single EM Trigger Efficiency Using a Diem Tag and Probe Method", D0 Note 4338.

[5] D. Alton et al, "Measurement of $Z \rightarrow e^+e^-$ and $W \rightarrow e^{\pm}\nu$ Production Cross Sections at the Tevatron With the DZero Detector", D0note 4131.

[6] C. Balazs, C.-P.Yuan, "Resbos: The Monte Carlo for Resummed Boson Production and Decay".
http://www.pa.msu.edu/people/balazs/ResBos/

[7] J. Zhu, "Status of PMCS_EM", D0note 4062.

[8] J. Zhu, "The WZRUNI algorithm of the PMCS_MET package: a description and comparison to p13.03 data", D0note 4090.

[9] J. Pumplin et al, "New Generation of Parton Distributions with Uncertainties from Global QCD Analysis", hep-ph/0201195.

[10] A.D. Martin et al, "Uncertainties of Predictions From Parton Distribution I: Experimental Errors", hep-ph/0211080.

[11] Golonka, Piotr, Was, Zbigniew, "PHOTOS Monte Carlo: a precision tool for QED corrections in Z and W decays", hep-ph/0506026.

[12] J. Zhu "Determination of Electron Energy Scale and Energy Resolution using P14 zee data", D0 Note 4323.

[13] Private Communication with Robert Zitoun and Pierre Petroff.

[14] http://www-d0.fnal.gov/phys_id/jes/d0_private/certified/v4.2/note.ps

[15] T. Edwards et al., "The Updated DØ Luminosity Determination - Short summary", D0 Note 4328.

[16] R. Hamberg. W.L. van Neerven and T. Matsuura, "A complete calculation of the order α_S^2 correcton to the Drell-Yan K-factor", Nucl. Phys. B359, 343 (1991).

[17] S. Eno et al., "Combining the CDF and DØ R Measurement", D0 Note 3693.

[18] Particle Data Group; S. Eidelman et al., "Electroweak model and constraints on new physics", Phys. Lett. B 592, 1 (2004).

[19] Particle Data Group; S. Eidelman et al., "Gauge and Higgs Boson Particle Listings", Phys. Lett. B 592, 1 (2004).